Spring 5-23-2019

Magnetization Dynamics in Coupled Thin Film Systems

Daniel J. Adams
University of New Orleans, djadams1@uno.edu

Recommended Citation

Adams, Daniel J., "Magnetization Dynamics in Coupled Thin Film Systems" (2019). *University of New Orleans Theses and Dissertations*. 2578.
https://scholarworks.uno.edu/td/2578

Magnetization Dynamics in Coupled Thin Film Systems

A Dissertation

Submitted to the Graduate Faculty of the
University of New Orleans
in partial fulfillment of the
requirements for the degree of

Doctor of Philosophy
in
Engineering and Applied Science
Physics

by

Daniel J. Adams

B.S. University of New Orleans, 2014
M.S. University of New Orleans, 2016

May, 2019

Acknowledgements

I give my highest gratitude to Professor Leonard Spinu. Being a part of your research group has been a rewarding experience for which I am endlessly grateful.

Thank you to my wife Bridget, my mom, dad, Jennifer, Addi, Jimmy, mawmaw, pawpaw, and my entire family and all my friends for their support and company throughout my studies.

Thank you to everyone in the physics department, my professors, Ms. Denise, my friends and classmates. Matt, thanks for hanging out with me all the times I was stuck in the lab late dealing with cryogens and for being a reasonable friend always. Thank you to everyone in AMRI, Dr. John Wiley, Poncho, Jennifer, and my colleagues. Violet, thanks for sticking around with me on evenings and weekends in the lab, too. I especially thank the past members of my research group: Denny, Shankar, Ali, Nicolas, Pratik, Jessica, Asif, Dr. José Vargas, Dr. Artur Maksymov, and everyone else. Thank you to Simeon and Danielle for your significant contributions to this work. You have all made this experience great.

I would like to thank my professors and committee members: Dr. Leonard Spinu, Dr. Leszek Malkinski, Dr. Ashok Puri, Dr. John Wiley, and Dr. Damon Smith, for all of their helpful guidance, education, and advice. I am incredibly thankful to Dr. Juliette Ioup for all of the guidance she has given to me throughout the years and to Dr. John Wiley for the support through AMRI and helping to provide relief to any problems which arose. I also thank Dr. Kevin Stokes for his help throughout my undergraduate and first years of graduate work.

I am very grateful to the Graduate School for providing the scholarship which supported my research assistantship for my years in graduate school.

To Mr. Harry Rees, thank you for all your help with the machines and electronics. I could not have done this without you. To Raymond Williams, thank you for your assistance, advice, and friendship. Thank you to Bud for always providing help and company to me. I thank NanOsc Instruments AB, especially Fredrik Magnusson, and the Quantum Design apps team for providing the CryoFMR spectrometer, Dr. Ganping Ju and Dr. Erol Girt for providing the SAF samples, Dr. Carlos Garcia for providing the exchange-biased multilayers, Dr. Paula Kern for providing the exchange-biased bilayers, and Dr. Dorin Cimpoesu for providing the simulations which supported our results as well as the advice and guidance throughout my projects.

I am very appreciative to Poncho De Leon for the constant help he provided me in my years at AMRI, and I am grateful to have known him for the last 5 years of his life. Poncho was an integral part of this institute. He had advice for every situation and was always happy to provide relaxing conversation to break up monotonous work days. AMRI is not the same without him. Thank you, Poncho.

I especially thank my mother for everything she has given me and done for me. Again, I could not have come this far without you.

Bridget, you have been my constant support and patient companion for most of my graduate studies. Thank you so much for everything. Finding you was my greatest achievement at this university. Everything else, including this Ph.D., is secondary.

Table of Contents

List of Figures

Abstract

A study is presented detailing experimental investigations of magnetization dynamics in nanostructured systems which are coupled magnetically. This work seeks to characterize the anisotropy of such systems through experimental techniques which probe microwave resonant absorption in the materials.

A custom-built experimental setup, designed and assembled in our labs, is explained in detail. This setup allows for angular-dependent ferromagnetic resonance (FMR) measurements in the sample plane through vector network analyzer spectroscopy and is adaptable to two different types of coplanar waveguides. This technique has proven effective for characterization of multiple types of magnetic systems, including multilayered structures as detailed here, with different types of anisotropies while allowing us to draw analogies with more common characterization techniques. The angular FMR setup has been used to study coupled systems, such as those coupled through the Ruderman–Kittel–Kasuya–Yosida interaction as well as exchange-biased structures. These types of coupled systems have technological impacts and are highly applied in the components of magnetoresistive random access memory. Using this new characterization technique, properties of synthetic antiferromagnets have been revealed which had not been observed before.

In addition to these experiments, magnetic susceptibility and FMR in exchange biased systems have been investigated at temperatures as low as 2 K. This investigation used a new FMR spectrometer and was one of the first studies to use this instrument.

For the first time a new method of identifying several types of coupling which can be present in layered nanostructures is presented and supported through comparison with known techniques, thus connecting a new characterization technique for layered structures with decades-old procedures. Many results within this work are also supported theoretically with computer simulations.

Keywords: magnetization dynamics, critical curve, ferromagnetic resonance, coupled magnetic structures, synthetic antiferromagnet, exchange bias.

Introduction

The term *magnetization dynamics* refers to the motion of individual magnetic moments subject to a magnetic field, a gyroscopic precession about the effective magnetic field as defined by the Landau-Lifshitz-Gilbert (LLG) equation. The timescale of magnetization dynamics, defined by this precession, is on the order of nanoseconds. In this regime, dipolar interactions, external fields, and spin-lattice interactions govern the magnetic moment dynamics. Magnetization reversal occurs through the precessional motion which is gradually opposed by damping [1, 2]. Due to the timescale of precessional motion, a characterization technique with a perturbation field on the order of gigahertz such as *ferromagnetic resonance* (FMR) is referred to here as a *dynamic* technique. On the other hand, a *static* technique uses a no perturbing field or a field of excitation frequency ω low enough such that $\omega << \omega_L$, where ω_L is the precessional frequency of the magnetic moment, the *Larmor frequency*.

With the accidental discovery of FMR over 100 years ago came a powerful characterization technique. The discovery was made in 1911, when V.K Arkad'yev observed the absorption of ultra-high frequency radiation by a ferromagnetic material, although it would still be more than a decade before the qualitative explanation by Dorfman would come. From there, little progress was made until 1935, when the theoretical work of Landau and Lifshitz was published. Finally, experimental works were published in 1946, preceding vigorous studies in the field, both experimental and theoretical [3].

Naturally, in modern times, FMR has been highly applied to nanostructured materials. The extension to nanoscale domain is logical due to the reliance of technological advancements on magnetic nanostructures, especially in the field of data storage. This class of materials is defined as having at least one dimension with length on the order of nanometers, as in nanowires and thin films. A particularly interesting subclass of these materials is coupled magnetic nanostructures. Reduced dimensions and interfaces between the materials alter the properties of magnetic structures, such as domain formation and anisotropy.

Characterization of these materials is crucial to their application. Probing the susceptibility gives important information such as coercivity and anisotropy, but it is also important to characterize these devices in a high-frequency environment which can probe dynamic properties such as damping of the magnetic moments' precession. FMR is a technique which can achieve this as well as provide useful information about the anisotropy. Thus, the static and dynamic types of techniques are certainly independently useful and can independently evaluate many different types of anisotropy. However, until now little has been done to connect the dynamic phenomenon of FMR to the static magnetization reversal in ferromagnetic materials in a way which explicitly shows the evolution from the static domain to the dynamic.

One concept which is fundamental to mapping the magnetization properties is the critical curve. This was introduced by Slonczewski [4] and further developed by Thaiville [5], based on the work of Stoner and Wohlfarth for uniaxial anisotropic particles [6]. The critical curve is the key to understanding the static behaviors of magnetic materials [7]. Radu constructed the susceptibility curves for coupled nanostructures using a quasi-static perturbation method, providing a wealth of information about the magnetization reversal and coupling effects in synthetic antiferromagnets [8, 9]. This work seeks to further the results mentioned here, by characterizing coupled magnetic systems in a high frequency dynamic environment. We use the concept of the critical curve to make the connection between the static and dynamic experiments.

A concept for studying the FMR properties of these systems is developed in an analogy to the static critical curve, which we call the *dynamic critical curve* (dCC). As will be shown, the dCC is sensitive to the different types of anisotropies and coupling effects captured by the critical curve while also containing information about the damping. A main focus of this work is to use this concept to investigate the magnetization dynamics in coupled thin film structures. Specifically, two essential components of magnetic random access memory are studied, the synthetic antiferromagnet and the exchange biased structure. In this dissertation, the dCC for these two systems will be constructed based on critical curve formalism.

Beyond this, exchange bias is studied through low temperature FMR characterization and magnetization reversal measurements, and parallels are made between this and other types of samples.

An outline of the format of the dissertation follows:

Chapter 1, *Introduction to Magnetism*, opens the dissertation with an introduction to the relevant types of magnetism, namely ferromagnetism and antiferromagnetism, as well as the energy concepts used throughout. It also introduces the Stoner-Wohlfarth model and LLG equation. The concept of FMR is explained in detail.

Chapter 2, *Experimental Techniques for Studying Magnetic Nanostructures*, details the process of magnetization measurements including magnetic susceptibility and FMR spectroscopy.

Chapter 3, *Dynamic Critical Curves in Synthetic Antiferromagnets*, begins by introducing the synthetic antiferromagnet (SAF) structure and anisotropy present. Applications of SAF are discussed as is the concept of the dCC. A new experimental setup is detailed. Finally, the dCC is presented and a connection is made to the critical curve.

Chapter 4, *Dynamic Critical Curves in Exchange Bias Structures*, elaborates on the phenomenon of exchange bias introduced in Chapter 1 and gives details on the samples measured. The dCCs for exchange bias samples are also presented here.

Chapter 5, *Low Temperature Measurements of Exchange Bias in Multilayer Thin Films*, introduces the *slow relaxer model* originally developed for rare-earth-doped garnets and was recently applied to exchange bias. This chapter presents experimental investigations of static and dynamic magnetization behavior at low temperatures of more complex exchange bias samples. Multilayered samples have interesting properties due to the higher number of interfaces. As exchange bias is a topic which is still lacking a complete theoretical explanation, experiments which reveal characteristics not observable at room temperature or which are perturbation-field-dependent may help further the study of these materials.

Chapter 6, *Conclusions*, presents conclusions drawn from work done in these projects.

The dissertation ends with a list of the author's publications and a brief Vita.

Chapter 1: Introduction to Magnetism

This chapter will introduce two types of magnetism which are central to the discussion which will follow, namely ferromagnetism and antiferromagnetism. The quantum mechanical roots of magnetism will be explained, as well as interaction processes between neighboring electron spins. Although this chapter will serve as an introduction, some preliminary knowledge of different types of magnetism is assumed, such as paramagnetism and ferromagnetism.

The first half of the chapter introduces basic concepts of magnetism while the second half focuses on the concept of magnetization switching, a key topic of this thesis. Under magnetization switching, there are two approaches: static and dynamic. The static approach is represented by Stoner-Wohlfarth model that studies the magnetization switching for an idealized system at temperature T=0 K, under which the time does not enter as a variable. The second approach to treat switching is through the Landau-Lifshitz-Gilbert equation, which is a time-dependent equation of motion of the magnetization. Finally, chapter one introduces the concept of ferromagnetic resonance (FMR), which is the main experimental tool to study magnetization dynamics here.

1.1 Ferromagnetism and Antiferromagnetism

Magnetism originates from the spin of an electron. In a ferromagnetic material, the electron spins of neighboring atoms align parallel to each other in the direction of an applied magnetic field. In the case of antiferromagnetism, energy is minimized when the neighboring electron spins are aligned antiparallel (see Figure 1.1). These materials then have a zero net magnetic moment.

A ferromagnet will have a spontaneous magnetization even without an applied field present. Materials exhibiting this property include iron, nickel, and cobalt. The magnetic moments result from the electron spins, and the material magnetization results from parallel alignment of spins. Perfect alignment should only occur at absolute zero, and as temperature increases the moments are gradually misaligned, due to the thermal energy. As temperature continues to increase, the magnetic ordering is reduced until temperature surpasses the Curie temperature T_C, destroying ferromagnetic ordering, and the material becomes paramagnetic [10].

The magnetic susceptibility χ relates the material's magnetization to the applied field to which it is subjected. χ for a ferromagnetic material can be several orders of magnitude larger than that of a paramagnetic material. Magnetic susceptibility takes the form

$$\chi = \frac{\mathbf{M}}{\mathbf{H}} = \frac{C}{(T - C\lambda)} = \frac{C}{(T - T_C)} \tag{1.1}$$

where $\boldsymbol{M}$ is the magnetization, $\boldsymbol{H}$ is the applied field, C is the Curie constant, T is temperature, and λ is the proportionality constant relating magnetization to the *exchange field* [11]. The exchange field is defined as the interaction between magnetic moments. The resulting exchange force is the cause of the magnetic moments' tendency to align parallel to one another, and it is dependent on the relative orientation of the spins of the two electrons. The exchange force is quantum mechanical and has no classical counterpart [12].

The energy of the exchange interaction between a pair of electrons, i and j, is given by

$$E_{ex} = -2J\mathbf{S}_i\mathbf{S}_j = -2J\mathbf{S}_i\mathbf{S}_j\cos\phi \tag{1.2}$$

where $\boldsymbol{S}_i$ and $\boldsymbol{S}_j$ are the spins of the electrons, and J is the exchange integral and is related to the overlap of the charge distributions of atoms i and j. Eq. (1.2) is referred to as the *Heisenberg model* [11].

Parallel or antiparallel spin orientation determines the charge distribution of the two spins. The Pauli Exclusion Principle prevents two identical particles with the same spin from occupying the same place at the same time; however, particles with opposite spins are not subject to this condition. Therefore, the energy will depend on the orientation of spins.

Note that for a parallel spin orientation, $\phi = 0$ and $\cos\phi = 1$, so J must be *positive* for energy to be minimized. This gives rise to ferromagnetic ordering. Conversely, if $\phi = \pi$, $\cos\phi = -1$, and J must be *negative* to minimize energy, giving the antiferromagnetic order. This concept can be put into perspective by reviewing the Bethe-Slater curve in Figure 1.1 [13]. A concept of critical importance is illustrated in this curve; for ferromagnetic materials, J is positive, and for antiferromagnetic materials, J is negative.

The coefficient J is difficult to evaluate, but was found by Bethe in 1933 to be a function of interatomic spacing. It takes the form

$$J = \iint \psi_a^*(\mathbf{r}_1)\psi_b^*(\mathbf{r}_2)V_C\psi_b(\mathbf{r}_1)\psi_a(\mathbf{r}_2)\mathrm{d}\tau_1\mathrm{d}\tau_2 \tag{1.3}$$

where V_C is the Coulomb potential and ψ_i terms are the wave functions. This, together with the earlier work of Slater for various materials allowed for the evaluation of the Bethe-Slater curve.

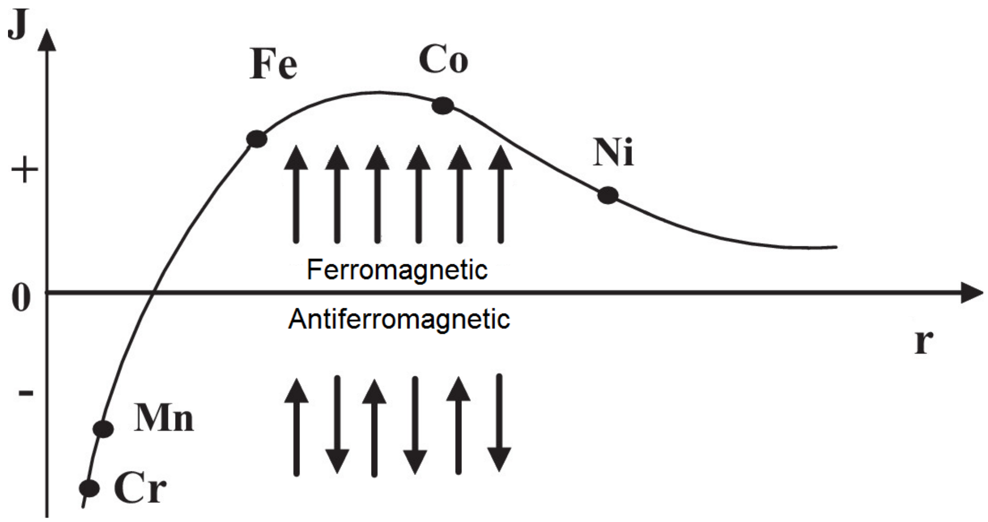

Figure 1.1 The Bethe-Slater curve (Zhong 2012).

1.2 Magnetic Free Energy

The exchange energy which keeps spins aligned in a certain orientation has been discussed above but will be reviewed again to introduce the *indirect* exchange. In addition to this, there are several other energies that must be reviewed before moving on to the Stoner-Wohlfarth model and ferromagnetic resonance. These relevant energy terms include magnetic anisotropy energies and the energy from interacting with an external magnetic field.

1.2.1 Zeeman Energy

There is a potential energy associated with a polarized magnetic moment in a magnetic field. This interaction energy between the magnetization $\boldsymbol{M}$ and the external magnetic field $\boldsymbol{H}$ is called the Zeeman energy. It can be written as

$$E_Z = -\mathbf{M} \cdot \mathbf{H} \tag{1.4}$$

1.2.2 Exchange Energy

The following subsections cover the two different types of exchange interactions: the *direct* exchange, which was discussed above, and the *indirect* exchange, a phenomenon critical to the experimental work of Chapter 3.

1.2.2.1 Direct Exchange

The direct exchange is the interaction responsible for ferromagnetic and antiferromagnetic behavior. This was described in Section 1.1.

1.2.2.2 Indirect Exchange

The indirect exchange interaction deals with the coupling of magnetic moments over relatively large distances. The theory of this interaction was introduced in 1954 when Ruderman and Kittel calculated the indirect exchange coupling of nuclear magnetic spins over long ranges

[14, 15]. Their work was expanded in the following years by Kasuya and Yosida [16, 17]. It was shown that the spin density had an oscillatory behavior as a function of separation distance and that the alignment of the coupled moments can be either parallel or antiparallel. This phenomenon was named for the four researchers and is now widely known as the RKKY interaction.

Coupling of this type between two ferromagnetic thin films separated by a conductive spacer will be seen in Chapter 3 of this dissertation. The mediator in this interaction is polarized conduction electrons. The ferromagnets on either side of the non-magnetic spacer cause oscillations in the spin density of the spacer. This then leads to an interlayer exchange coupling constant j that oscillates with the distance between the ferromagnets. Therefore, two ferromagnetic materials coupled through RKKY interaction may have parallel alignments of their magnetization or antiparallel.

The exchange constant has the form

$$j_{ij}^{RKKY} = 9\pi \left(\frac{j^2}{\varepsilon_F} \right) F(2k_F r_{ij}) \tag{1.5}$$

where ε_F is the Fermi energy, k_F is the radius of the Fermi surface, r_{ij} is the distance between the point magnetic moments, and $F(x)$ is a function given by

$$F(x) = \frac{\sin x - x \cos x}{x^4} \tag{1.6}$$

which shows the oscillatory behavior of the coupling constant [7, 18]. j^{RKKY} is shown graphically in Figure 1.2 [14].

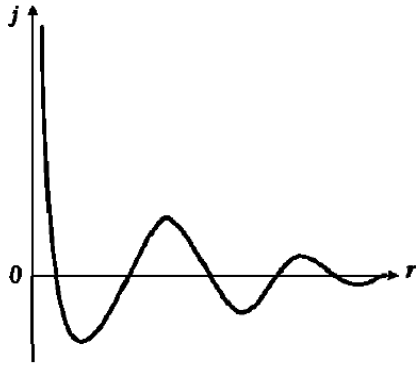

Figure 1.2 Variation of the indirect exchange coupling coefficient *j* (Ruderman 1954)

1.2.3 Anisotropy Energy

Anisotropy refers to the directional dependence of properties of a material. Anisotropies may be intrinsic to the material or particular specimen, or they may be due to some other factor, such as sample growth and preparation conditions or coupling to another material.

Many times, the anisotropy is evident from magnetization measurements such as the major hysteresis loop (MHL) [19], which describes magnetization as a function of applied magnetic field. In practice, the MHL is usually recorded from a high ("saturating") magnetic field H_{max} and swept to $-H_{max}$. In the particular case of the MHL, a sample which is not isotropic will have two axes with distinctive hysteresis loops. A loop along one particular axis will have an approximately square loop. This direction is often referred to as the easy direction or easy axis. The sample's magnetization reversal field is typically very apparent from the MHL along this direction. Along another direction, known as the hard axis, the loop will have a slanted shape and show reversible behavior (in practice, this behavior may not be perfectly reversible). In general, these axes are separated by an angle of $\frac{\pi}{2}$.

An example of the MHL is shown in Figure 1.3 [6] along different directions, with the easy axis defined as 0°. These are theoretical curves according to the Stoner-Wohlfarth (SW) model which illustrate the point that the easy axis has the squarest loop while the hard has the reversible loop.

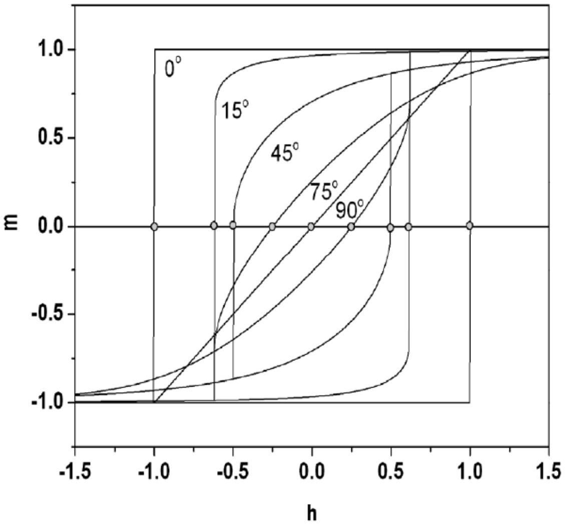

Figure 1.3 Theoretical SW MHL along different directions with respect to the easy axis (0°) (Bertotti 1998)

The following subsection describes some of the most common types of anisotropy as well as those most relevant to this dissertation.

1.2.3.1 Magnetocrystalline Anisotropy

One particularly type of anisotropy which is intrinsic to some materials is the magnetocrystalline anisotropy. When a magnetic field is applied, the electron orbital resists reorientation due to its coupling to the crystal lattice. This coupling gives a preferred magnetization direction, resulting in an axis along which anisotropy energy is minimized.

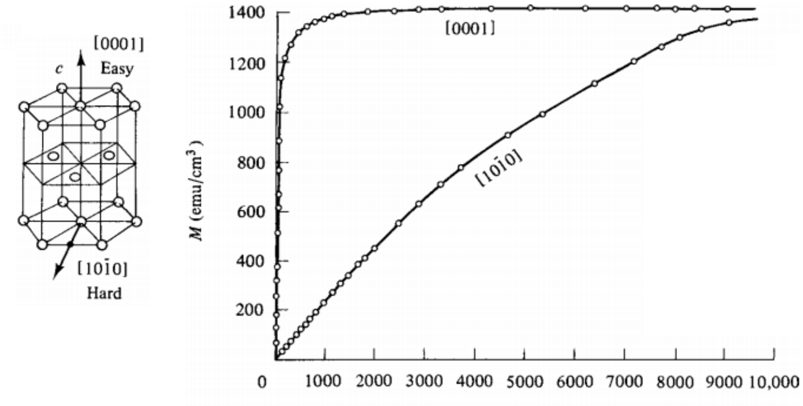

Figure 1.4 Single crystal of cobalt with indicated magnetization axes (left) and magnetization curves for a single crystal of cobalt (right) (Cullity 2008)

A common example of a material in which magnetocrystalline anisotropy is prominent is cobalt, which has uniaxial anisotropy. Referring to Figure 1.4 (left) [12], energy is dependent on the angle θ between the *c*-axis and magnetization vector. Energy is minimized when $\theta = 0^\circ$ and maximized at $\theta = 90^\circ$, but it is again minimized at $\theta = 180^\circ$. The energy is written as

$$E_K = K_0 + K_1 \sin^2\theta + K_2 \sin^4\theta + \cdots \tag{1.7}$$

where K_n are the anisotropy constants (and K_0 is often disregarded). In the case of iron and nickel, this energy is sometimes considered negligible, whereas for cobalt it is usually taken into account, often disregarding higher-order terms. For crystalline anisotropy, the constants are of the order 10^4 – 10^5 [20]. One should note that notation used in Eq. 1.7 is generally used to describe *any* uniaxial anisotropy.

1.2.3.2 Shape Anisotropy

Anisotropy can also be due to extrinsic factors, such as sample shape. When a field is applied across a magnetic material, magnetic “free poles” occur at the edges of the sample. This produces a field, called the demagnetizing field $\boldsymbol{H}_d$, which oppose the magnetization $\boldsymbol{M}$.

$$\mathbf{H}_d = -N\mathbf{M} \tag{1.8}$$

The demagnetizing factor *N* is dependent only on the magnetization and the shape of the specimen, as pole separation is dependent on sample geometry. The MHL of a sample with shape anisotropy is shown below in Figure 1.5.

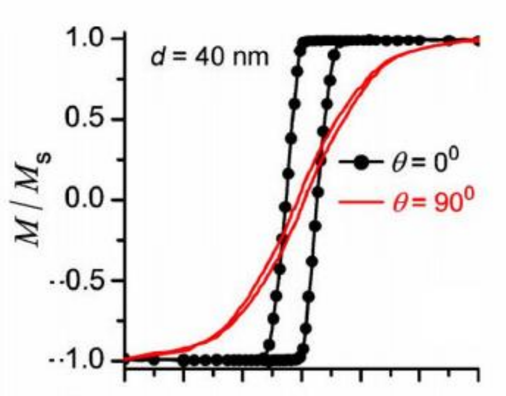

Figure 1.5 MHL for an array of nickel nanowires, with the easy axis defined as 0° and hard axis as 90°

1.2.3.3 Induced Anisotropy

The technique of annealing a sample in the presence of a magnetic field is often used to induce a uniaxial magnetic anisotropy in the material [21]. This process involves heating a sample above its Curie temperature and allowing it to cool with a field applied [22]. The anisotropy constants in these cases are typically orders of magnitude smaller than the first-order magnetocrystalline anisotropy constants. However, the effective magnetocrystalline anisotropy is dramatically reduced when the materials are grown amorphously [20]. Therefore, this technique may give the preferred direction in amorphously-grown samples. Note that growing a sample in the presence of a field can also induce anisotropy.

1.2.3.4 Exchange Anisotropy

The exchange anisotropy, also known as *exchange bias*, has been known since it was famously reported in 1956 by Meiklejohn and Bean in their renowned paper *A New Magnetic Anisotropy*. This anisotropy is observed when an antiferromagnetic material and ferromagnetic material are in intimate contact, and the sample is field-cooled such that $T_{Néel} >> T_{Measurement}$. This anisotropy manifests itself in the form of a displaced MHL [23]. The displacement maybe right or left, depending on the orientation of the sample's cooling field with respect to the measurement field. Turning the sample by 180° will therefore cause the MHL to shift to the opposite direction, in general. For this reason, the exchange bias is called *unidirectional* anisotropy. It can also be observed in measured torque curves. Angular dependent torque measurements for a sample with uniaxial anisotropy show a period of π whereas a sample with unidirectional anisotropy has a period of 2π. These properties are shown in Figure 1.6 .

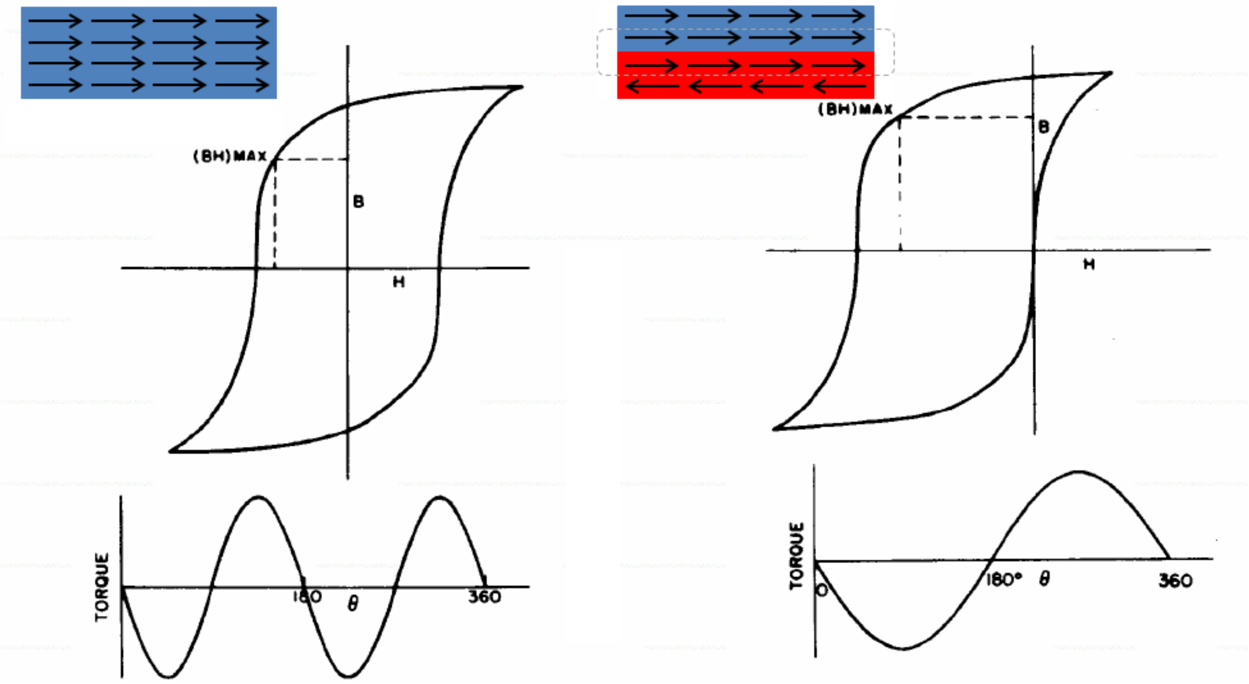

Figure 1.6 *left:* schematic of ferromagnetic moments (top), MHL for Co particles (middle), and torque vs. θ for Co particles (bottom); *right:* schematic of ferromagnetic moments coupled to antiferromagnetic moments (top), MHL (middle) and torque vs. θ for oxide coated Co particles (bottom) below the Néel temperature of the antiferromagnet

Figure 1.6 is mostly taken from Ref [23], in which a collection of cobalt nanoparticles was measured at liquid nitrogen temperatures after being cooled to these temperatures in a strong magnetic field (2 Tesla). As expected, the MHL for this sample was symmetric (Figure 1.6 *left*, middle), and the torque curve was a $\sin 2\theta$ function (Figure 1.6 *left*, bottom). A layer of oxide was allowed to grow on another set of cobalt particles. The composition of the oxide was confirmed to be CoO (antiferromagnetic below 289 K) by electron diffraction. When this sample was field-cooled and measured, the MHL was shifted, and torque curve is of the form $\sin\theta$.

Some observations were made by the authors about this phenomenon. In order for loop displacement to occur, the cobalt particles must have a layer of oxide. Additionally, there was certainly some dependence on the thickness of CoO. This property was difficult to quantify due to size distributions of the particles, but even in recent decades this property was still being actively studied. Another condition is that the material be cooled through the Néel temperature T_N, the temperature of magnetic ordering in an antiferromagnetic material, with a magnetic field applied.

Exchange bias is now often studied in thin films. It is also known that the exchange anisotropy will set if the antiferromagnetic material is grown under the influence of an *in situ* magnetic field, and it is has been commonly accepted that the uniaxial anisotropy and unidirectional anisotropy will be collinear with the cooling field, although it has been shown that this is not always true [24]. This is a subject explored further in a later chapter of this dissertation.

The physical mechanism of the exchange anisotropy is exchange coupling at the interface between the ferromagnetic and antiferromagnetic materials. Uncompensated spins in the antiferromagnet at the interface align with the magnetized ferromagnetic spins [24]. Besides the fundamental interest in these structures, exchange bias has found applications in magnetic random access memory, magnetic field sensors, and giant magnetoresistance spin valves [25-27].

1.3 Domains and Magnetization Dynamics

It is known that a ferromagnetic material in its demagnetized state has small atomic magnetic moments which are aligned randomly, such that there exists a zero vector sum over the material. Through the application of a magnetic field, these moments become aligned and the material is in a magnetized state. Atomic moments as circulating electric currents were suggested by Ampére [28] 70 years before the discovery of the electron [29].

The gradual aligning of moments randomly oriented on the interatomic scale explains the properties of paramagnets, which have random orientation of moments in the absence of field due to Boltzmann energy. However, ferromagnetic properties can be explained with regions of ordered magnetic moments but random orientation of these regions. These regions are referred to as *domains*.

1.3.1 Magnetic Domains

Domains are volumes of uniform magnetization within a material which exhibits magnetic ordering. Direct experimental evidence for magnetic domains was shown in 1949 [30], and since then domain theory has been central to discussions of magnetization processes [19]. The area separating two regions of uniform magnetization is the domain wall, across which a gradual change in the magnetization occurs. An example of a domain wall, also called a Bloch wall [31], is shown in Figure 1.7 [11].

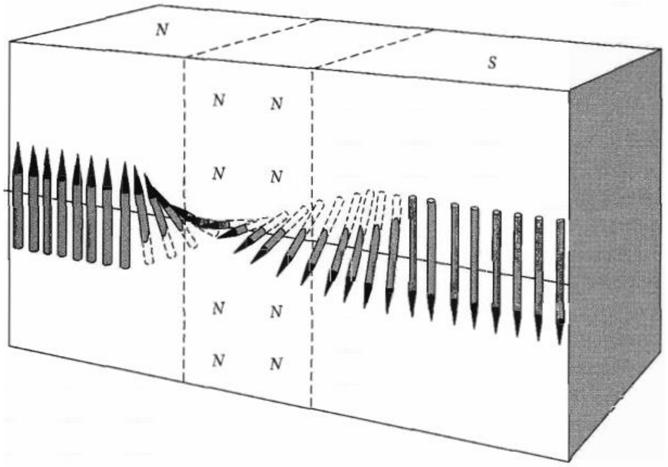

Figure 1.7 Illustration of domain wall (Kittel 2005)

The reason the wall has some thickness associated with it, rather than being a rapid directional change, is that in a ferromagnetic material, for example, the exchange energy is minimized only by adjacent spins being parallel. Therefore, a sudden change of 180° from one magnetic moment to the next would give the wall a large exchange energy. By allowing for a gradual change over N atoms, with an average angle of $\frac{\pi}{N}$ between adjacent spins, the exchange energy can be minimized.

On the other hand, the anisotropy energy is trying to minimize the wall width in order to reduce the number of spins pointing away from the easy axis. This competition leads to a domain wall having a nonzero width and a definite structure [19]. Each domain wall has an energy per unit area, since spins within the wall are not aligned with each other nor with the adjacent domains. Thus the formation of walls adds energy to the system and therefore indefinite divisions cannot occur.

As a ferromagnetic material is subject to an applied field, the number of domains aligned with the field increases in order to minimize the field energy (see Eq. 1.4), followed by the mechanism of domain rotation. In this process, magnetic moments in domains which are unfavorably aligned overcome the anisotropy energy and suddenly rotate to the direction of the easy axis nearest the field direction. Finally, at high magnetic fields, coherent rotation occurs, in which moments along the preferred easy direction gradually rotate into the field direction.

Domain walls have been observed to move in a sudden, jerky fashion in response to an applied field, no matter how smoothly that field is increased. This effect is known as the Barkhausen effect, and when the sample is placed in a search coil hooked to an oscilloscope, spikes will be observed on the voltage-time curve, which are known as Barkhausen noise. The Barkhausen noise is most prominent during the steepest part of a hysteresis loop.

A special case occurs when the sample is thin enough such that its thickness is comparable with the thickness of a domain wall. The wall structure is then different and the magnetization rotates in the plane of the sample rather than the plane of the wall. This is referred to as a Néel wall.

1.3.2 The Stoner-Wohlfarth Model

The magnetization process of a magnetic system can in principle be described by determining the total free energy of the system and imposing the conditions of equilibrium (Eq. 1.9) and stability (Eq. 1.10).

$$\frac{\partial E}{\partial \theta} = 0 \tag{1.9}$$

$$\frac{\partial^2 E}{\partial \theta^2} > 0 \tag{1.10}$$

The Stoner-Wohlfarth (SW) Model considers a single-domain particle with uniaxial anisotropy, and uses a single magnetization vector to describe the state of the whole system [6]. The consequence of this is that the magnitude of the magnetization of the SW particle will remain constant and only its direction will change. By finding the energy minima, the switching behavior of such a system can be predicted. It is important to remember that while this is an idealized model which cannot always perfectly describe a real-life system, it is nonetheless useful to consider when studying an actual system.

When subject to a magnetic field ***H***, the only energies one must consider are the anisotropy and the energy from interaction of the magnetization per volume $\boldsymbol{M}_S$ with ***H***. From the previous section, we can write the total energy of the system as [32]

$$E(\theta,\phi) = K_v V \sin^2\theta - M_S VH(\sin\theta\sin\psi\cos\phi + \cos\theta\cos\psi) \tag{1.11}$$

where K_V is the anisotropy constant per volume, V is the volume of the particle, θ is the angle between $\boldsymbol{M}_S$ and the anisotropy axis, and ψ is the angle between ***H*** and the anisotropy. We have assumed that the uniaxial anisotropy lies along the *z* axis. This is illustrated below in Figure 1.8.

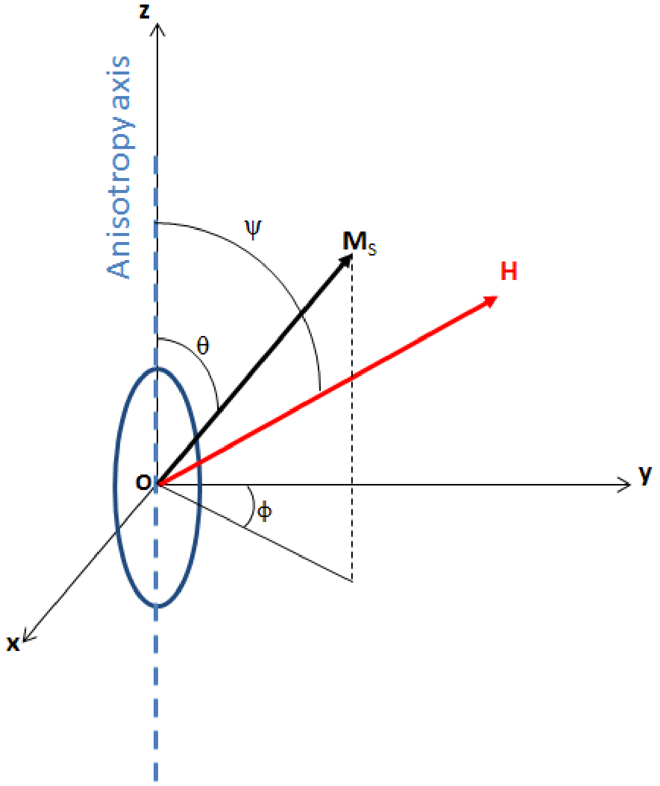

Figure 1.8 Stoner-Wohlfarth particle in magnetic field

The magnetization lies in the plane of the field and uniaxial anisotropy, which in Figure 1.8 is defined as the YZ plane. We may use the expression for the anisotropy field $H_K = \dfrac{2K}{M_S}$ in Eq. 1.11, giving it the form

$$E(\theta,\phi) = \frac{M_S V}{2}(H_K \sin^2\theta - 2H(\sin\theta\sin\psi\cos\phi + \cos\theta\cos\psi)) \tag{1.12}$$

Applying the equilibrium condition of Eq. 1.9 to this expression for energy for the angle ϕ, we find that ϕ=0°.

$$\frac{\partial E(\theta,\phi)}{\partial\phi} = M_S VH\sin\theta\sin\psi\sin\phi = 0 \tag{1.13}$$

Applying the equilibrium and stability conditions for θ,

$$\frac{\partial E(\theta,\phi)}{\partial\theta} = \frac{M_S V}{2}(H_K \sin 2\theta + 2H_z \sin\theta - 2H_y \cos\theta) = 0 \tag{1.14}$$

$$\frac{\partial^2 E(\theta,\phi)}{\partial\theta^2} = \frac{M_S V}{2}(H_K \cos 2\theta + 2H_z \cos\theta - 2H_y \sin\theta) > 0 \tag{1.15}$$

where $H_z = \cos\psi$ and $H_y = \sin\psi$ are the components of the field H which are parallel and perpendicular to the anisotropy field, respectively. These two equations are shown simplified below.

$$H_y = H_z \tan\theta + H_K \sin\theta \tag{1.16}$$

$$H_y > -\frac{H_z}{\tan\theta} - H_K \frac{\cos 2\theta}{\sin\theta} \tag{1.17}$$

Replacing the “>” in Eq. 1.17 with “=” and solving this system of equations, the parametric equations for H_y and H_z are found to be

$$H_y = H_K \sin^3\theta \tag{1.18}$$

$$H_z = -H_K \cos^3 \theta \tag{1.19}$$

It is these parametric equations which describe the SW astroid, aptly named the “critical curve”, first discussed by Slonczewski [4] and further developed by Thiaville [5]. The astroid is formed by letting θ vary from 0 to 2π. The line given by Eq. 1.16 is tangent to the astroid. Additionally, an *equality* form of Eq. 1.17 is perpendicular to this tangent. These lines are seen in Figure 1.9 in blue and red, respectively, and their point of intersection is located on the critical curve. The red line dives the plane into two. In one, there is stable equilibrium (upper region) while in the other, the equilibrium is unstable [33].

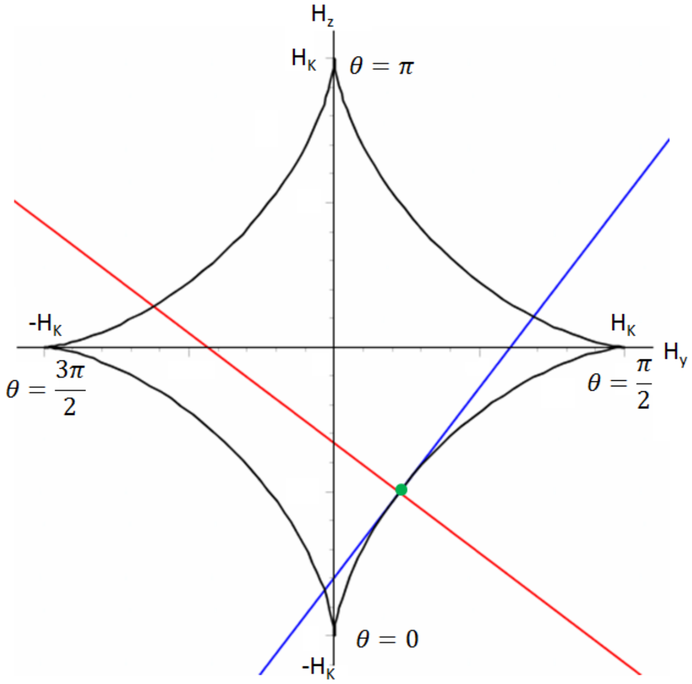

Figure 1.9 The astroid curve in plane of coordinates H_y and H_z. (black), equilibrium condition Eq. 1.16 (blue), and stability condition Eq. 1.17

The orientation of the normalized magnetization $\mathbf{m} = \dfrac{\mathbf{M}}{M_S}$ for a given magnetic field $\mathbf{h} = \dfrac{\mathbf{H}}{H_K}$ can be determined by the tangents to the astroid which passes through H in the plane defined by H_y and H_z. Each tangent may identify either a stable or an unstable state.

Note that when the field point is located outside the astroid, there is only one stable solution. For points inside the astroid, there are two (Figure 1.10). The stable states for some a field can be determined by first drawing a tangent to the critical curve starting from the coordinates (h_x,h_y). The orientation of the tangent will be stable if, when measuring from the +h_x axis, θ falls within the range labeled on the corresponding part of the astroid [4, 7].

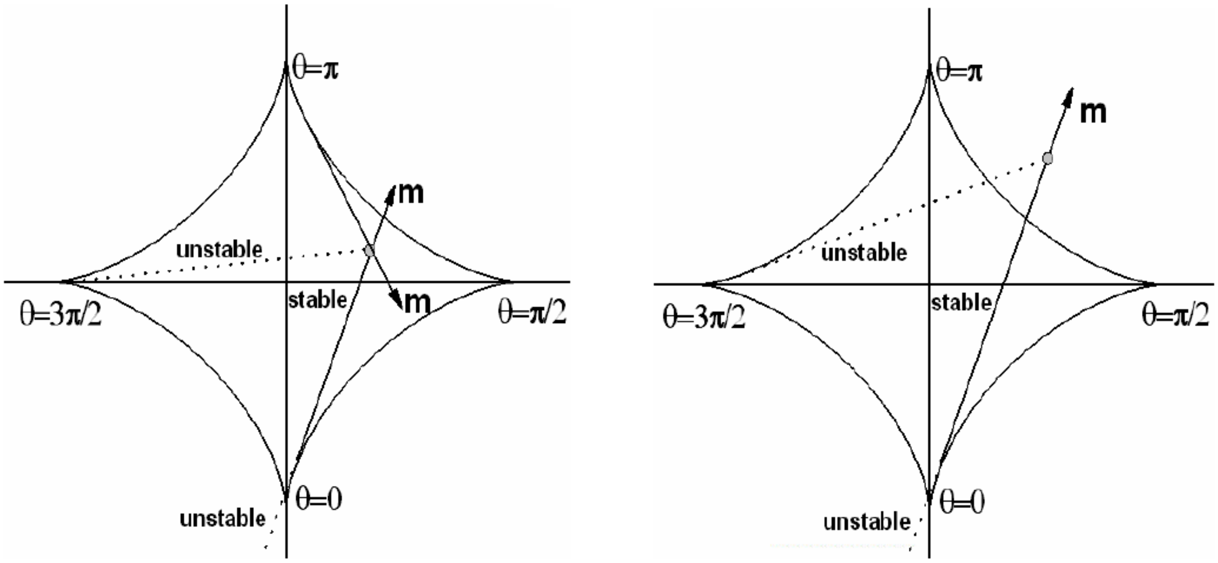

Figure 1.10 Possible **m** orientations for an applied field. The lines marked as “stable” (“unstable”) are sets of local energy minima (maxima). *left*: inside the astroid and *right*: outside the astroid (Bertotti 1998).

One then observes that when the field point is within the curve, one of two possible states occur, depending on the tangent’s starting point which is determined by the magnetization history. Outside of the astroid, there is only one possible stable state. When the critical curve is crossed as the field changes, a discontinuous change in magnetization, simply called *switching*, may or may not occur, depending on the magnetization history.

1.3.3 Néel-Brown Model

The model of Stoner and Wohlfarth assumed no thermal excitations. As a particle becomes thermally excited, the moments tend to decay toward equilibrium. Néel first considered a single-domain ferromagnetic particle with uniaxial anisotropy and uniform magnetization, but with magnetic moments affected by thermal fluctuation [34]. The concept was further developed by Brown [35], and both results gave a single relaxation time under the ideal particle assumption. The Néel-Brown model gives the relaxation time for a particle magnetization to overcome an energy barrier and spontaneously switch. The relaxation time τ is found as

$$\tau = \tau_0 e^{\frac{KV}{k_B T}} \tag{1.20}$$

where k_B is Boltmann’s constant and T is temperature, and therefore the denominator gives the thermal energy. K is the anisotropy per unit volume and V is the volume, a quantity which gives the anisotropy energy barrier seen in Figure 1.11. τ_0 is the time related to the magnetization reversal.

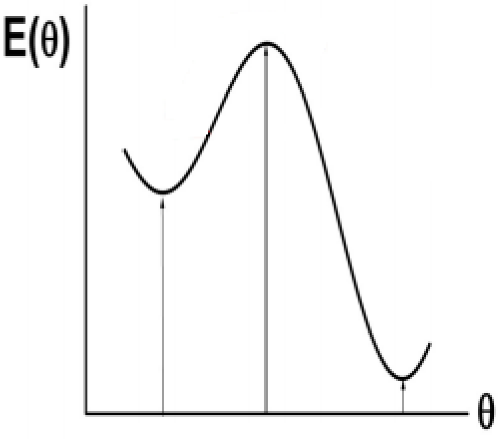

Figure 1.11 Illustration of the energy barrier

1.3.4 The Landau-Lifshitz-Gilbert Equation

In order to describe the motion of a magnetic moment ***m*** in a solid when a magnetic field is applied, one must consider the torque ***N*** experienced by ***m*** as it begins to align with the ***B*** field.

$$\mathbf{N} = \frac{d\mathbf{J}}{dt} = \mathbf{m} \times \mathbf{B} \tag{1.21}$$

where $\boldsymbol{J}$ is the angular momentum, which is proportional to $\boldsymbol{m}$ ($\mathbf{m} = \frac{q_0}{2m_0}\mathbf{J}$, and the constant of proportionality is half of the charge-to-mass ratio). Substitute this and the relationship $\mathbf{B} = \mu_0\mathbf{H}$ and consider the magnetization of a single-domain particle in its effective magnetic field as

$$\frac{d\mathbf{M}}{dt} = -\gamma(\mathbf{M} \times \mathbf{H}_{eff}) \tag{1.22}$$

where the constants have been combined and written as $-\gamma$, the gyromagnetic ratio. This is the Landau-Lifshitz (LL) equation. Based on the reasoning that damping should exist, giving the system the magnetization state with minimum energy while the magnetization remained constant, a phenomenological damping term was added to this equation [33]:

$$\frac{d\mathbf{M}}{dt} = -\gamma\left(\mathbf{M} \times \mathbf{H}_{eff}\right) - \gamma\frac{\lambda}{\mathbf{M}_S}(\mathbf{M} \times [\mathbf{M} \times \mathbf{H}_{eff}]) \tag{1.23}$$

where $\boldsymbol{M}_S$ is the saturation magnetization and λ is the phenomenological damping parameter.

Eq. 1.23 works for cases of small damping. Gilbert later introduced the equation [36]

$$\frac{d\mathbf{M}}{dt} = -\gamma\left(\mathbf{M} \times \mathbf{H}_{eff}\right) + \frac{\alpha}{M_S}(\mathbf{M} \times \frac{d\mathbf{M}}{dt}) \tag{1.24}$$

where α is often referred to as the Gilbert damping parameter. Eq. 1.24 is known as the Landau-Lifshitz-Gilbert (LLG) equation. This is capable of describing strong damping. It is phenomenologically different and more correct than the LL equation [37, 38]. The precession of the magnetization is shown in Figure 1.12.

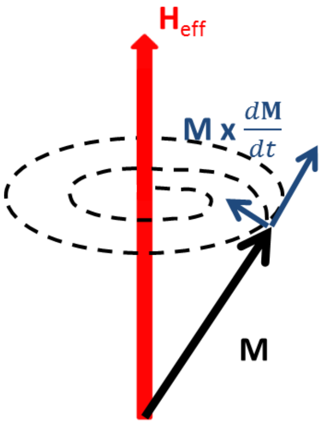

Figure 1.12 Precession of magnetization subject to effective magnetic field

1.3.5 Spin Resonance

Electron paramagnetic resonance is a resonance between an alternating field and the net magnetic moment of an electron, subjected to the applied field [19]. This phenomenon is experimentally observed when a sample is placed in a field ***H*** of a few thousand Oersted (Oe). As noted in previous sections, the spins precess around the field direction at the Larmor frequency ν_L which is dependent on ***H***. Additionally the sample must experience an alternating field at a right angle to the field ***H***. When the frequency ν of this alternating field equals ν_L, the system is in resonance.

Recall Eq. 1.4 for potential energy of a magnetic moment ***m*** in a magnetic field:

$$E = -m_H H \tag{1.25}$$

where we have used m_H to represent the component of the magnetic moment along the direction of ***H***. This value is determined by

$$m_H = g m_j \mu_B \tag{1.26}$$

where g is the gyroscopic splitting factor with a value of 1 for orbital motion and 2 for spin, μ_B is the Bohr magneton, and m_j is a quantum number representing the projection of the angular momentum j along the specified axis.

The state of the material subjected to ***H*** can be thought of as a distribution of atomic moments among a set of $2j+1$ energy levels. Each level is distinguished by a value of m_H. The separation between energy levels is then [19]

$$\Delta E = \Delta m_H H = g\mu_B H \tag{1.27}$$

since the values of m_j differ by unity, only allowing transitions between adjacent levels. It logically follows then that the condition for resonance is

$$h\nu = g\mu_B H \tag{1.28}$$

where h is Planck's constant and v is the microwave frequency, and the product is related to energy by the well-known formula $\Delta E = h\nu$.

1.3.5.1 Ferromagnetic Resonance

Resonances also occur in ferromagnetic materials, where the main difference between ferromagnetic resonance (FMR) and electron paramagnetic resonance is the presence of strong exchange forces [22] and anisotropy fields H_K. When ***H*** is applied, there is coherent precession about the magnetic moments' equilibrium orientation. The energy absorption is again given by Eq. 1.28, with $g \approx 2$ (although g may differ due to spin-orbit interaction).

The simplest case of FMR occurs when the field is strong enough to remove the domain structure, i.e. the sample is magnetically saturated. FMR can however occur in unsaturated states. Resonance modes may be non-uniform, indicating areas of different magnetizations.

FMR is, in principle, similar to other forms of resonance (with H in the Eq. 1.28 replaced by $H + H_K$). The total electron magnetic moment precesses around the direction of the applied magnetic field. When the precessional frequency equals the frequency of the transverse field, energy is absorbed from the electromagnetic source. The resonance condition was famously derived by Kittel in his renowned text *Introduction to Solid State Physics*. The derivation is shown here, with N_x, N_y, and N_z being the demagnetizing factors; $\boldsymbol{B}_i$ are the components of the internal magnetic induction, and $\boldsymbol{B}_0$ is the induction related to the applied field [11].

$$B_{i,x} = B_{0,x} - N_x M_x ;\ B_{i,y} = B_{0,y} - N_y M_y ;\ B_{i,z} = B_{0,z} - N_z M_z \tag{1.29}$$

Recalling the spin equation of motion and relating it to magnetic induction, $\frac{d\mathbf{M}}{dt} = \gamma(\mathbf{M} \times \mathbf{B}_i)$, and applying the rules of cross products, we have

$$\frac{dM_x}{dt} = \gamma(M_y B_z - M_z B_y) ;\ \frac{dM_y}{dt} = -\gamma(M_x B_z - M_z B_x) \tag{1.30}$$

To first order, we set $M_z = M$ and $\frac{dM_z}{dt} = 0$. Applying the Eqs. 1.29,

$$\begin{aligned}\frac{dM_x}{dt} &= \gamma[M_y(B_0 - N_z M_z) - M(-N_y M_y)] = \gamma[B_0 + (N_y - N_z)M] \\ \frac{dM_y}{dt} &= -\gamma[M_x(B_0 - N_z M_z) - M(-N_x M_x)] = -\gamma[B_0 + (N_x - N_z)M]M_x\end{aligned} \tag{1.31}$$

With time dependence $e^{i\omega t}$, solutions exist if

$$\begin{vmatrix} i\omega & \gamma[B_0 + (N_y - N_z)M] \\ -\gamma[B_0 + (N_x - N_z)M] & i\omega \end{vmatrix} = 0 \tag{1.32}$$

Finally, the FMR condition relating frequency ω_0 to induction B_0 is found to be [11]

$$\omega_0^2 = \gamma^2[B_0 + (N_y - N_z)M][B_0 + (N_x - N_z)M] \tag{1.33}$$

1.4 Summary

In this chapter, we have provided an overview of different types of magnetism and discussed the energy terms relevant to the following chapters as well as how these energies affect magnetization processes. In particular, we determined the astroid using the Stoner-Wohlfarth model. It is seen that switching behavior can be deduced using the free energy of the system. This is the basic concept of the *critical curve*, a polar map of points of magnetization reversal as determined by a method able to probe the irreversible changes in orientation of magnetization. It is essentially the locus of points for which magnetization reversal occurs [5], and will be discussed further in Chapter 2.

Additionally, the concept of ferromagnetic resonance has been presented. This is a topic highly relevant to later parts of this dissertation. An experimental method for determining FMR as the high-frequency analog to susceptibility measurements will be explained in the next chapter and is the central idea of the work to be presented. It is a method sensitive to different anisotropies in ways similar to those found in the critical curve.

Chapter 2: Experimental Techniques for Studying Magnetic Nanostructures

This section will introduce the experimental methods relevant to the following chapters. We will define the concepts of *static* and *dynamic* magnetization measurements and discuss experiments in these two regimes. In the static regime, susceptibility measurements give important information regarding switching fields and anisotropy. Susceptibility χ was defined in Eq. (1.1) as the ratio of the magnetization induced in the material and the applied magnetic field $\boldsymbol{H}$. The differential susceptibility, defined as

$$\chi_{ij} = \frac{\partial M_i}{\partial H_j} \tag{2.1}$$

describes ferromagnetic materials. The susceptibility tensor describes the response of the material, i.e. magnetization $\boldsymbol{M}$, in the i^{th} direction due to a change of $\boldsymbol{H}$ in the j^{th} direction.

In the dynamic regime, we will focus on the phenomenon of spin resonance. As this dissertation is concerned with magnetization dynamics in ferromagnetic materials, we will restrict our discussion to ferromagnetic resonance (FMR). These experiments are mainly performed in the saturated states of the material and can give information about relaxation phenomena. Additionally, FMR can be used to identify anisotropies in different layers of multilayer materials. There are several techniques for performing FMR spectroscopy which will be discussed.

The common feature of all frequency-domain magnetic experiments is that the property measured is susceptibility, which has a real and imaginary component, denoted as χ' and χ'', respectively.

2.1 Static and Dynamic Regimes

The distinction between the static and dynamic regimes in experimental magnetism is concerned with the presence of an excitation field $\boldsymbol{h}_{\mathrm{ac}}$, and how the frequency of this field ω compares with the precessional frequency of the magnetic moment ω_L. Experiments with no excitation field, or an excitation field of low enough frequency such that $\omega << \omega_{\mathrm{L}}$, are referred to as *static* experiments. Examples of this include susceptibility measurements such as the major hysteresis loop (MHL) which uses no excitation frequency and another experiment detailed in this chapter which involves an LC tank resonator with frequency on the order of megahertz, approximately 3 orders of magnitude smaller than ω_L. Conversely, in ferromagnetic resonance (FMR) spectroscopy, $\boldsymbol{h}_{\mathrm{ac}}$ is a microwave frequency field. As this is comparable to precessional frequency, FMR is a *dynamic* experiment.

2.2 Static Magnetization Measurements

In this section, major experimental techniques in the static regime used extensively throughout this dissertation will be discussed. We will review the process by which the experiments are carried out as well as the underlying physics which makes them possible.

2.2.1 The Major Hysteresis Loop

The major hysteresis loop (MHL), mentioned briefly in Section 1.2.3, is a magnetization curve as a function of field, a characterization technique from which much information can be identified by observation. Figure 2.1 shows the characteristics quickly obtainable from the MHL, including the remanent magnetization or *remanence*, which is the magnetization retained at zero field after the material has been magnetized, the *saturation magnetization*, which is where the magnetization of the material levels off, and the *coercive field* H_c, which is the field required to drive the material magnetization to zero after it has been magnetically saturated.

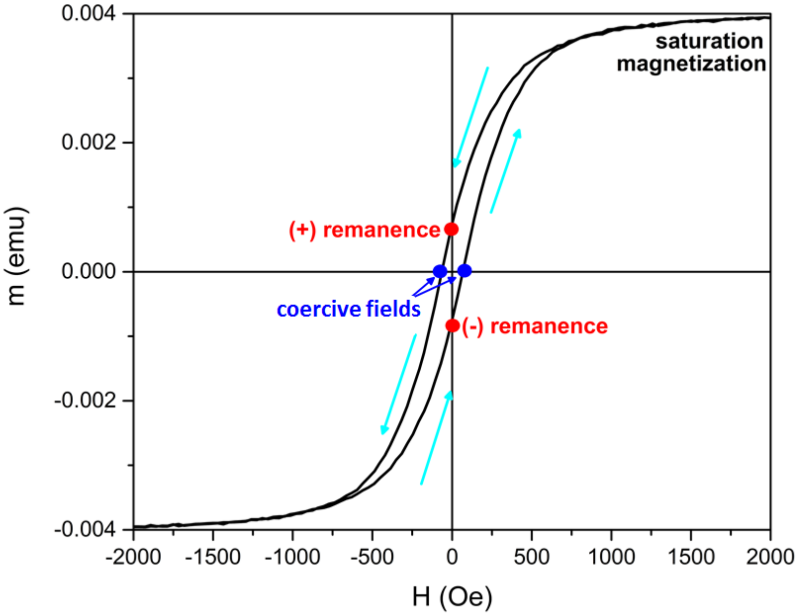

Figure 2.1 MHL of a nickel nanostructure experimentally recorded by VSM. Light blue arrows indicate the path direction of the loop.

The MHL is often the first method used in magnetic material characterization, especially because it can quickly identify the class of magnetic material studied. Figure 2.2 shows some of the different results one may obtain when recording the magnetization curve for different classes of materials.

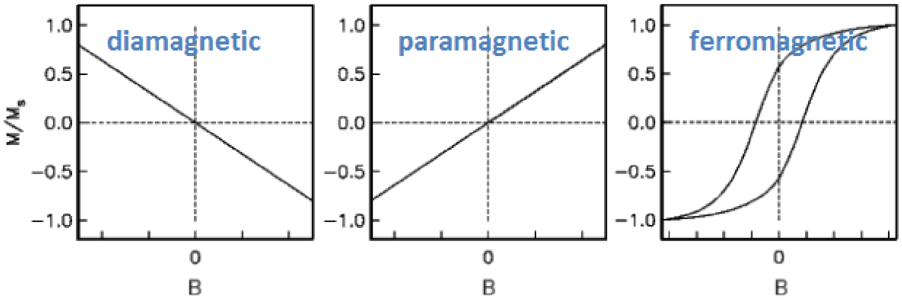

Figure 2.2 Magnetization curves of a diamagnetic, paramagnetic, and ferromagnetic material

In the following chapters, MHLs are primarily recorded using a vibrating sample magnetometer (VSM), which is a highly sensitive instrument for measuring magnetic forces. The sample under study is fixed to the bottom of a rod and suspended between the poles of an electromagnet. The coils of the electromagnet are charged to the desired field ***H*** which is measured by a built-in Hall effect gaussmeter. The sample is vibrated in the vertical direction and as it becomes magnetized, the field of the sample in rapid motion causes a proportional current to be induced in a small set of pickup coils fixed to the poles of the electromagnet. This current is translated to a signal and output by the software. In our lab, we use a Micromag 3900 VSM System from Princeton Measurements Corporation, now a part of Lake Shore Cryotronics.

Alternatively, an alternating gradient magnetometer (AGM) may be used. This technique is more sensitive to materials with a small magnetization, able to measure magnetic moments in the range of 10^{-9} emu whereas the VSM is limited to 10^{-6} emu. Again the sample is placed between the poles of an electromagnet, where ***H*** is monitored by a gaussmeter. Rather than vibrations, an alternating gradient field is applied across the sample space. As the material becomes magnetized, the gradient field produces a force on the sample, causing a very small but measureable deflection of the sample rod left or right proportional to the sample's magnetic moment. A piezoelectric element to which the sample rod is attached is able to measure the deflection which is recorded and output as a magnetic signal.

Another method for obtaining the MHL is using the magneto-optical Kerr effect (MOKE), which is the change in polarization of light reflected from the surface of a magnetized material. In a MOKE system, the sample space is between the poles of an electromagnet, as usual, and a laser is set up such that the light reflects from the sample surface and is collected at a photodiode after passing through a polarizing filter.

2.2.2 Tunnel Diode Oscillator Technique

A number of research efforts have been dedicated to developing characterization methods which can measure various properties of nanostructured materials [7]. A sensitive and flexible technique for probing the anisotropy of ferromagnetic materials is the *transverse susceptibility method*. In this experiment, two fields are applied simultaneously: an *ac* and *dc* field applied perpendicular to each other. The original model of Aharoni developed under the Stoner-Wohlfarth model tells us that the transverse susceptibility signal has peaks located at the values of the dc field which are equal to the anisotropy field and switching field values [39].

Resonator methods have been used extensively to probe switching behavior in materials [8, 9, 40-49], and these studies have shown that the *tunnel diode oscillator* (TDO) method is a consistently reliable technique for characterizing magnetization switching. This technique is based on an LC-tank circuit where the inductor L couples to the material being studied. A change in the material properties will induce a change in the inductance, resulting in a shift in the resonance frequency [50]. This shift may reflect, for example, a change in the magnetic susceptibility χ.

A brief description of the TDO circuit follows. An LC-tank is externally powered to compensate for dissipation. This power provided by a tunnel diode that is precisely forward-biased with a voltage in the region of the negative slope of the I-V curve [50]. A tunnel diode is a semiconductor diode with a heavily doped p-n junction about 10 nm wide, resulting in a broken bandgap. The conduction band electrons on the n-side are approximately aligned then with the valence band holes on the p-side. With normal forward-biasing, as voltage increases, electrons initially tunnel through the p-n junction barrier as electrons in the n-side conduction band become aligned with p-side valence band holes. As voltage continues to increase, the states become misaligned and current is reduced. This is negative resistance, because the decrease corresponds to increasing voltage. Increasing the voltage further, the diode operates as a normal diode. Electrons travel by conduction across the p-n junction rather than tunneling. Therefore, the most important operating region is the negative resistance region [7].

In the tunnel diode, dopant concentrations in the p and n layers are increased to a point to which the reverse breakdown voltage becomes zero and the diode conducts in the reverse direction. In conventional diodes, conduction takes place under forward bias but is blocked when the junction is reversed biased. This is only overcome at the point of reverse breakdown voltage, which defeats the natural tendency to not conduct in the reverse direction. When a tunnel diode is forward-biased, tunneling occurs, and a region exists where an increase in forward voltage is accompanied by an increase in forward current. This negative resistance region is exploited in the tunnel diode oscillator [7].

The resonant frequency for an LC circuit is expressed

$$\omega_0 = \frac{1}{\sqrt{LC}}, \text{ or } f_0 = \frac{1}{2\pi\sqrt{LC}} \tag{2.2}$$

If the inductance L changes by some amount ΔL, the frequency may then be written as

$$f_0 + \Delta f = \frac{1}{2\pi\sqrt{(L+\Delta L)C}} \tag{2.3}$$

Using a binomial expansion for small ΔL seen below, an expression can be found for the change in frequency.

$$f_0+\Delta f=\frac{1}{2\pi\sqrt{(L+\Delta L)C}}=\frac{1}{2\pi\sqrt{LC}}\frac{1}{\sqrt{\left(1+\frac{\Delta L}{L}\right)}}=f_0\left(1+\frac{\Delta L}{L}\right)^{-\frac{1}{2}}$$

$$(1-x)^{-\frac{1}{2}}=1+\left(-\frac{1}{2}\right)(-x)+\frac{\left(-\frac{1}{2}\right)\left(-\frac{3}{2}\right)}{2!}(-x)^2+\ldots \quad \text{Binomial Expansion}$$

$$f_0\left(1+\frac{\Delta L}{L}\right)^{-\frac{1}{2}}\approx f_0\left\{1+\left(-\frac{1}{2}\right)\left(\frac{\Delta L}{L}\right)\right\} \quad \text{to first order}$$

$$\text{Therefore,} \quad f_0+\Delta f\approx f_0-\frac{1}{2}\frac{\Delta L}{L}f_0$$

$$\Delta f\approx-\frac{1}{2}\frac{\Delta L}{L}f_0 \tag{2.4}$$

If a magnetic sample is acting as the core of the solenoid, then the flux density *B* is

$$B=\frac{\mu_0\mu_r N^2 i}{l} \tag{2.5}$$

Here, *N* is the number of turns in the coil, *i* is the current, and *l* is the length of the coil. As usual, μ_0 and μ_r are the permeability of free space and relative permeability, respectively. The total magnetic flux through the coil of cross-sectional area *A* is

$$\Phi=\frac{\mu_0\mu_r N^2 iA}{l} \tag{2.6}$$

The coil has a self-inductance defined as $L=\frac{d\Phi}{di}$, which gives

$$L=\frac{\mu_0\mu_r N^2 A}{l} \tag{2.7}$$

Now, permeability can be defined as $\mu=\mu_r\mu_0$, or, in terms of susceptibility,

$$\mu=(\chi+1)\mu_0 \tag{2.8}$$

Substituting this definition into Eq. 2.7 gives

$$L = \frac{\mu_0 \left(\chi + 1 \right) N^2 A}{l} \tag{2.9}$$

and Eq. 2.4 becomes

$$\frac{\Delta f}{f_0} = -\frac{\Delta \left\{ \dfrac{\mu_0 \left(\chi + 1 \right) N^2 A}{l} \right\}}{2 \left\{ \dfrac{\mu_0 \left(\chi + 1 \right) N^2 A}{l} \right\}} \tag{2.10}$$

Therefore, a change in resonant frequency is associated with a change in the magnetic susceptibility of the sample inside of the coil [7].

$$\frac{\Delta f}{f} \propto \frac{\Delta \chi}{\chi} \tag{2.11}$$

In practice, the sample is placed within the inductor coil of the circuit, which is then placed in between the coils of an electromagnet (see Figure 2.3 which is taken from Ref [44]). The circuit is powered, and the dc field produced by the electromagnet is ramped from negative saturation to positive and then from positive saturation to negative. The TDO is self-resonant, with a typical resonant frequency around 5 to 8 MHz. The coil’s frequency is recorded as a function of field to monitor the change in frequency, indicating a change in χ.

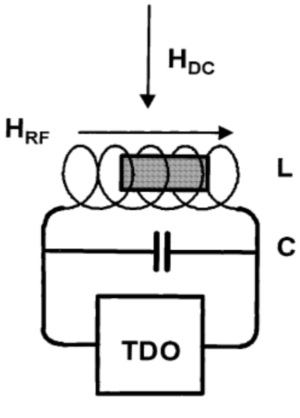

Figure 2.3 Schematic of the rf susceptibility TDO experiment

2.2.2.1 The Critical Curve from Susceptibility Measurements

As mentioned previously, transverse susceptibility (TS or χ_t) measurements in our lab require two magnetic fields: a dc field $\boldsymbol{H}_{dc}$, and a small, perturbing ac field $\boldsymbol{h}_{ac}$. χ_t has both a real (χ_t') and imaginary component (χ_t''). When the perturbing frequency is low, χ_t'' is zero, and TS is given by [51]

$$\chi_{xx} = \frac{M^2}{F_{\theta\theta}F_{\varphi\varphi} - F_{\theta\varphi}^2}\left(\sin^2\theta_M \sin^2\varphi_M F_{\theta\theta} + \frac{\sin 2\theta_M \sin 2\varphi_M}{2} F_{\theta\varphi} + \cos^2\theta_M \cos^2\varphi_M F_{\varphi\varphi}\right) \tag{2.12}$$

where θ_M is the equilibrium polar angle of the magnetization vector $\boldsymbol{M}$, φ_M is the equilibrium azimuthal angle, and F_{ij} are the second derivatives of the free energy density at the equilibrium position where F is minimum. Now, the denominator $F_{\theta\theta}F_{\varphi\varphi} - F_{\theta\varphi}^2$ is the curvature of the free energy surface at equilibrium. The points for which the denominator equals zero are the critical points which occur as the system energy passes from one energy minimum to another [47]. Therefore, the points at which the denominator is zero are the switching points, described by the free energy and satisfying the condition $F_{\theta\theta}F_{\varphi\varphi} - F_{\theta\varphi}^2 = 0$. In experiment, it is easy to see that this situation will manifest as a singularity.

The samples discussed in this work are thin films which exhibit some type of anisotropy. Therefore, it is very important for measurements to be angular-dependent. For a TS experiment, this would require applying the dc field at different orientations while simultaneously rotating the ac field in order to keep these two fields perpendicular in the plane of the thin film. Doing this would allow us to track angular variation of the switching fields. In practice, this would mean the sample would have to be physically rotated within the coil in very precise increments. As the coil diameter is approximately 7 mm, rotating the sample to any precisely measured angle would be difficult or even impossible. It is certainly much easier to leave the sample and coil stationary with respect to one another and rotate the dc magnetic field with respect to the coil/sample system. In this case, however, we would no longer be measuring *transverse* susceptibility. Fortunately, it has been proved that, although the experimental setup is different from traditional TS measurements, the singularities detected still preserve the switching information of TS experiments [47]. In this case, the susceptibility χ_{xx} from Eq 2.12 no longer represents TS, but rather a combination of transverse and longitudinal susceptibility.

Now that we have established the feasibility of measuring the angular dependence of susceptibility, we emphasize the point that this allows us to track the switching fields as a function of field orientation θ_H. The critical curve can then be obtained by plotting the switching field values in polar coordinates. This is most conveniently accomplished in our setup by recording the susceptibility signal for both increasing and decreasing fields along one position of the dc field magnet. This point is easier explained in a picture. Figure 2.4 [47] shows an example of susceptibility curves calculated for an ideal Stoner-Wohlfarth particle for fields increasing from negative saturation to positive (top left) and decreasing from positive saturation to negative (bottom left), and the critical curve as can be constructed from the singularities in the susceptibility signal.

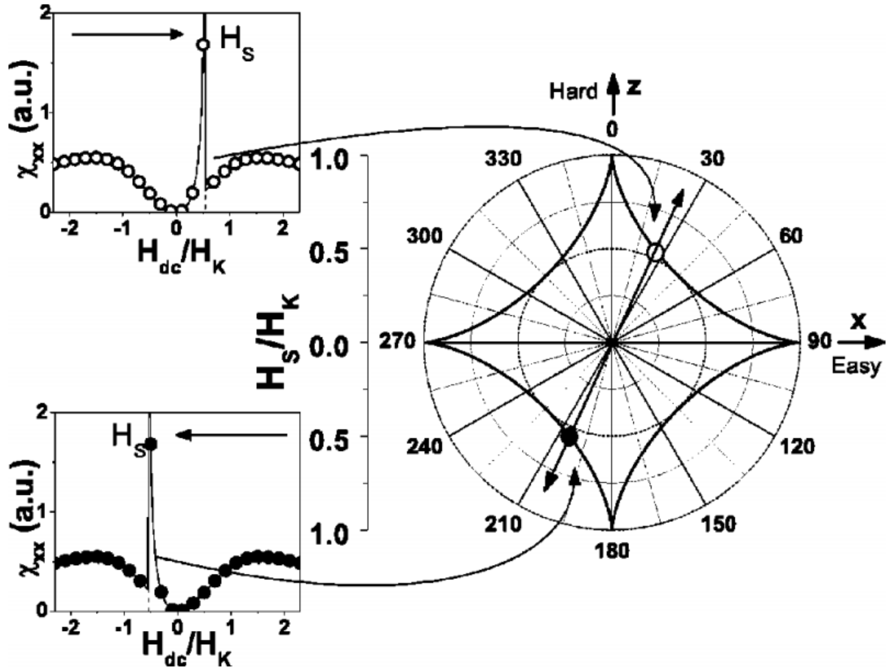

Figure 2.4 *left*: Simulated susceptibility curve for an ideal Stoner-Wohlfarth particle for θ_H = 25° (top: fields increasing; bottom: fields decreasing). *right*: Theoretical critical curve as determined from susceptibility signals at different angles (Spinu 2005).

2.3 Dynamic Magnetization Measurements

This section exclusively focuses on spin resonance in ferromagnetic materials (ferromagnetic resonance – FMR). We will cover the several different techniques for studying FMR in our systems.

It may be useful to first review the basic theory and practice of spin spectroscopy, first introduced in Section 1.3.5 Spectroscopy is the measure of energy differences, ΔE. Recall that electromagnetic energy will be absorbed if

$$\Delta E = h\nu \tag{2.13}$$

This absorption causes a transition from the lower energy state to the higher, with these energy differences being due to the Zeeman effect. The Zeeman effect results from the interaction of unpaired electrons with the external field produced in the lab, B_0. The electron will be in the lowest energy state when aligned parallel $\left(M_S = -\frac{1}{2}\right)$ to *B₀* and highest when it is antiparallel $\left(M_S = +\frac{1}{2}\right)$ to B_0 (Figure 2.5 from Ref [52]).

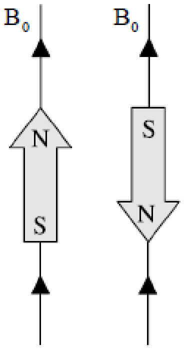

Figure 2.5 Energy orientations of the electron magnetic moment

The most basic equations relevant to spin resonance are

$$E = g\mu_B B_0 M_S = \pm\frac{1}{2} g\mu_B B_0 \tag{2.14}$$

and

$$\Delta E = h\nu = g\mu_B B_0 \tag{2.15}$$

From Eqs 2.14 and 2.15, it is clear that the energy states diverge linearly as the field increases (see Figure 2.6 from Ref [52]), but with no field, the two states have the same energy. Therefore, a field must be present to measure the energy difference. In the case of ferromagnetic resonance, absorption can be detected with no field applied due to the presence of an anisotropy field.

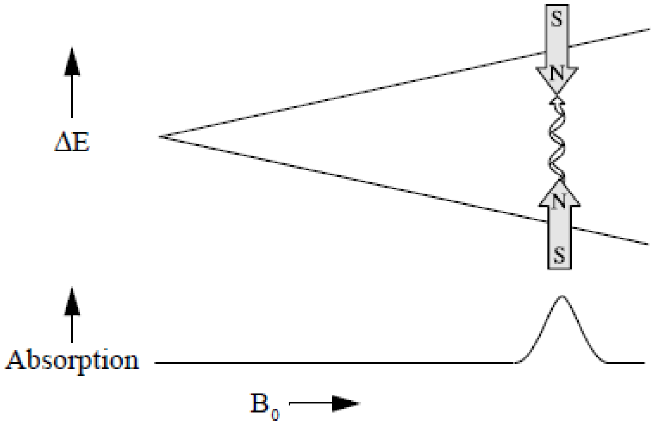

Figure 2.6 Spin state energy difference as a function of magnetic field

The following sections detail different method through which the energy states are probed. In this thesis, spin resonance are exclusively studied in ferromagnetic materials.

2.3.1 Cavity Resonator Method

Note that in spin spectroscopy, either the external field magnitude or the electromagnetic field frequency may be varied. For spin resonance, the electromagnetic wave is often in the microwave bands, because this is where resonances normally occur for fields easily achieved in the laboratory.

In cavity FMR, the magnetic field is varied while the microwave frequency is held constant. There are four major components to the spectrometer. The first is the source which provides the microwave radiation. The second is the sample, which is subject to the external field and the microwave. The third is detector. The fourth, the sample cavity, will be discussed later. When the detector receives a reduced quantity of radiation relative to the quantity provided by the source, resonance has occurred. If the output is the absorption signal, then a peak will correspond to absorption. By convention, the derivative of the absorption, which takes the form of a Lorentzian derivative, is displayed. An example of this is shown in Figure 2.7, where the ordinary Lorentzian is shown in red and the derivative is shown in black. The solid gray vertical line corresponds to the resonance. The dashed blue and purple lines correspond to the full width at half maximum linewidth and the peak-to-peak linewidth, respectively.

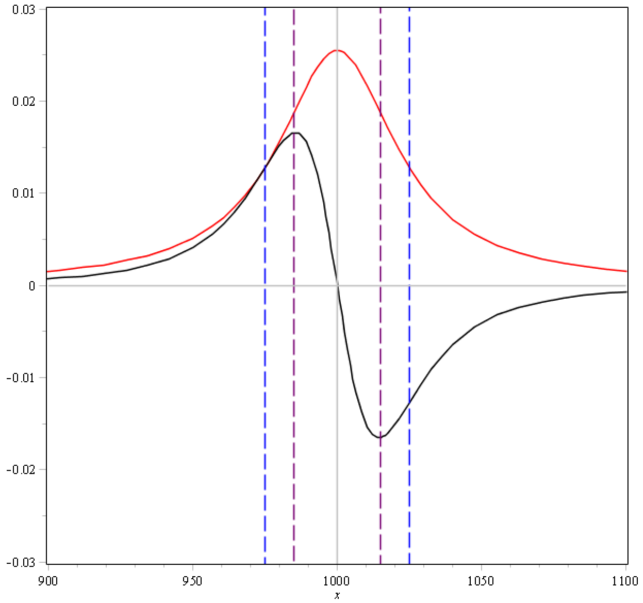

Figure 2.7 Simulated Lorentzian (red) and its derivative (black)

The microwave bridge houses the source and detector. A circulator is used to ensure the detector only sees the microwave radiation coming back from the sample cavity. Referring to Figure 2.8 from Ref [53], the radiation returned from the cavity at port 2 can only travel to port 3.

Energy losses which occur at resonance by which the oscillatory motion of the electron spins is converted to heat within the sample determine the width of the resonance peak (In Figure 2.7, the dashed purple lines associated with the peak-to-peak linewidth of the black curve).

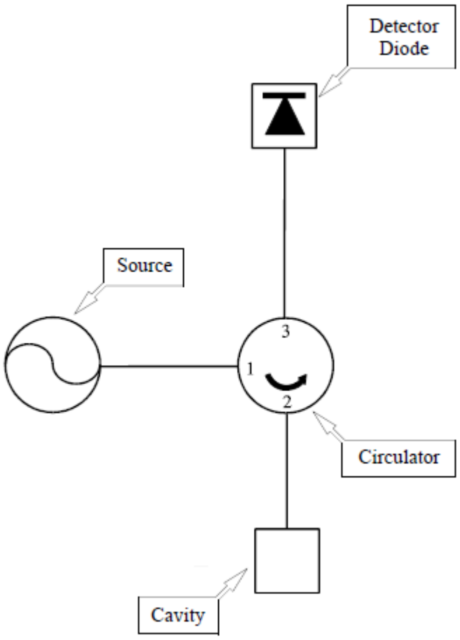

Figure 2.8 Block diagram of the microwave bridge

A final and important component to discuss is the cavity. The cavity is simply a metal box with a shape that resonates with microwaves of a specified frequency, meaning that the cavity stores microwave energy. A consequence is that there are standing waves inside the cavity, which have their electric and magnetic fields exactly out of phase. The magnetic field component drives resonance, so if the sample is placed in an electric field minimum and magnetic field maximum, the highest sensitivity is obtained. Our spectrometer is the Bruker EMX and our microwave bridge contains an X-band source which operates at approximately 9.8 GHz. It is equipped with a goniometer so that the sample may be rotated with respect to the magnetic field.

2.3.2 Coplanar Waveguide Methods

While cavity methods have the advantage of high sensitivity, it is limited in that each cavity is only resonant for a particular frequency. If we require broadband FMR, another method is needed. The technique discussed in this subsection employs a coplanar waveguide, rather than a hollow waveguide to deliver the microwave radiation as in the previously discussed method.

2.3.2.1 Vector Network Analyzer Method

A vector network analyzer (VNA) is a two- or four-port device designed to send and receive electromagnetic signals. The VNA can calculate the scattering parameters, or S-parameters. Our VNA is an Agilent Technologies model 8722ES, a two-port S-parameter network analyzer which operates in the range of 50 MHz to 40 GHz. A schematic of the two-port design is shown below in Figure 2.9.

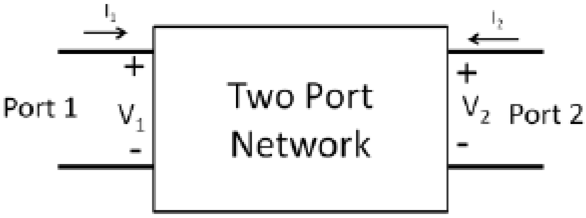

Figure 2.9 General design of the two-port network

The voltages are related by the scattering matrix. This matrix is commonly used in microwave network analysis as it is convenient and easy to deal with [54]. The matrix is seen below in Eq. 2.16.

$$\begin{bmatrix} V_1^- \\ V_2^- \\ \vdots \\ V_N^- \end{bmatrix} = \begin{bmatrix} S_{11} & S_{12} & \cdots & S_{1N} \\ S_{21} & & & \vdots \\ \vdots & & & \\ S_{N1} & \ldots & & S_{NN} \end{bmatrix} \begin{bmatrix} V_1^+ \\ V_2^+ \\ \vdots \\ V_N^+ \end{bmatrix} \tag{2.16}$$

The S_{21} parameter is the one of importance in VNA-FMR. It is a ratio of the input signal to the output. This is relevant since the microwave signal passes through the sample and will be absorbed when resonance occurs. This manifests as a reduced ratio of input to output,

$$S_{21} = \frac{V_2}{V_1} \tag{2.17}$$

and therefore a dip in the S_{21} spectrum corresponds to resonance.

One feature of VNA-FMR is the transmission line. Coaxial cables from the machine's input and output are coupled to the coplanar waveguide (CPW), upon which the sample is placed. A magnetic field is applied in the plane of the sample. A schematic is shown in Figure 2.10 for characterization along the easy axis. It has been shown that VNA-FMR using a CPW is in good agreement with theoretical results as well as cavity-based techniques, and in general gives a high signal-to-noise ratio [55-58].

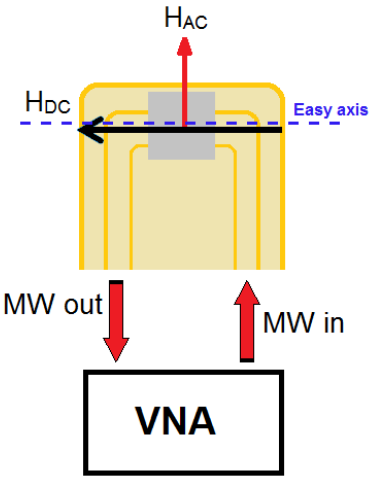

Figure 2.10 Diagram of CPW with sample

An advantage of this method is that a wide range of frequencies can be used. This means that resonance can be measured by holding the frequency constant and sweeping the external field ***H***, similar to cavity FMR, or by fixing ***H*** and sweeping the frequency. A unique and useful representation of the data over a desired range of frequencies and ***H*** values can be constructed by fixing the frequency at the lowest desired value, sweeping the field, and recording the S_{21} parameter. The frequency is then changed to the next increment, and the process repeated. By plotting ***H*** values on the x-axis, frequency values on the y-axis, and S_{21} on the z-axis, as shown below.

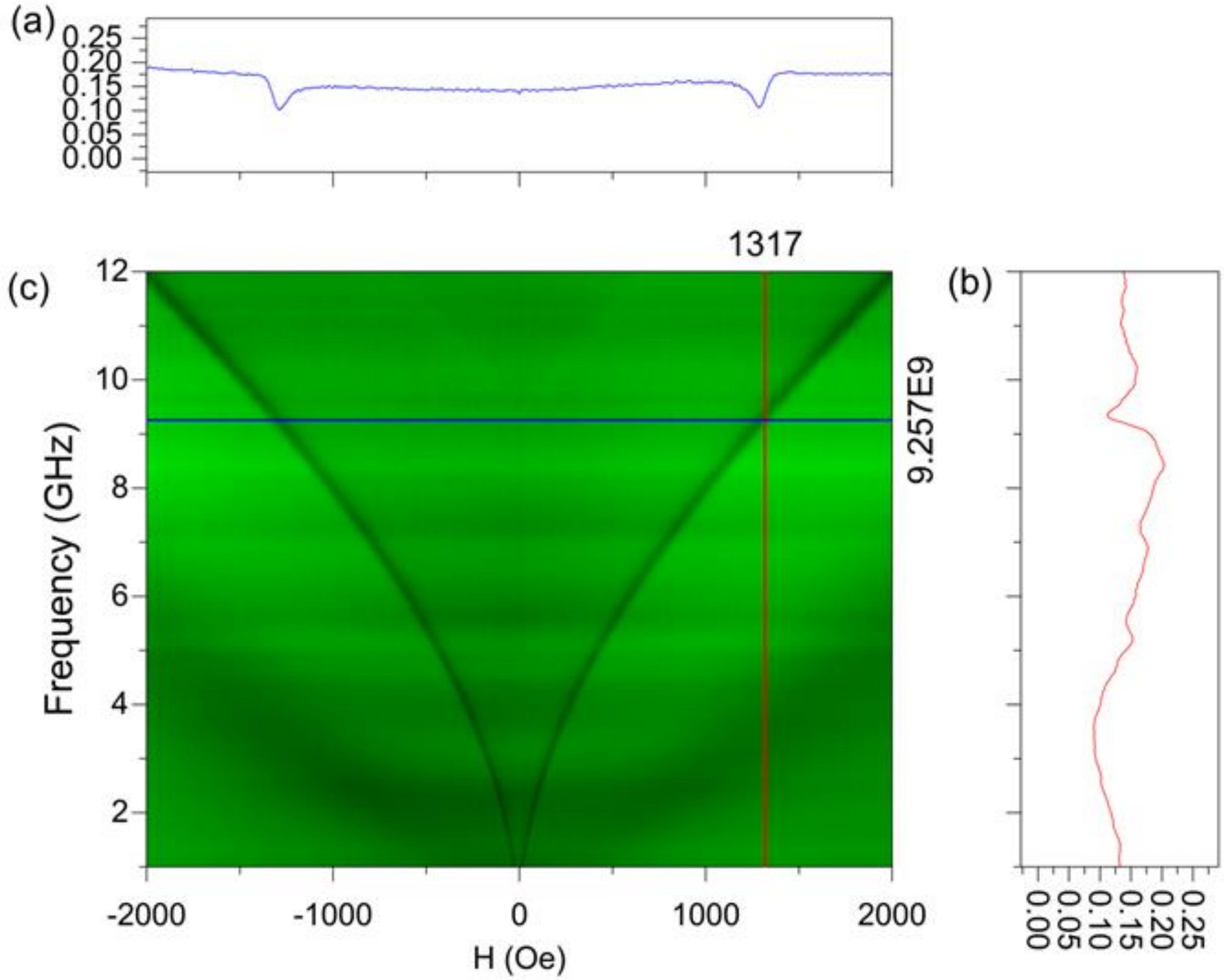

Figure 2.11 Experimentally determined FMR in $Ni_{80}Fe_{20}$ thin film. (a) S_{21} parameter as a function of *H* at the selected frequency (blue line – 9.257 GHz), (b) S_{21} as a function of frequency at selected *H* (red line – 1317 Oe) (c) 3D graph which is a combination of the 2D graphs at every *H* and frequency.

2.3.2.2 Phase FMR and CryoFMR

Recently, there has been some interest in developing broadband FMR spectrometers to measure spectra at low temperatures. PhaseFMR by NanOsc Instruments is a product line of several spectrometers which can be applied at cryogenic temperatures. These instruments use a CPW as in VNA-FMR, although in most cases the frequency range is more limited. The advantage, however, is that the instruments are easy to use and fully controlled by ready-made software.

The spectrometer may be used with an electromagnet which is powered by a supply controlled by the PhaseFMR software. FMR spectra are taken by field sweep holding frequency constant. Transmission is monitored to detect resonance. A lock-in amplifier is used to filter out noise through use of Helmholtz coils connected to an ac source, creating a small modulation field parallel to the applied field. In the case of CryoFMR, the spectrometer is coupled to a waveguide positioned at the bottom of an insert for the Quantum Design Physical Properties Measurement System (PPMS). In this case, the PPMS temperature and magnet are controlled by the CryoFMR software.

Regardless of the method, difficulties still exist in FMR spectroscopy. One complication is the effect of eddy-currents. At microwave frequencies on the order of gigahertz, the penetration depth of the alternating field on the order of tens of nanometers. For this reason, samples are normally composed of thin films or particles [12].

2.4 Susceptibility and Ferromagnetic Resonance

In the preceding sections, we have detailed many ways in which one can study the magnetic susceptibility and resonant absorption of ferromagnetic samples. These techniques have the potential of revealing dynamic properties of the materials under study such as anisotropy and coupling. In both techniques, two fields are applied, $\boldsymbol{H}_{\mathrm{dc}}$ and $\boldsymbol{h}_{\mathrm{ac}}$, generally perpendicular to one another. It has been shown by Spinu *et al.* [51], that the distinction between the two techniques is actually artificial, and it is from this work that this section came to be.

As has been established, the measurement of transverse susceptibility as a function of field presents characteristic peaks at the field values $H_{dc} = \pm H_K = \pm \frac{2K_1}{M}$ and $H_{dc} = H_S$, where H_K is the anisotropy field, K_1 is the anisotropy constant, M is the magnetization, and H_S is the switching field [22, 39, 48, 59]. The peaks $H_{dc} = \pm H_K$ are always present, determined by particles with easy axis perpendicular to $\boldsymbol{H}_{\mathrm{dc}}$. FMR frequency is given by $\omega_r^2 = \gamma^2 \left(H_K^2 - H_{dc}^2 \right)$ for $H_{dc} < H_K$ and $\omega_r^2 = \gamma^2 H_{dc} \left(H_{dc} - H_K \right)$ for $H_{dc} \geq H_K$. Therefore, $H_{dc} = \pm H_K$ corresponds to a resonance frequency of zero, and the peaks in transverse susceptibility are then associated with FMR at zero frequency. In Figure 2.12 below taken from Ref [51], we can see in the main panel the real part of the transverse susceptibility for reduced frequencies $\omega/\omega_{\mathrm{K}}$ as a function of $\boldsymbol{H}_{\mathrm{dc}}$. To the upper right is an exploded view of the spectra near the anisotropy field and at the bottom is FMR spectra for reduced resonance frequency $\omega_{\mathrm{r}}/\omega_{\mathrm{K}}$ as a function of $\boldsymbol{H}_{\mathrm{dc}}$. Note that the peaks near the anisotropy fields for both types of measurements exactly match.

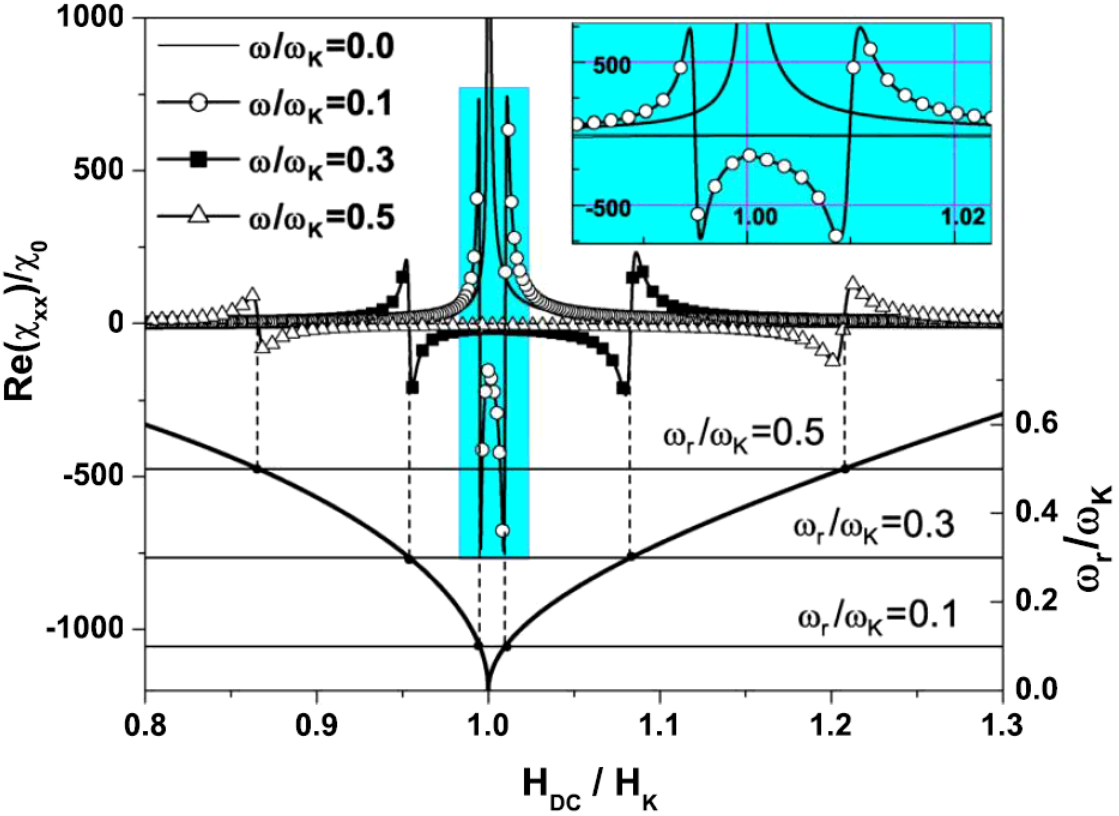

Figure 2.12 Main: Real part of transverse susceptibility as a function of applied field perpendicular to easy axis. Top right: Exploded view near $H_{dc} = H_K$. Bottom: Reduced resonance frequency as a function of applied field perpendicular to the easy axis (Spinu 2006).

2.5 Conclusion

In this chapter, we have studied in detail the measurement techniques which are relevant to the remaining chapters of this dissertation. We have discussed distinctions and similarities of measurement techniques within the static and dynamic regimes. In the chapters which follow, we will see all of the techniques discussed above applied to the study of the magnetization dynamics in coupled magnetic nanostructures.

Chapter 3: Dynamic Critical Curves in Synthetic Antiferromagnets

This chapter details a new FMR probe station built in our labs. We also introduce here the first type of coupled thin film structure studied with this setup – those which are coupled through the Ruderman–Kittel–Kasuya–Yosida (RKKY) interaction. As we will see, these structures may show one of two types of coupling, commonly referred to as ferromagnetic or antiferromagnetic coupling. Although these names are familiar, the RKKY interaction is a form of *indirect* exchange (see Chapter 1, Section 1.2.2) and the ferromagnetic or antiferromagnetic coupling is artificial. For this reason, layers coupled antiferromagnetically are referred to as synthetic antiferromagnets (SAF).

The work detailed in this chapter is a continuation of a study presented in Refs. [60, 61] in which it was shown that angular FMR can be used to help identify whether an RKKY coupled sample is coupled ferromagnetically or antiferromagnetically and drew analogies to the critical curve. Here we further our study and redefine our focus to include only a sample coupled antiferromagnetically. These new data are supported with micromagnetic simulations.

3.1 Introduction to Synthetic Antiferromagnet Structures

Layered structures coupled through RKKY interactions have been particularly interesting and important for their technological applications. Their application is directly related to a controllable coupling strength. One type of RKKY system is SAF.

SAF are trilayer stacks consisting of two ferromagnetic layers coupled across a non-magnetic, conductive spacer. The sign of the exchange constant in Chapter 1 (Eq. 1.5) determines whether the coupling will be ferromagnetic (meaning the magnetizations in the two layers are parallel) or antiferromagnetic (the magnetizations will be antiparallel). This value is a function of the separation between the ferromagnetic layers, which is determined by the thickness of the non-magnetic spacer. It is clear from Figure 3.1 that SAF has a negative *j* value, indicating a condition of antiparallel alignment of magnetization. The coupling arises from Friedel-like spatial oscillations in the spin density of the conductive spacer, leading to a coupling between the ferromagnetic layers which oscillates with separation *r* [62].

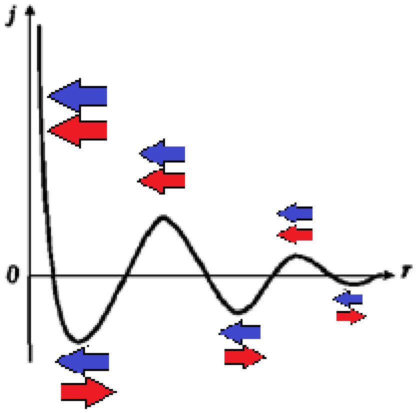

Figure 3.1 *J* as a function of spacing *r* with arrows indicating ferromagnetic coupling ($j > 0$) and antiferromagnetic coupling ($j < 0$)

A clearer idea of how susceptibility is affected by the sign of *j* can be seen in Figure 3.2 [63], which shows the simulated major hysteresis loops (MHL) for a ferromagnetically-coupled sample (right) and SAF (left). The MHL is one of the quickest ways to identify antiferromagnetic coupling. As we shall see, however, this is not the only way to identify the coupling.

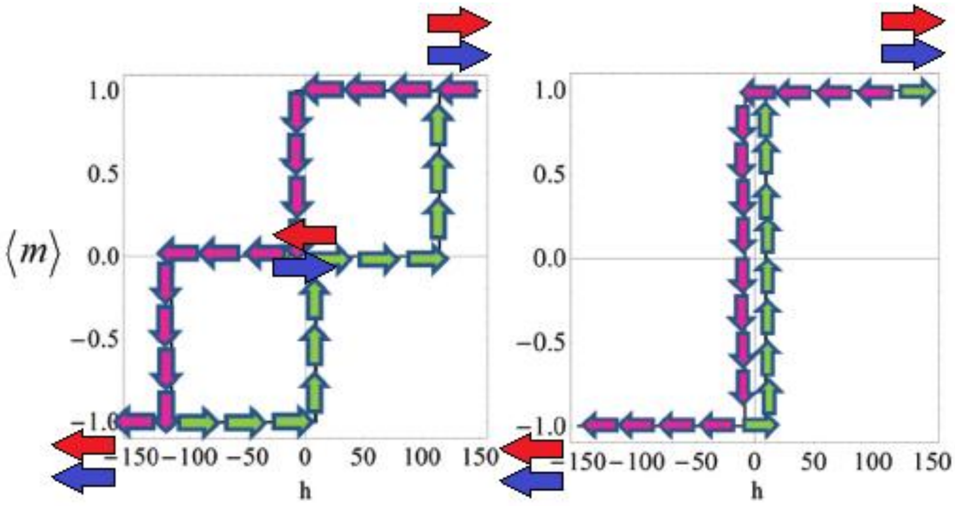

Figure 3.2 Simulation with path direction for structures displaying antiferromagnetic coupling (left) and ferromagnetic coupling (right). The red and blue arrows represent the magnetization of each layer at different points on the MHL (Forrester 2013).

An illustration of an RKKY-coupled structure can be seen in Figure 3.3. Due to controllable coupling strength and thermal stability [64-67], SAF has applications in magnetic sensors, perpendicular recording media, exchange-coupled composite media, and magnetic random access memory (MRAM) components [26, 67-77]. Recently, it has even been shown that SAF nanoparticles show potential for use as contrast agents in magnetic resonance imaging [78]. It has also been suggested that SAF structures may help to understand spin-orbit torque switching [79]. The use of SAF in applications is dependent on its interlayer exchange coupling which determines the individual magnetization reversal of the ferromagnetic layers [9].

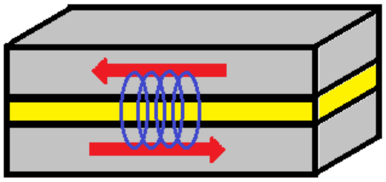

Figure 3.3 Schematic representation of the SAF showing the coupling of the two ferromagnetic layers.

3.1.1 SAF Applications

The coupling observed in SAF has been investigated for its applications since 1986 [80]. This section will briefly cover some SAF applications and reasons why they are so applicable.

Due to enhanced thermal stability [81, 82], SAF have been applied in recording media as the soft under-layer. The bottom layer and recording layer are coupled antiferromagnetically across a thin metallic spacer. The exchange coupling enhances thermal stability, and one study has reported that the coupling strength may be manipulated through changing the thickness of the bottom layer [83].

In a magnetic tunnel junction (MTJ), a pinned layer is separated from a free layer by a non-magnetic spacer. These devices are used in high density read heads and MRAM applications. The MTJ is found in sub-micron cells, in which a larger switching field is required as size decreases due to the increase in the demagnetizing field from the cell edges. The use of SAF structures in these devices reduces the required switching field.

An important application of SAF is to MRAM and toggle-MRAM [7]. The MRAM writing operation is shown in Figure 3.4 [84]. The selected MTJ highlighted in red is located between the selected word line and bit line (green). Current flows in the direction of the blue arrows which induces a magnetic field in a circular direction. The vector sum of the magnetic fields must be large enough to switch the MTJ state, while the single field of the word line and single field of the bit line must be small enough to maintain the state of the half-selected MTJ which are found along the selected word line or bit line. The astroid to the right is the ideal switching curve of the MTJ free layer. The astroid shows how the free layer may be magnetized to state 1 or state 0. For example, in this figure, the bit line lies along the x-axis and the word line along the y-axis. If the magnetic field begins from zero (origin of the coordinate system) and increases to the right of the y-axis and astroid, and then returns to the origin, the MTJ will be magnetized to the right, or state 1. If it instead increases to the left of the astroid and returns to zero, the MTJ will be left in the magnetization state 0. If the field never goes beyond the astroid, the MTJ state remains unchanged. It is clear then that the fields to switch the selected MTJ must lie outside the astroid while for the half-selected MTJs the fields must not exceed the boundary of the astroid.

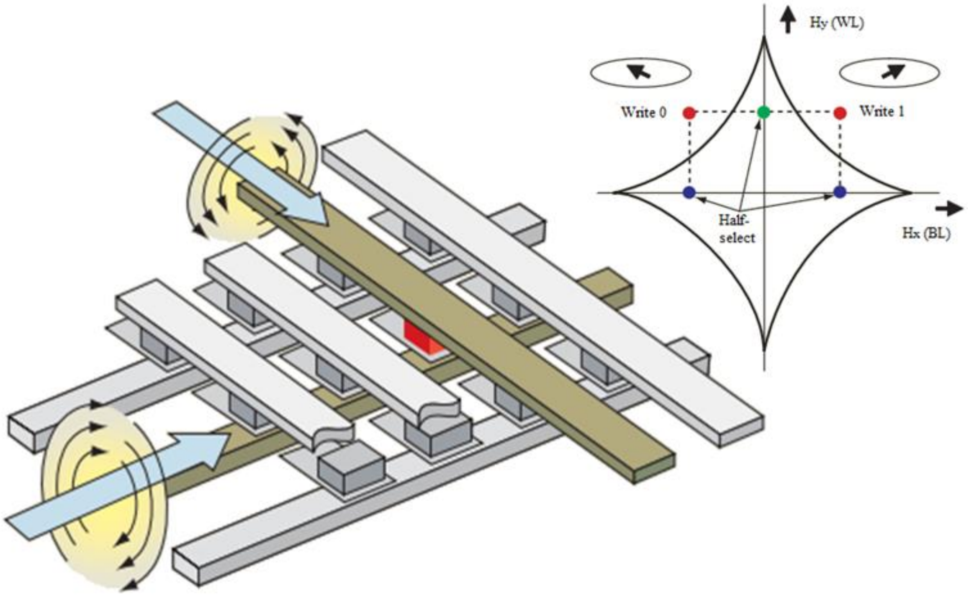

Figure 3.4 MRAM write operation and ideal critical curve describing the switching in the MTJ free layer (Maffitt 2006).

With operations close to the curve boundary, there is a risk of thermally-activated switching [85]. To deal with this problem, the “toggle-mode” MTJ was developed [72]. An illustration of this is seen in Figure 3.5 [7]. This structure still contains a pinned layer and a free layer, except now the free layer itself is a SAF. In order to achieve a successful toggle, the applied field must trace a path in the applied field plane that encloses the “spin-flop” point. This device in not as susceptible to half-select disturbs which do not trace a path that encloses the spin-flop point. Also, since the free layer has zero net magnetization, it is unaffected by the state of nearby devices.

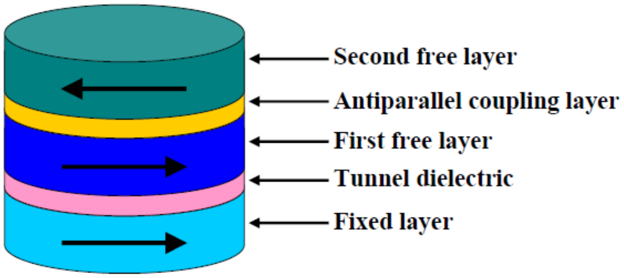

Figure 3.5 Toggle MTJ structure (Radu 2008).

3.1.2 Free Energy and Magnetization Dynamics in SAF

The free energy in a SAF structure, in general, includes a Zeeman term and the exchange term. Anisotropies, such as shape, uniaxial, and out-of-plane, may be present as well. For our sample, magnetization and uniaxial anisotropy was in the plane of the sample.

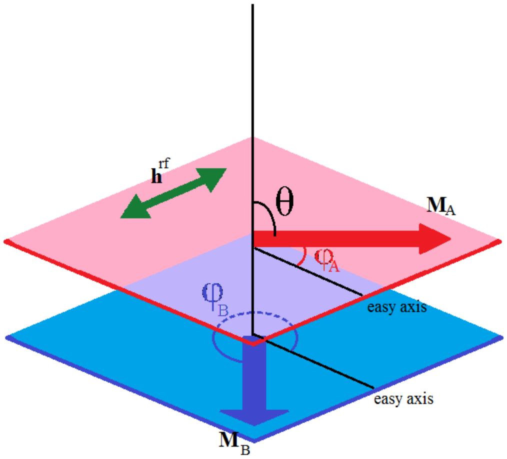

Figure 3.6 Schematic of the ferromagnetic layers in SAF. The magnetization vectors are in the plane of the sample and defined by the angles θ, φ_A and φ_B. The H_{dc} (not shown here) and h_{rf} are in the plane of the sample in our experiments.

Refer to Figure 3.6 for the following discussion. The Zeeman and uniaxial anisotropy contributions [12] can be written as

$$E(\varphi) = -MH\cos(\varphi_{\mathrm{H}} - \varphi_i) + K_0 + K_1 \sin{\varphi_i}^2 + K_2 \sin{\varphi_i}^4 + \cdots \tag{3.1}$$

where the first term on the right hand side in the Zeeman energy and the others are anisotropy terms. φ_{H} is the direction of $\boldsymbol{H}_{\mathrm{dc}}$, and the subscript i refers to the top and bottom layers, A and B

respectively. M is the magnetization and K_n's are the anisotropy constants. Therefore the energy is minimized when $\varphi_i = 0°$, i.e. along the easy axis.

The contribution due to the coupling must take into account the coupling constants J_1 and J_2, the so-called bilinear and biquadratic coupling constants between the two layers [86]. It has the form

$$E_{\text{int}} = J_1 \frac{\mathbf{M_A} \cdot \mathbf{M_B}}{|\mathbf{M_A}||\mathbf{M_B}|} + J_2 \left\{ \frac{\mathbf{M_A} \cdot \mathbf{M_B}}{|\mathbf{M_A}||\mathbf{M_B}|} \right\}^2 \tag{3.2}$$

or, equivalently,

$$E_{\text{int}} = J_1 \cos(\varphi_{\text{A}} - \varphi_{\text{B}}) + J_2 \cos^2(\varphi_{\text{A}} - \varphi_{\text{B}}) \tag{3.3}$$

3.2 Critical Curves in SAF

3.2.1 Sample Description

The sample studied is a trilayer stack of FeCoB ferromagnetic layers coupled antiferromagnetically across a 1.6 nm spacer of Ru. The sample was deposited on glass at room temperature by dc magnetron sputtering by Dr. Ganping Ju at Seagate Technology. During deposition, a small magnetic field was applied in the plane of the thin films in order to induce a uniaxial anisotropy. An overcoat of C was deposited on top for sample protection. The dimensions of the sample were $5\ \text{mm} \times 5\ \text{mm}$, with a total sample thickness of approximately 30 nm. A schematic of this sample is shown in Figure 3.7 and a TEM image of the sample cross-section can be seen in Figure 3.8.

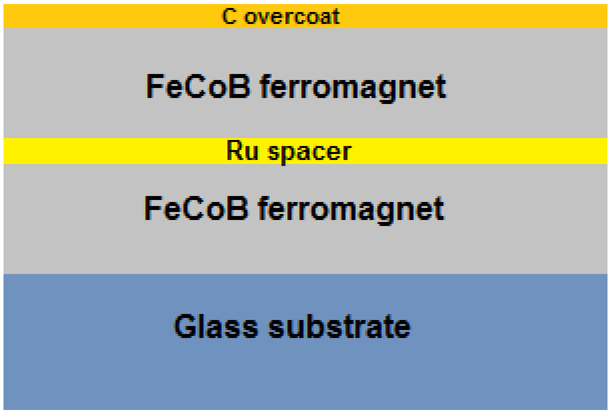

Figure 3.7 Schematic of SAF cross-section

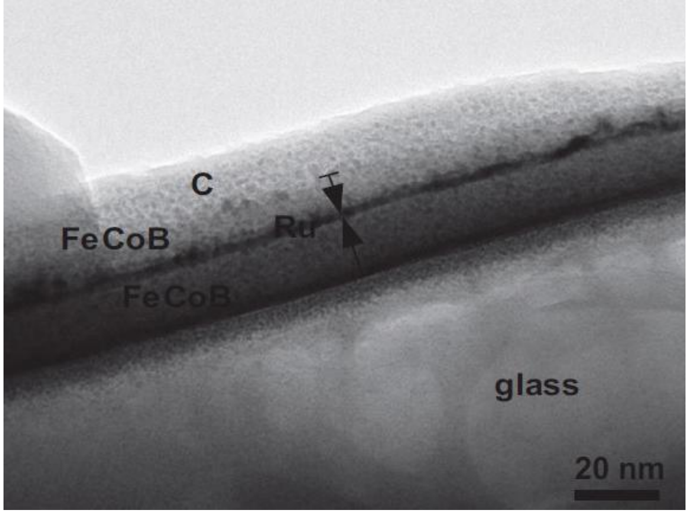

Figure 3.8 TEM cross-section image of SAF sample.

The MHL for this sample was recorded using Lake Shore’s PMC MicroMag 3900 Vibrating Sample Magnetometer (VSM). Clear antiferromagnetic coupling was observed for this sample. Figure 3.9 shows the MHL along the easy and hard axes. A broadband FMR curve using Vector Network Analyzer (VNA)-FMR was recorded along the anisotropy axis and is shown in Figure 3.10(b) along with a continuous wave spectrum (a) and S_{21} as a function of frequency graph (c).

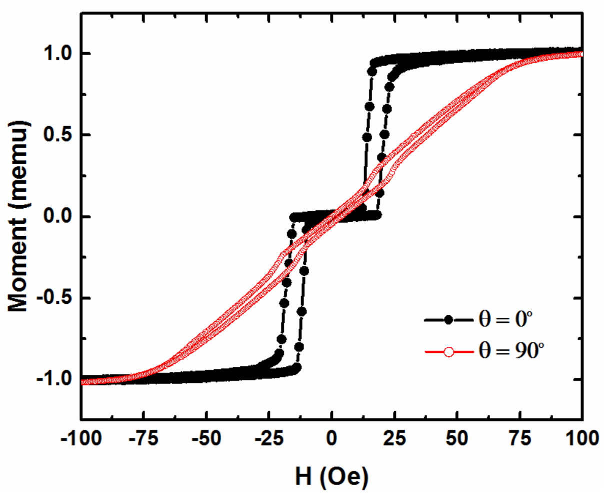

Figure 3.9 MHL along the easy axis (black) and hard axis (red)

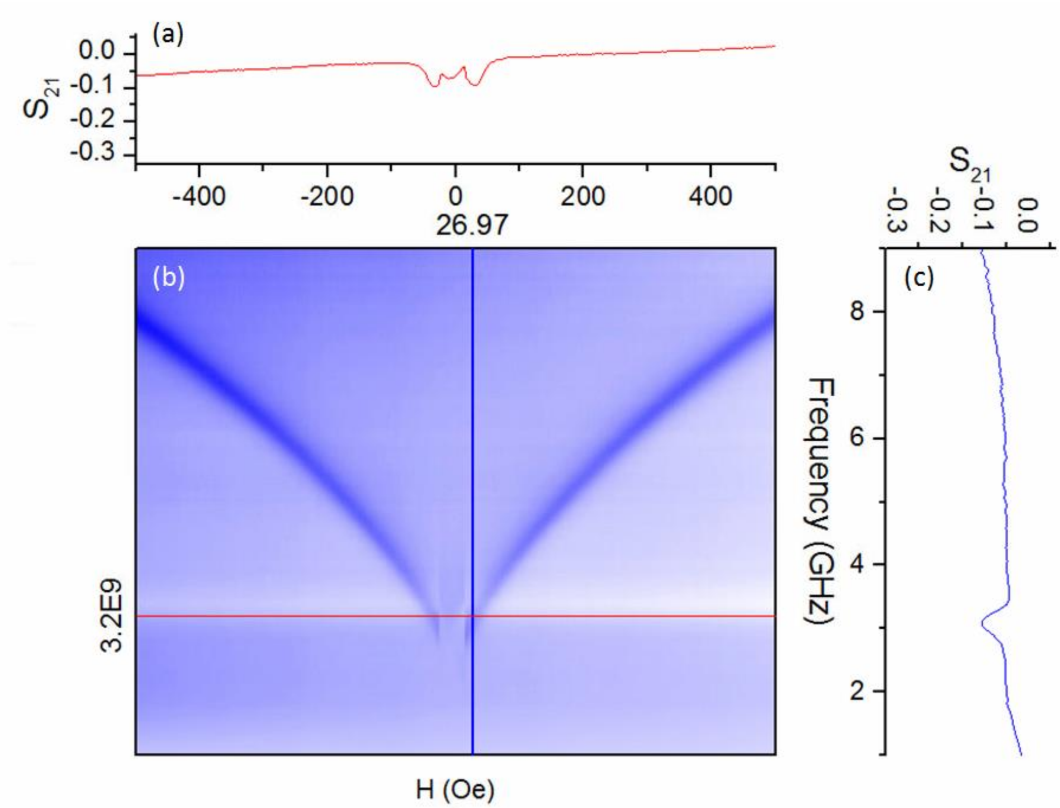

Figure 3.10 FMR curves for SAF sample: (a) S-parameter vs. H, (b) broadband FMR curve, and (c) S-parameter vs. frequency

A separation in the lower frequency region of the descending and ascending branches of the FMR curve corresponds to the splitting in the MHL. Since in SAF there are two magnetization reversals, the broadband curve is split and symmetry is observed across the first and second switching events. Figure 3.11 shows a detailed view of this.

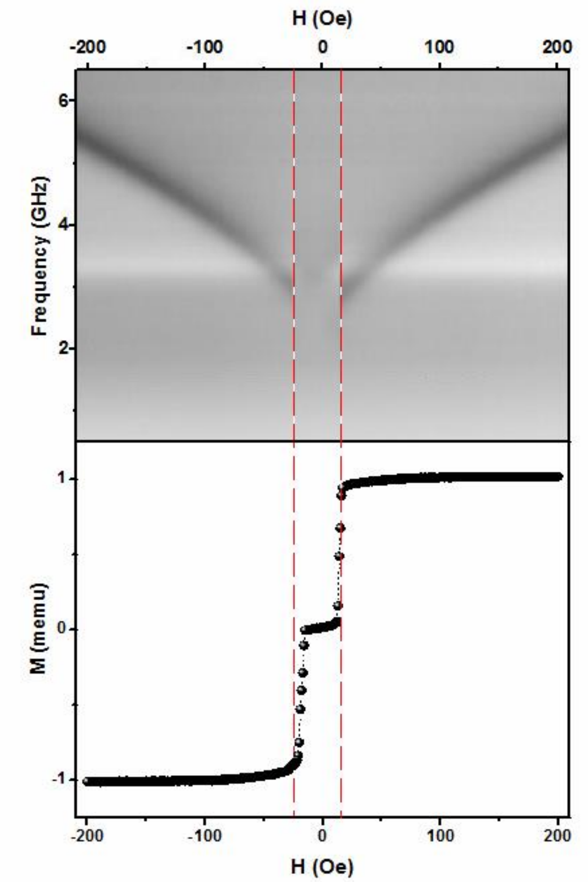

Figure 3.11 Broadband (top) and MHL (bottom) for SAF sample for descending fields showing corresponding splitting regions in the two graphs

3.2.2 Critical Switching Curve

The static critical curve (CC) was obtained using the tunnel diode oscillator (TDO) method detailed in Refs. [7-9]. The sample was placed in a sensing coil with the ac field perpendicular to the sample's easy axis. Both the ac and dc magnetic fields were in the plane of the sample. The dc magnetic field ($\boldsymbol{H}_{\text{dc}}$) was created by a double Helmholtz coil which is capable of achieving a uniform magnetic field in any direction within the plane of the sample. $\boldsymbol{H}_{\text{dc}}$ was ramped from positive saturation to negative at different angles with respect to the easy axis in the range 0° to 180° in increments of 2°. Throughout the experiment, the sensing coil remained fixed in place. The susceptibility was recorded at every step of $\boldsymbol{H}_{\mathrm{dc}}$. From the angular dependent susceptibility measurements, the CC can be constructed. Figure 3.12 shows the CC and how it is constructed from the susceptibility curve as well as how it relates to the MHL.

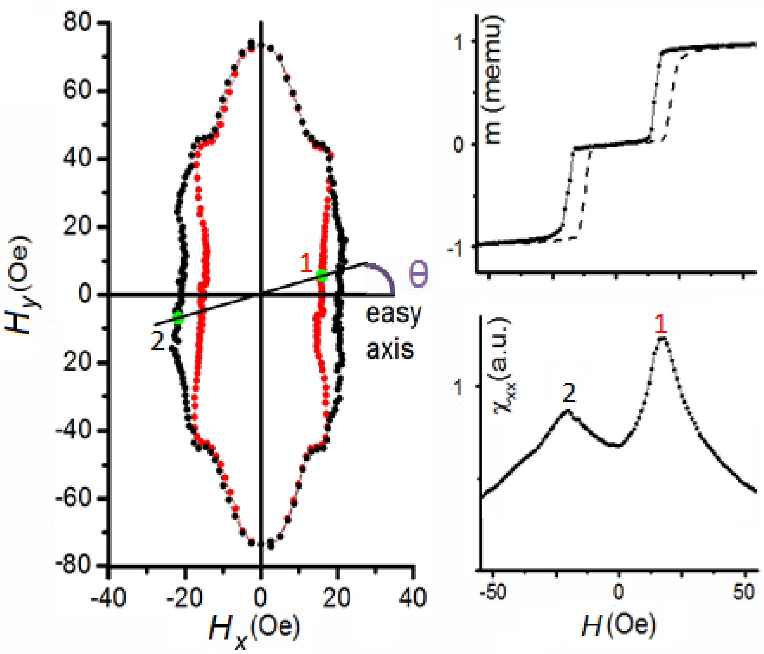

Figure 3.12 CC (left) determined through susceptibility curves (bottom right) and corresponding MHL (top right)

As known from the MHL, there is clear antiferromagnetic coupling in this sample. Due to the non-synchronous layer switching, the CC contains both inner and outer curves we can expect, unlike what we would see in a single-layer system. In that case, a CC with a single branch is expected and observed experimentally, similar to the Stoner-Wohlfarth (SW) astroid for a single-domain particle.

3.2.3 New Experimental Setup and Dynamic Critical Curve

When a microwave field is present, the static CC is no longer valid and must be replaced by a representation which takes into account the dynamic effects. In order to accomplish this, we construct a *dynamic critical curve* (dCC).

To produce a dCC, a new probe station for CPW-FMR had to be constructed. The custom-built setup was originally described in Ref. [60, 61], but has been modified somewhat to fine-tune the original study, as described in this chapter.

The probe station has two levels, with the lower level housing the field-projection magnet. The magnet sits on a rotation stage capable of 360° rotation and is controlled by computer. The second level is the where the sample is actually probed. This probe station is adaptable to two different types of CPWs. Micron-sized CPWs or commercial CPWs (as in this experiment) may be used.

For micron-sized CPWs, a plastic stage is fixed in place above the magnet, and the appropriate microwave probe tips are mounted on two arms on either side of the stage, which are connected to the output and input of the VNA. The arms are brought in, such that the probe tips can make contact with the Ground-Signal-Ground (GSG) lines of the waveguide. A microscope mounted on a ball-bearing boom stand is available for assistance with making contacts. This type of CPW has the advantage of being able to be placed much closer to the magnet, and experiments utilizing this waveguide have less limitations of magnetic field. However, the sample in these cases must be extremely small, which is not always practical or desirable. For larger surface area samples, the much larger commercial CPW is a better option. For commercial-grade CPWs, the plastic stage and probe arms are removed and replaced by a plastic holder which suspends the CPW’s sample area over the point of constant magnetic field. The VNA output and input are connected directly to the CPW.

A bipolar power supply powering the projected field electromagnet is responsible for the magnetic field. The magnitude of the field is determined in the sample location by the LabVIEW program from the current input to the magnet based on a current-to-field calibration. For this reason, it is extremely important to ensure accurate calibration in the sample space. The calibration must be redone any time the sample space changes, i.e. in the case of switching waveguides, and should be periodically checked with a Gaussmeter in between experiments.

For this study, the probe station was rebuilt on an anti-vibration table, which allowed us to probe frequencies much lower than originally thought possible. In a previous experiment [61], the FMR signal was thought to have disappeared below 2.5 GHz but was actually masked by noise. Incorporating the anti-vibration table increased the signal-to-noise ration and allowed us to probe frequencies as low as 1.75 GHz for the sample studied here.

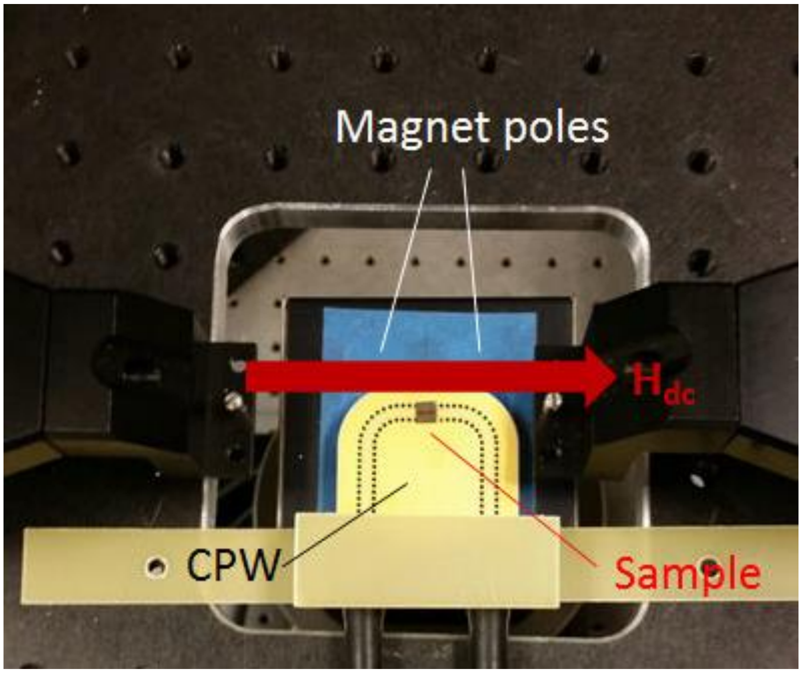

Figure 3.13 Picture of top level of probe station with CPW and sample in place.

The sample was placed on the signal line of a commercial grade CPW (see Figure 3.13 above) connected to the VNA such that the magnetic field component of the microwave ($\boldsymbol{h}_{ac}$) was along the hard axis of the sample and perpendicular to the easy axis. The field-projector magnet supplied the uniform magnetic field ($\boldsymbol{H}_{dc}$) in the plane of the sample. The geometry of the fields with respect to one another, as well as to the anisotropy axis is seen in Figure 3.14, referred to as "Configuration 1".

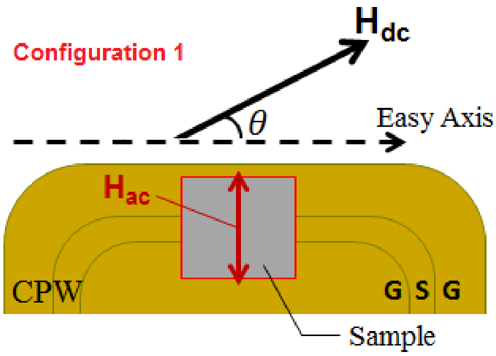

Figure 3.14 Schematic of field geometry with respect to the sample's anisotropy.

$\boldsymbol{H}_{\text{dc}}$ was ramped down from positive saturation to negative in steps of 1.5 Oe. The FMR absorption was measured by using the VNA to probe the transmission coefficient S_{21} at the desired frequency at each increment of $\boldsymbol{H}_{\text{dc}}$. Once the final field value was reached and the recording of S_{21} was complete, the magnet was turned by 5° and the experiment began again. This process was repeated at 5° increments from 0° to 175°. This is all that is necessary, since $\boldsymbol{H}_{\text{dc}}$ is ramped from positive to negative saturation, and therefore a positive and negative FMR absorption is recorded at every angle. For example, the "positive fields" side of a scan will be 0° and the "negative fields" side of the same scan will be 180° since the magnetic field has changed directions (see Figure 3.15(a)). Thus, this will give one absorption curve for every angle studied. In the end, a complete polar chart containing FMR information can be constructed in analogy to the CC. An example is shown in Figure 3.15(b) for 3.5 GHz. The continuous-wave FMR graph (Figure 3.15(a)) can be thought of as a slice out of the broadband curve (see Figure 3.10). The lowest points in the S_{21} vs. H graph correspond to maximum resonant absorption. These points in the dCC are shown by the darkest blue color while maximum transmission (minimum absorption) is the lighter area of the graph.

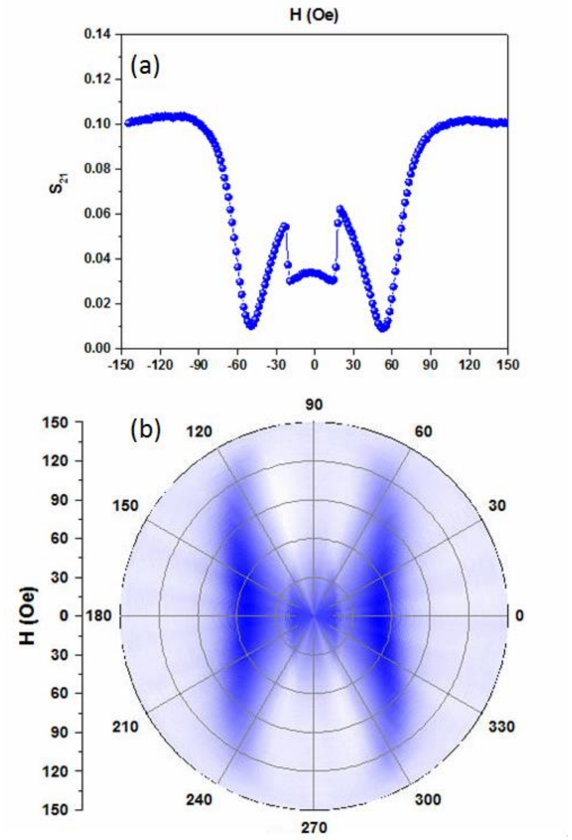

Figure 3.15 (a) Continuous-wave FMR for SAF at 3.5 GHz along 0° (positive x-axis) and 180° (negative x-axis) and (b) SAF dCC at 3.5 GHz.

The dCC is a mechanism for dynamically probing the anisotropy effects in a magnetic system. As seen below in Figure 3.16, the coupling effects of this particular system are also preserved. These features are particularly evident between 3 and 3.5 GHz where double resonances occur. This phenomenon is expected based on the broadband curve of Figure 3.10.

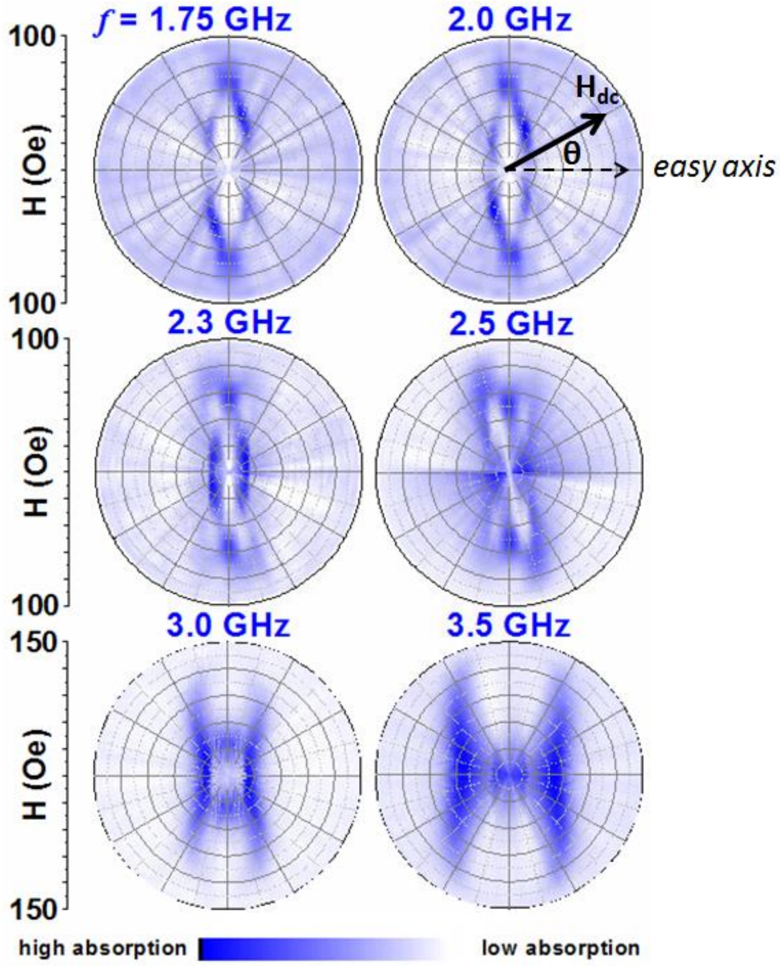

Figure 3.16 dCC for selected frequencies. Field geometry and easy axis are indicated

The double resonances can be expected by comparison of the MHL and broadband curve in Figure 3.11 and are associated with the successive switching of the SAF's ferromagnetic layers. It is appropriate here, however, to look closer at this phenomenon to better show the symmetries across the magnetization reversal. Figure 3.17 compares a single frequency (3.2 GHz) FMR curve to the MHL for a closer look at the double resonances due to SAF coupling.

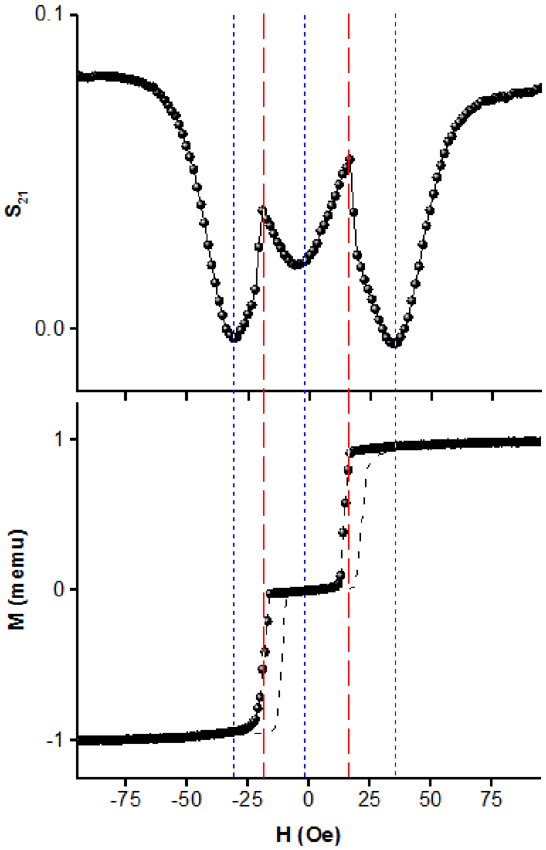

Figure 3.17 Continuous-wave FMR at 3.2 GHz (top) highlighting the double resonances and how they relate to the MHL (bottom). Blue guidelines are placed at the resonances while red guidelines are placed at the switching fields.

Notice that as the frequency is lowered, the dCC takes on a shape much more similar to the static CC. The two types of critical curves are compared directly in Figure 3.18. An interesting feature occurs around 2.3 GHz and lower frequencies. The dCC is observed to move inside of the CC. This corresponds to the area of the MHL unique to SAF – the state in which the magnetization in one ferromagnetic layer has reversed its direction but the second layer has yet to switch, creating the split in the MHL. For a typical ferromagnetic film, one would expect to see symmetric resonances across the branch of the CC (or approximately across 0 Oe above saturation). In the case of SAF however, this feature implies that for low frequencies, resonance only occurs in the state of antiparallel magnetizations.

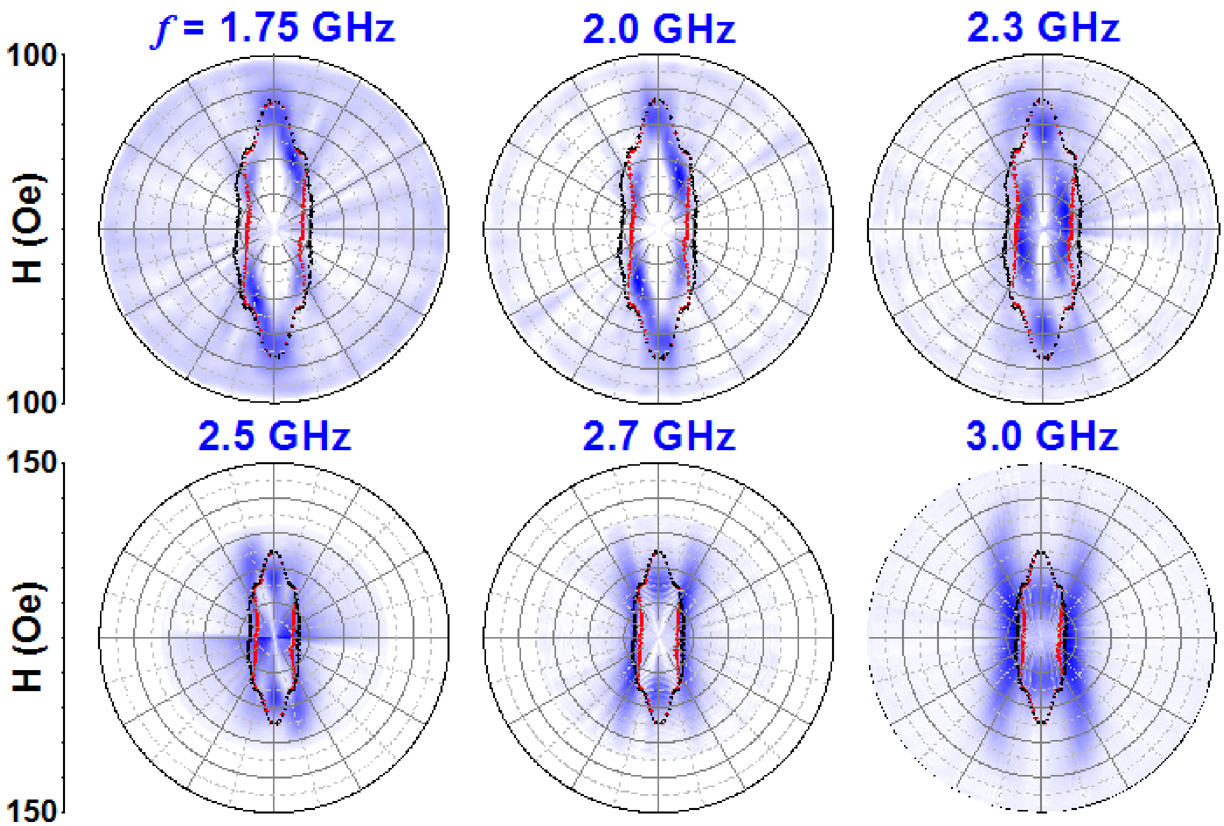

Figure 3.18 Static CC compared to dCC for selected frequencies

Another interesting feature is that the low frequency dCCs are closed at 90°. Normally one would not expect to see clear FMR in this orientation since $\boldsymbol{h}_{\mathrm{ac}}$ and $\boldsymbol{H}_{\mathrm{dc}}$ are parallel. The reason this occurs in low frequencies here is that when $\boldsymbol{H}_{\mathrm{dc}}$ is applied at 90° (which also corresponds to the hard axis – see Figure 3.14) the magnetic moment $\boldsymbol{m}$ is aligned with it only for fields outside of the CC. Inside of the CC there is a non-zero angle between $\boldsymbol{H}_{\mathrm{dc}}$ and $\boldsymbol{m}$ as well as between $\boldsymbol{h}_{\mathrm{ac}}$ and $\boldsymbol{m}$. For this reason, the ac field is able to determine an oscillation of $\boldsymbol{m}$.

For higher frequencies, the dCC is limited in that FMR absorption is unable to be determined outside of the CC at 90°, i.e. when $\boldsymbol{m}$ is aligned with $\boldsymbol{h}_{\mathrm{ac}}$. This is observed as a gap in the graph as fields approach 90° (and 270°). Therefore, with this sample orientation on the CPW, we lose information about the hard axis, and a complete dynamic characterization is lacking. To remedy this issue we turn the sample on the CPW to Configuration 2 (Figure 3.19) and repeat the experiment.

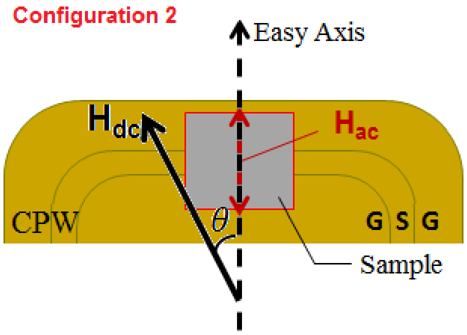

Figure 3.19 Schematic of field geometry with respect to sample's anisotropy for Configuration 2.

The polar chart produced by these measurements will contain the hard axis characterization and will lack easy axis characterization, since in this new orientation the easy axis is parallel to $\boldsymbol{h}_{ac}$. If we overlay this new polar graph with the original, we will have a complete dCC. Examples of this are shown in Figure 3.20 with the original graph in blue and the new graph in green.

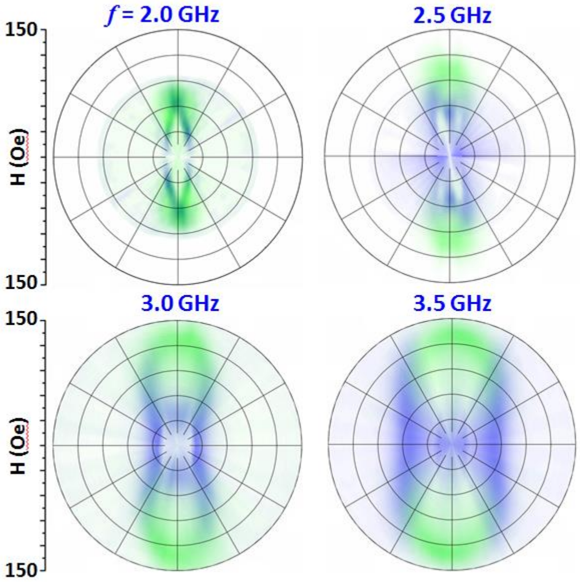

Figure 3.20 Superposition of dCC obtained for selected frequencies in Configuration 1 (blue) and Configuration 2 (green).

3.3 Micromagnetic Simulations and Macrospin Model

Support with modeling and simulations came through collaboration with Dr. Dorin Cimpoesu of Iasi University, Romania. The following discussion is based on the work of Cimpoesu in Ref [87]. A simple but sufficient model for this system is to assume that the magnetization in each layer can be described as a pseudo-single particle, with effective fields of each layer containing the anisotropy, antiferromagnetic coupling, the applied field, and the phenomenological demagnetizing field. The classical SW model predicts the same saturation field both along the easy axis and perpendicular to it for a single-domain particle [6]. To overcome this limitation, a generalized SW model is used which can describe the angular dependence of the switching field in non-single domain particles while maintaining the macrospin hypothesis [88]. This model uses a phenomenological expression for the anisotropy to describe observed dependencies of the switching field on the field orientation [4, 5].

The static critical curve for the system was obtained by solving the following equations:

$$\frac{\partial F}{\partial \varphi_A} = \frac{\partial F}{\partial \varphi_B} = 0 \tag{3.4}$$

$$\left(\frac{\partial^2 F}{\partial \varphi_A^2}\right)\left(\frac{\partial^2 F}{\partial \varphi_B^2}\right) - \left(\frac{\partial^2 F}{\partial \varphi_A \partial \varphi_B}\right)^2 = 0 \tag{3.5}$$

where F is the free energy of the system. The angles φ_i have the same meaning as before.

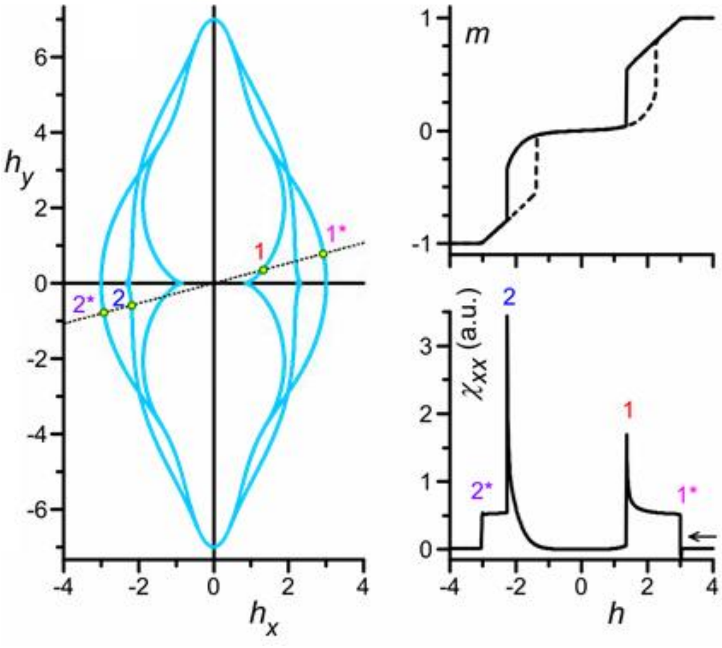

Figure 3.21 Simulated critical curve determined through simulated susceptibility curves (bottom right).

Figure 3.21 shows the simulated critical curve for the simulated particles with antiferromagnetic coupling (compare to Figure 3.12). For the dCC, the coupled LLG equation is integrated to find the time evolution of the magnetization. The energy absorbed from $\boldsymbol{h}_{\mathrm{ac}}$ by the system is proportional to the product $f_{ac}\chi''$, where f_{ac} is the frequency and χ'' is the imaginary part of the complex susceptibility [89-92]. The polar contour representations seen in Figure 3.22 are built by simulating the χ'' field variation with $\boldsymbol{H}_{\mathrm{dc}}$ along different directions. The ac frequencies in the figure, f_{ac}, are in units of the Kittel frequency.

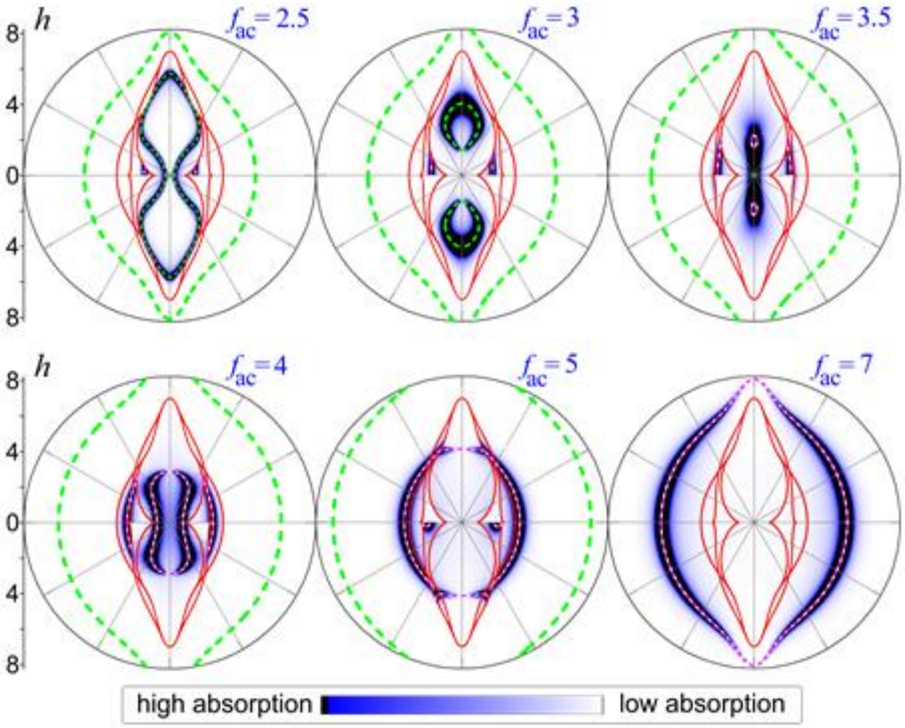

Figure 3.22 Simulated imaginary susceptibility computed on the descending branch of the MHL.

3.4 Summary

The static and dynamic properties of a FeCoB trilayer were used to characterize the anisotropy in the antiferromagnetically coupled system based on critical curve formalism. While the critical curve provides information about the anisotropy through the irreversible magnetization reversal in each layer, the presence of a microwave excitation field requires a new model. We have therefore presented a simulation-supported experimental characterization of the magnetization dynamics in SAF in both static and dynamic regimes [87].

Chapter 4: Dynamic Critical Curves in Exchange Bias Structures

In the follow sections, we discuss a type of anisotropy introduced briefly in Chapter 1. This anisotropy, known as exchange bias or exchange anisotropy, was first reported by Meiklejohn and Bean [23]. As described in Section 1.2.3.4 this experiment was performed on a set of Co-CoO nanoparticles. It was shown that the most notable attribute of the exchange biased structure is a displaced MHL.

The focus of this chapter is to measure exchange bias in a series of samples and to determine the static and dynamic critical curves of exchange-biased systems. In the samples under study, the antiferromagnetic layer of the structure is systematically increased across the set of samples. It is not uncommon to read about the still-uncertain properties of the exchange bias phenomenon [93], although it has been known and study since the famous 1956 paper.

4.1 Introduction to Exchange Bias Structures

A typical ferromagnetic material displays a symmetric major hysteresis loop (MHL) centered at zero field as demanded by time-reversal symmetry. However, the work of Meiklejohn and Bean showed that the MHL of slightly oxidized Co particles are distinctively displaced [94].

In the Co-CoO system, one attributes the unique properties observed to the exchange coupling between the spins of the ferromagnetic and antiferromagnetic materials at the interface between them. Above the Néel temperature, T_N, (about 20°C for CoO), the oxide is little affected by the application of a strong magnetic field while the Co is magnetically saturated. The spins of the Co in the oxide layer at the interface are forced into parallel orientation with the adjoining spins in the ferromagnetic layer due to the positive exchange force. When the system is field-cooled far below T_N, antiferromagnetic ordering is set in the CoO layer. The spin arrangement is seen in Figure 4.1. The magnetic moments in the CoO have chosen an axis of magnetization that minimizes their energy of interaction with the Co moments across the interface [95].

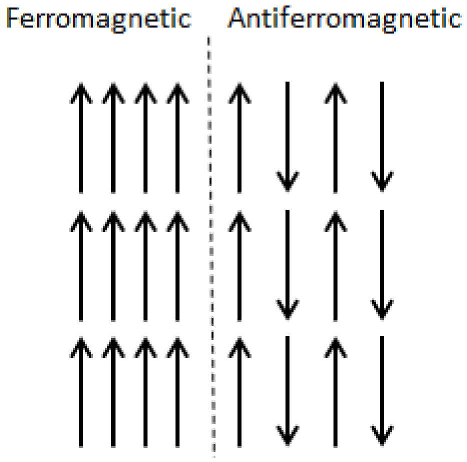

Figure 4.1 Arrow representation of the ferromagnetic/antiferromagnetic system

Removing the magnetic field does not affect the spin arrangement. Applying a strong field in the direction opposing the magnetization (downward, in this case) causes the spins of the Co to reverse, causing the coupling across the interface to try to reverse the spin system in the CoO (Figure 4.2 .

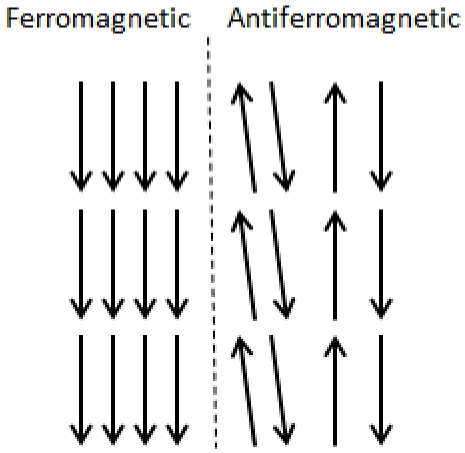

Figure 4.2 Arrow representation of the magnetization reversal in the ferromagnetic/antiferromagnetic system

As is pointed out by Cullity and Graham in Ref [12] and briefly discussed in Chapter 1, there are evidently three requirements for exchange bias to occur. The first is field-cooling through T_N in order to give an easy direction to the specimen. The second is intimate contact between the two materials, allowing the exchange interaction to occur. The last is strong crystalline anisotropy in the antiferromagnet.

An important distinction to revisit is the fact that the exchange anisotropy is a unidirectional anisotropy, contrary to the uniaxial anisotropy often observed in materials where anisotropy is induced during fabrication or in materials which exhibit magnetocrystalline anisotropy. The difference is seen in the MHL. In uniaxial anisotropic systems, the same result is obtained when measuring the material along its easy axis in either the 0° or 180° orientation due to the symmetry of the magnetization reversal. However, when measuring a system along a unidirectional anisotropy, the MHL will be displaced in one direction. Measuring at 180° to the unidirectional anisotropy will give a loop displaced in the opposite direction. Measuring perpendicular to the unidirectional anisotropy gives a loop which is not displaced but often elongated and nearly reversible as this axis in general is taken to coincide with the ferromagnetic hard axis. Unidirectional anisotropy is proportional to the first power of cosine, whereas uniaxial anisotropies are written as proportional to the cosine squared.

$$E = -K \cos\theta \tag{4.1}$$

For convenience, exchange bias is now often studied in a layered geometry (see Figure 4.3 from Ref [93]) and has been for over 40 years [96-99]. The deposition of exchange-biased is an important process, and the order of deposition of magnetic layers is important. When the ferromagnetic layer is deposited first and antiferromagnetic second in a magnetic field, the antiferromagnetic domains tend to be coupled in alignment with the direction of the ferromagnetic layer, producing exchange bias fields as well as an enhanced coercivity [96]. The values of the exchange bias field H_{eb} and coercive field H_c depend on the thicknesses of the ferromagnet and antiferromagnet layers [97, 98, 100, 101]. H_{eb} has been found to be inversely proportional to the thickness of the ferromagnetic layer [94]. With increasing antiferromagnetic thickness, H_{eb} been shown to increase to some maximum value before levelling off [102-104].

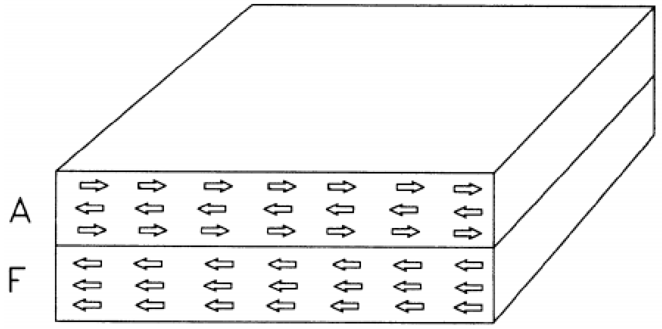

Figure 4.3 Schematic of exchange-biased layer structure (Stoecklein 1988).

4.1.1 Applications of Exchange Bias

Exchange bias has been studied extensively both theoretically and experimentally since the discovery of the phenomenon, particularly between the late 1980’s to early 2000’s, and has found technological applications in magnetoresistive heads biasing and spin valve structures [25, 53, 97, 98, 100, 101, 105-110]. It is of special interest here to discuss the spin-valve device further, as the synthetic antiferromagnet, introduced in the previous chapter, is a critical component.

It is known that current in ferromagnetic metals is carried by spin-polarized electrons, arising from the spin-dependent scattering of the majority and minority spin-polarized electrons, “up” and “down”, respectively [111]. These currents are manipulated by constructing inhomogeneous magnetic systems, such as the synthetic antiferromagnet. Systems such as these exhibit large changes in resistance as the magnetization of neighboring layers is changed, a phenomenon known as giant magnetoresistance (GMR) [112-117]. This effect has found application in the form of a highly sensitive magnetic recording read head for magnetic hard disk drives [118]. An important concept in the engineering of devices which take advantage of GMR is the fixing of the direction of the magnetic moment of the individual magnetic layers of a device by exchange bias [119]. This is the design of the device known as the *spin-valve*.

In a spin-valve device, one magnetic layer is expected to rotate freely while the other is pinned by an antiferromagnetic layer [120], effectively creating an exchange-biased synthetic antiferromagnet. The flow of current through the device then is modified by the application of a magnetic field. A schematic of the structure from Ref [119] can be seen below in Figure 4.4, where the red layer represents the magnetic free layer, the yellow layer is the non-magnetic spacer for antiferromagnetic coupling, the blue layer is the ferromagnetic pinned layer exchange-biased by the green antiferromagnetic layer.

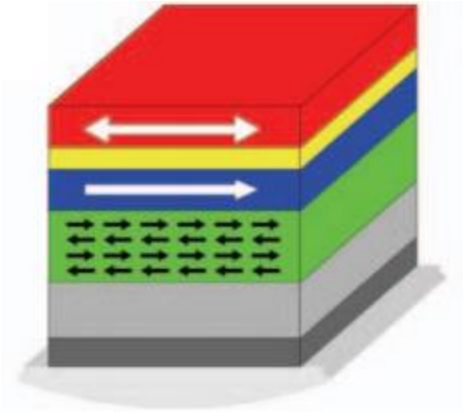

Figure 4.4 Basic GMR stack consisting of a pinned ferromagnetic layer locked by exchange bias (blue) and a ferromagnetic free layer (red).

4.1.2 Free Energy in the Exchange Biased System

This section will describe the free energy and magnetization dynamics in a real exchange biased system, especially as applied to the study of ferromagnetic resonance. We will refer to Figure 4.5 (adapted from Ref [24]) throughout the discussion, which is generalized from Ref [24].

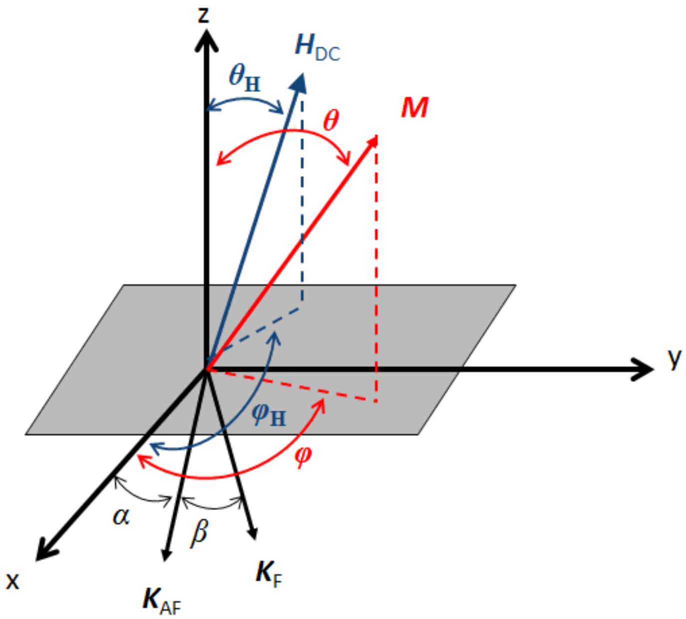

Figure 4.5 Spherical coordinate system used to describe orientations of M, H_{dc}, K_F, K_{AF}, with respect to the positive x-direction, which will be defined as the measurement direction.

In order to define the free energy, one must take into account the Zeeman energy, uniaxial anisotropy, and exchange anisotropy [48]. Keeping notation consistent with Figure 4.5 and assuming there is no significant contribution from shape anisotropy, the energy per unit volume is

$$\begin{aligned} E = &-M_S t_F H_{dc} \sin\theta \cos(\varphi - \varphi_H) + \left(2\pi M_S^2 t_F - K_S\right)\cos^2\theta \\ &- K_U t_F \sin^2\theta \cos^2(\varphi - \beta - \alpha) - H_{eb} M_S t_F \sin\theta \cos(\varphi - \alpha) \end{aligned} \tag{4.2}$$

where M_S is the magnetization, t_F is the ferromagnetic layer thickness, H_{dc} is the applied field, H_{eb} is the exchange bias field, θ and φ are the polar and azimuthal angles of the magnetization, θ_H and φ_H are the polar and azimuthal angles of the field, and K_S and K_U are the surface and uniaxial anisotropy coefficients. The angle α is the measurement angle, accounting for discrepancies in sample orientation during measurements. This can be adjusted for measurement offset after the fact. From here, α is set to zero.

It is often taken for granted that the uniaxial and unidirectional anisotropies lie along the same axis. It has been shown, however, that there is often a misalignment between these two anisotropies [24, 121-123]; they may be *noncollinear*. The angle β represents the misalignment angle.

Term by term, Eq 4.2 is the contributions from the Zeeman energy, shape and perpendicular anisotropies, in-plane uniaxial anisotropy, and interfacial exchange anisotropy [24]. From saturation, M_S will lie along the direction of H_{dc}, and therefore θ and θ_H are equal. Since the measurements are performed in the plane of the sample, $\theta = \theta_H = \frac{\pi}{2}$. This implies also that $\varphi = \varphi_H$ and that these angles represent the full magnetization and field vectors, respectively, rather than representing projections of the vectors. Applying these conditions, the free energy is found to be

$$E = -M_S t_F H_{dc} - K_U t_F \cos^2\left(\varphi_H - \beta\right) - H_{eb} M_S t_F \cos\varphi_H \tag{4.3}$$

4.2 Critical Curves in Exchange Biased Samples

It is known that H_{eb} as determined by through static and dynamic methods, such as the MHL and FMR respectively, in general, will give different values [124]. This is due to the fact that ferromagnetic resonance is a perturbative method which moves the magnetization only a small amount during the measurement, rather than irreversibly reversing the magnetization as in the MHL. Therefore, different magnetization processes are involved [125]. An interesting situation occurs by employing the Tunnel Diode Oscillator (TDO) method. This is a quasi-static method which does perturb the magnetization, but is also a magnetization reversal measurement. In the following sections, we report on the evaluation of H_{eb} as a function of t_{AF} through the critical curve constructed by the TDO method. We also compare static and dynamic evaluations of H_{eb} to the quasi-static evaluation.

4.2.1 Sample Description and Initial Measurements

Our samples were prepared at Universidade Federal de Santa Maria in Brazil by Dr. Paula Kern in the labs of Dr. Marcos Carara. This is a series of bilayer samples of $Ni_{81}Fe_{19}$(50 nm)/$Fe_{50}Mn_{50}$(t) prepared on Si (100) substrate through magnetron sputtering in a magnetic field of approximately 1 kOe. FeMn is commonly applied for domain stabilization and has been studied for a long time [96, 102]. NiFe has minimum anisotropy and magnetostriction, and therefore is a convenient magnetic material [93].

The thickness of the antiferromagnetic layer is varied across the five samples studied such that 3 nm $\leq t_{\mathrm{AF}} \leq$ 15 nm. The samples are named according to the thickness of the antiferromagnetic layer. The naming convention is P“t_{AF}(nm)”. For example, the sample t_{AF} = 3 nm is named P03, and sample t_{AF} = 15 nm is named P15. As is a common first step in exchange bias evaluation, the MHL was measured as a function of angle.

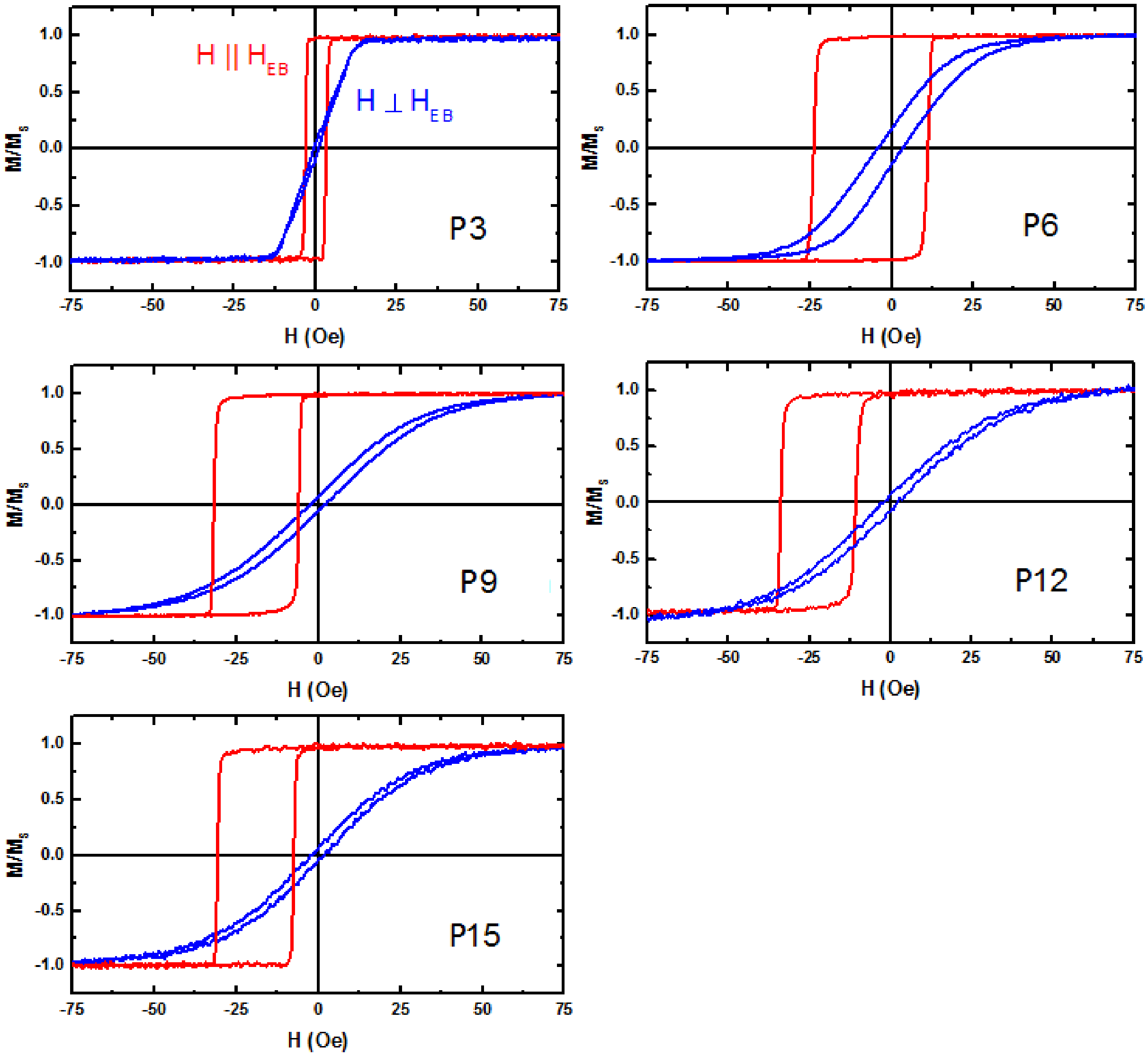

Figure 4.6 MHL as measured perpendicular (in-plane) to the exchange bias (blue) and parallel to the exchange bias (red) for all samples.

It is obvious that sample t_{AF} = 3nm shows no displacement of the MHL, even though an antiferromagnetic material is coupled to a ferromagnetic under the conditions outlined previously. This, however, is not surprising, as the onset of exchange bias in FeMn bilayer systems occurs around t_{AF} = 5 nm [24, 95, 105]. The variation in the exchange bias field, H_{eb}, with angle is seen below in Figure 4.7 and is shown along with the variation in coercivity. The coercivity is obtained by taking the absolute value half-difference of the coercive fields of the

MHL $\frac{|H_{C,L}-H_{C,R}|}{2}$, while the exchange bias field, H_{eb}, is evaluated through $\frac{H_{C,L}+H_{C,R}}{2}$.

Following this formula, no exchange bias was observed in sample P03, as expected.

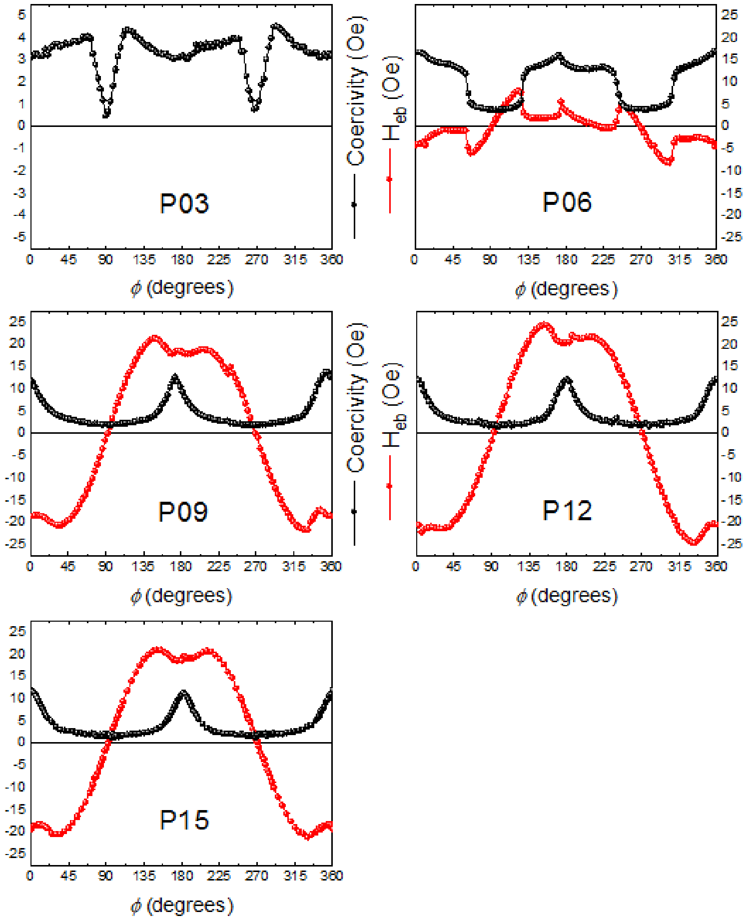

Figure 4.7 Variation of coercivity (black) and exchange bias (red) as a function of angle

The disturbances in the otherwise sinusoidal variation of H_{eb} vs φ become less extreme as the antiferromagnetic layer is increased. The imperfect sinusoidal behavior as well as the angular variation of coercivity is consistent with the findings of Ambrose *et al.*in Ref [94] and Xi *et al.* in Ref [102]. Figure 3 from Ref [94] and Figure 6 from Ref [102] are shown below in Figure 4.8 for comparison. In our samples, as antiferromagnetic layer thickness is increased, the graphs take on similar shape to Figure 4.8 *left* (a) and (b). In the figure above, 90° is defined by the orientation which shows zero exchange bias.

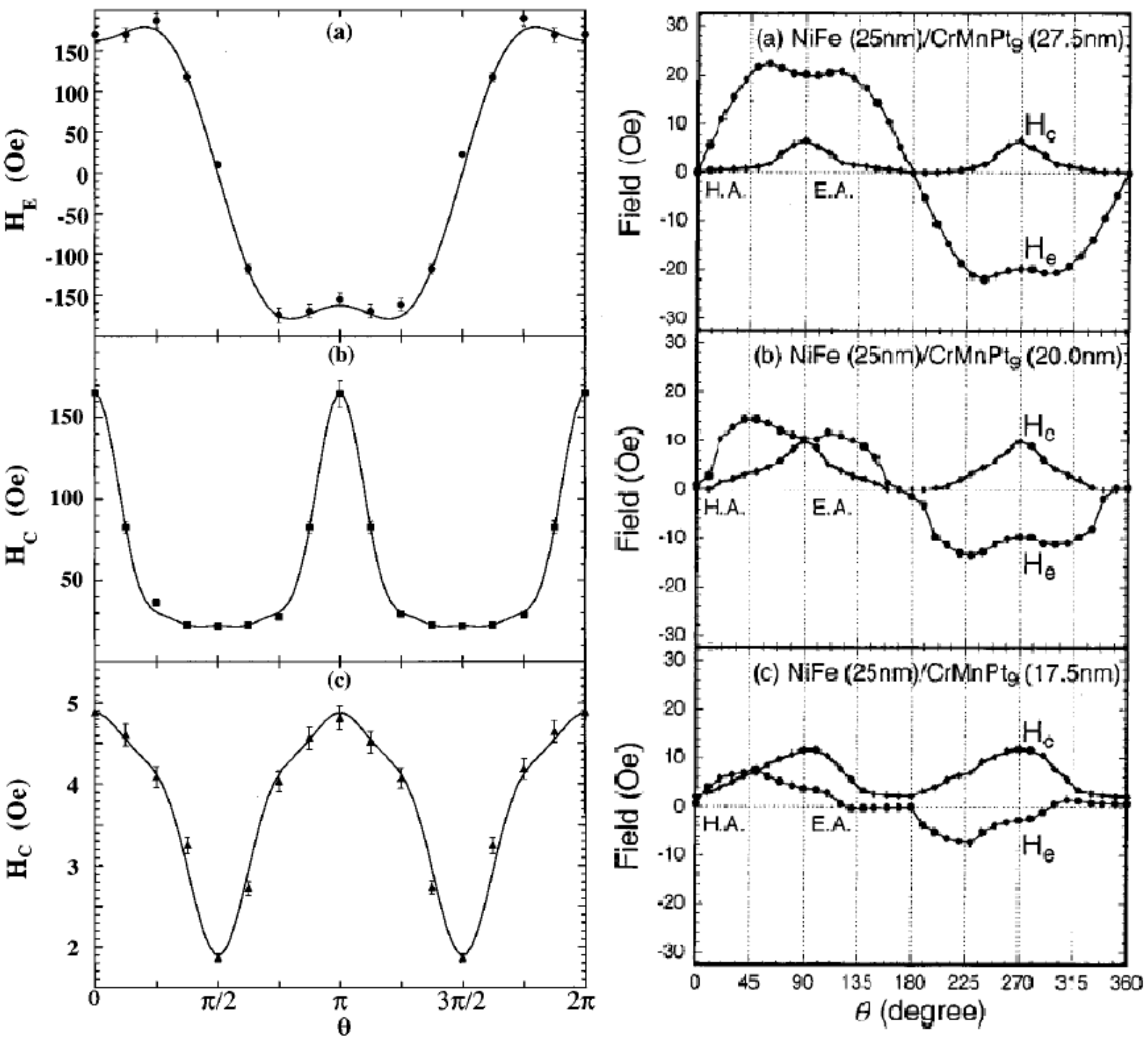

Figure 4.8 *left*: (Ambrose, 1997) Angular dependence of (a) exchange bias and (b) coercivity for NiFe(30 nm)/CoO(10 nm) system, and (c) coercivity for a single layer of NiFe. *right*: (Xi, 2000) Coercivity and H_{eb} for NiFe(25 nm)/CrMnPt$_9$(t), with t decreasing from (a) to (c).

Further, cavity FMR with angular variation was measured at 9.8 GHz for all samples. Figure 4.9 shows selected FMR curves for sample P09. The resonance field is defined as the x-value of the inflection point of the Lorentzian derivative. The y-axis is the derivative of absorption reported here in arbitrary units. The hard axis is defined as $\varphi = 90^{\circ}$.

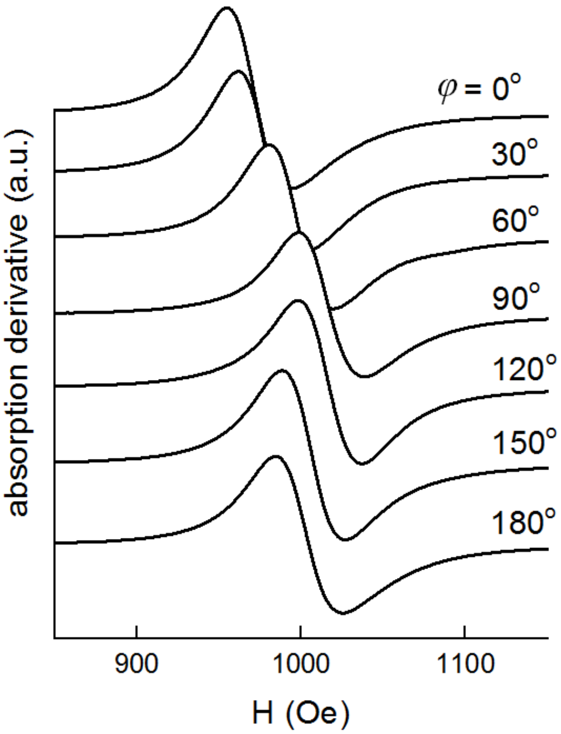

Figure 4.9 X-band FMR for sample P09.

After plotting the absorption derivatives, the resonance field H_r or H_{Res} can be determined by picking the inflection point. Plotting these as a function of angle in all samples, we find the angular variation of X-band FMR as shown in Figure 4.10. We now revisit Ref [24] for detailed analysis of these graphs. The resonance condition is [126]

$$\left(\frac{\omega}{\gamma}\right)^2 = \left[H_r + 4\pi M_{eff} + H_K \cos^2(\varphi_H - \beta) + H_{eb}\cos\varphi_H\right] \times \left[H_r + H_K \cos 2(\varphi_H - \beta) + H_{eb}\cos\varphi_H\right] \tag{4.4}$$

H_r and H_K are the resonance field and uniaxial anisotropy of the ferromagnet, ω is the angular FMR frequency, and γ is the gyromagnetic ratio. The quantity $4\pi M_{eff}$ is the effective demagnetization field and is equivalent to $4\pi M_S - 2K_S / M_S t_F$. As the surface anisotropy K_S can be large for thin films (small t_F) [127], we may assume that $H_r \ll 4\pi M_{eff}$. Additionally, $H_{eb}, H_K << H_r$, and the equation can be solved for H_r to find

$$H_r \approx \left(\frac{\omega}{\gamma}\right)^2 \frac{1}{4\pi M_{eff}} - H_{eb}\cos\varphi_H - H_K \cos 2\left(\varphi_H - \beta\right) \tag{4.5}$$

Note that the first term in this equation is independent of angle and therefore does not contribute to the anisotropy [128, 129], and the equation above is used to fit data in Figure 4.10. From the fitting, we may extract the values of H_{eb} and β.

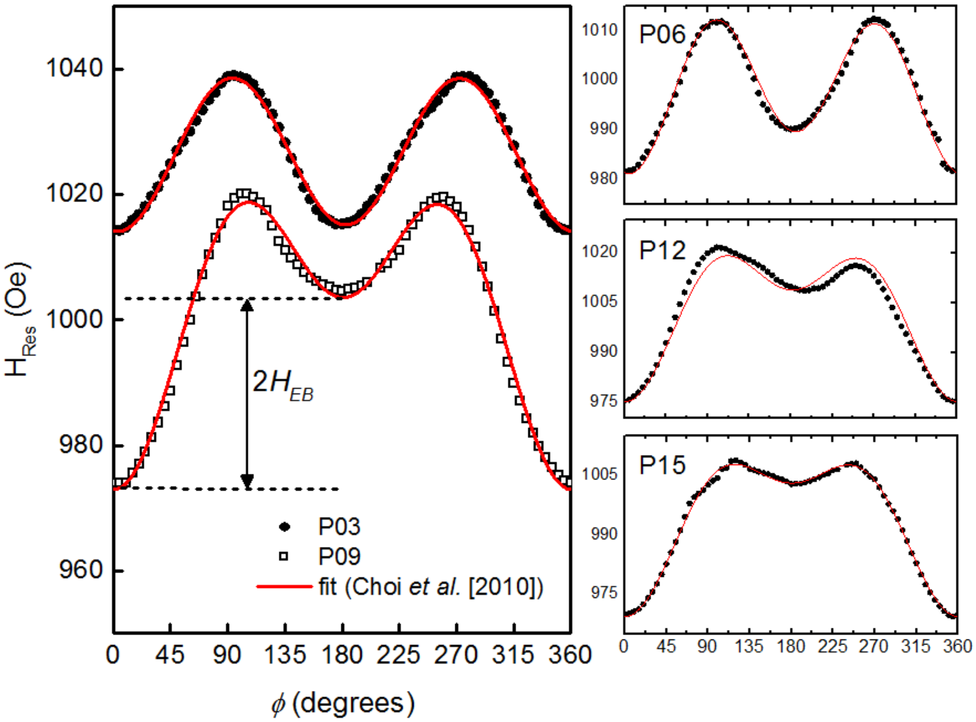

Figure 4.10 Angular variation of x-band FMR for all samples. The red line is the fit indicated in Eq 4.5 above.

H_{eb} can also be very simply extracted from this type of data, by taking half of the difference in resonance fields at 0° and 180°. As mentioned previously, there is often a discrepancy between exchange bias evaluated through different techniques. As we have calculated the value of H_{eb} through both methods, we can compare and find a difference as high as 22.8%. The comparison is shown below in Table 4.1, along with the angle of misalignment β, as determined only from the above fitting.

Sample	$H_{eb,\ X\text{-band FMR}}$	$H_{eb,\ MHL}$	β
P03	0	0	--
P06	4.26	4.65	5.26±0.37
P09	15.4	18.9	0.65±0.4
P12	16.9	21.9	1.25±0.99
P15	16.9	19.4	0.30±0.36

Table 4.1 Comparison of H_{eb} as evaluated through the MHL and X-band FMR spectra, with β included

This analysis indicates that sample P06 has the largest β while the smallest is found in sample P15. Note that P06 is the first sample in which exchange bias has appeared. The angle of misalignment may be explained more easily by referencing Figure 4.11, adapted from Ref [122]. The antiferromagnetic material (AFM) and ferromagnetic (FM) are shown, and emphasis is put on the imperfection of the interface, causing spin frustration when cooled below the Néel temperature T_N. Simulations by the authors successfully modelled the noncollinearity of the anisotropies in the exchange-biased system by applying random surface imperfections [122]. The assumption of existence of imperfections is reasonable, due to factors such as lattice mismatch, grain boundaries, surface roughness, etc. [24].

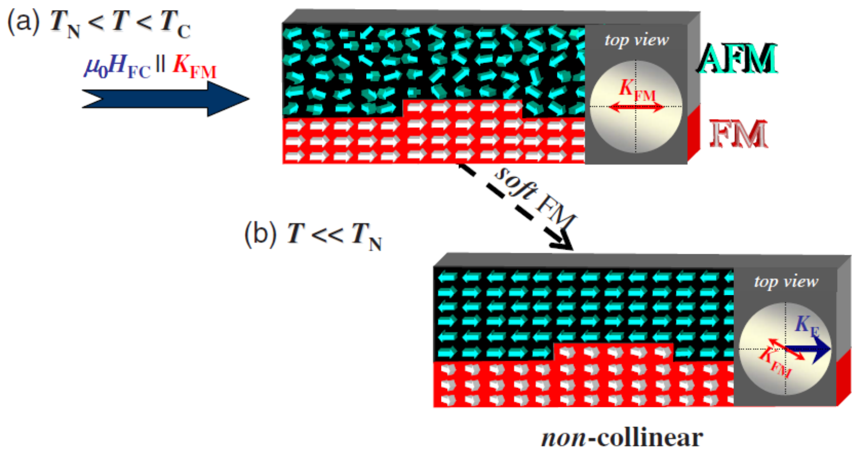

Figure 4.11 Model of the ferromagnetic (FM)/antiferromagnetic (AFM) interface (a) above the Néel temperature T_N of the antiferromagnet, and (b) below T_N (Jiménez, 2009)

We also relate the FMR measurements to the hysteretic measurements of exchange bias presented in Figure 4.7. The most symmetric case is seen in sample P15, the sample which is indicated in Table 4.1 to have the smallest β, while the most obvious symmetry breaking occurs in P06, indicated by FMR to have the largest β. The occurrence of high misalignment at the onset of exchange bias which decreases with increasing t_{AF} indicates that smaller antiferromagnetic anisotropies affect the alignment with the ferromagnetic anisotropy axis.

4.2.2 Critical Switching Curves

These samples were also studied through susceptibility (χ) measurements using the Tunnel Diode Oscillator (TDO), similar to the synthetic antiferromagnet sample of the last chapter. The critical curve (CC) for a perfect Stoner-Wohlfarth (SW) particle influenced by exchange bias should be displaced from the origin by an amount equal to H_{eb} and in the direction of H_{eb} along the exchange anisotropy axis.

The TDO circuit was exactly the same as used in the previous chapter. In this experiment, rather than using a double Helmholtz coil, an electromagnet on a rotation stage with goniometer was used to supply the magnetic field. The field step and angle step were 3 Oe and 3°, respectively. The field sweep was approximately ±80 Oe, as this is above the saturation point for all samples (see Figure 4.6). An example of the measurement of χ for sample P12 is shown in Figure 4.12 compared to the MHL for the dc field along 0°. As before, 0° is defined as the measurement perpendicular to the symmetric loop (90°).

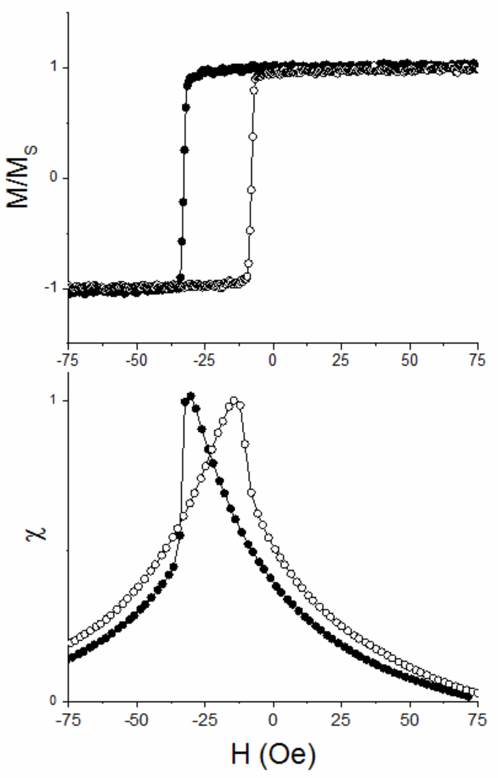

Figure 4.12 Normalized MHL (top) and susceptibility (bottom) along 0° for sample P12 for fields increasing (white circles) and fields decreasing (dark circles).

The descending branch of the MHL and corresponding susceptibility curve are shown with black circles while the ascending curves are white circles. A single peak is observed in the susceptibility signal, and it is this curve which is used to plot the CC point. The asymmetry across zero is a clear indicator of exchange bias, and the susceptibility hysteresis closely matches that of the MHL. Therefore, the CC is a useful characterization tool for determining H_{eb}.

An example of CC construction is shown below in Figure 4.13 for sample P03. As expected, the CC for this sample is symmetric, due to the fact that no exchange bias is present to shift the curve. Selected scans are shown as well to indicate the origin of points on the curve.

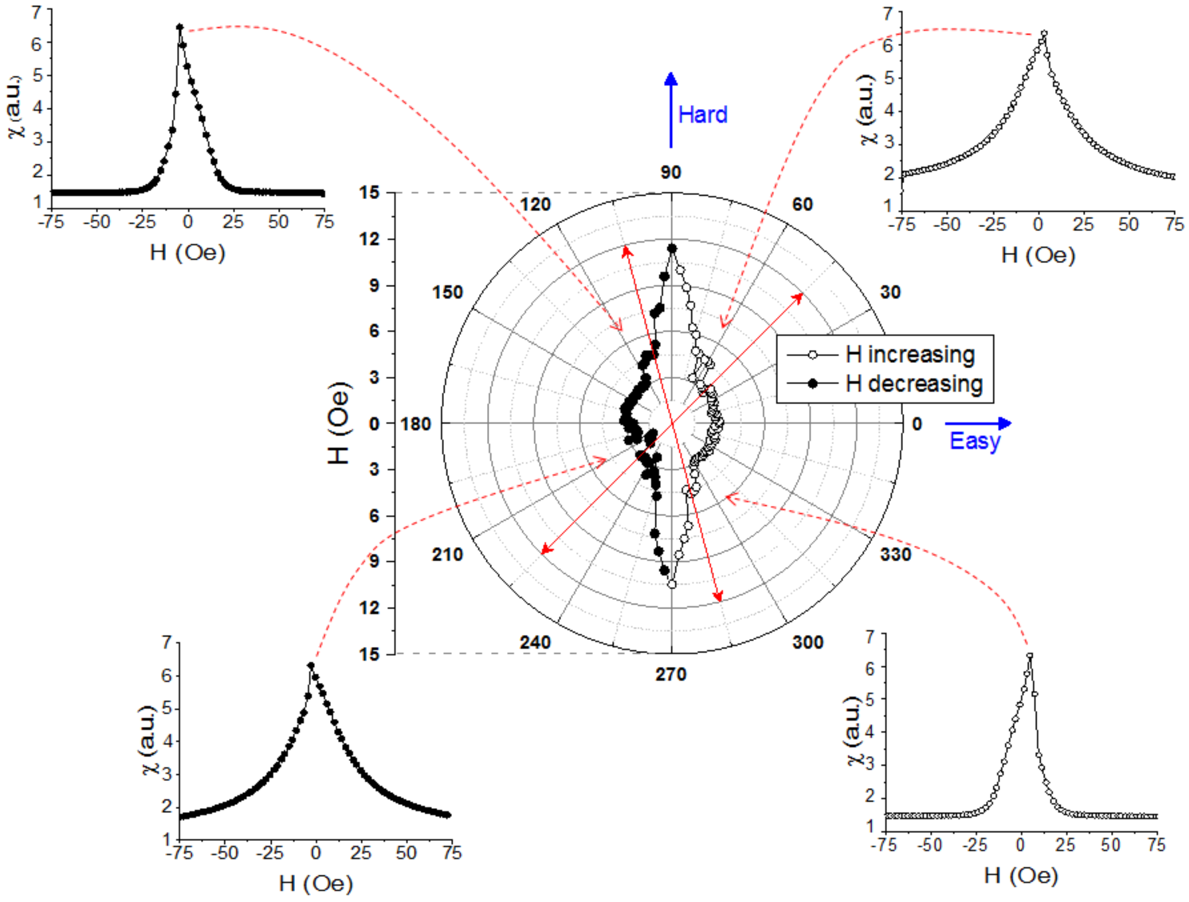

Figure 4.13 Critical curve of P03 (center) with selected susceptibility measurements shown

Contrasting with the CC of the SAF from the previous chapter, this sample shows a single curve, rather than an inner and outer envelope. This is exactly expected, as this sample is a single ferromagnetic layer rather than two coupled layers. The curve in Figure 4.13 is more representative of a typical ferromagnetic CC in a sample with uniaxial anisotropy [47]. Figure 4.14 gives a further look at the hard axis behavior of sample P03.

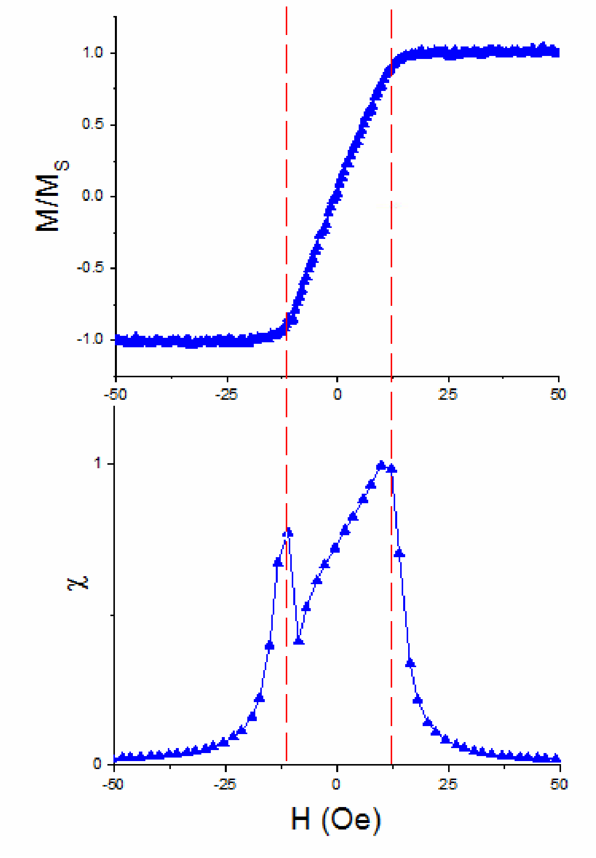

Figure 4.14 Hard axis characterization of P03 through descending MHL (top) and susceptibility (bottom)

The descending branch of the MHL for φ = 90° is seen in Figure 4.14 (top) with corresponding susceptibility curve below. Note the characteristic double peak, typical along the hard axis, in the susceptibility signal. As indicated in the figure, these symmetric peaks correspond to anisotropy field.

The other samples in this series are affected by exchange bias, and are therefore shifted by the exchange bias vector. Depending on the orientation of the dc field to the H_{eb} vector, the displacement may be either left or right.

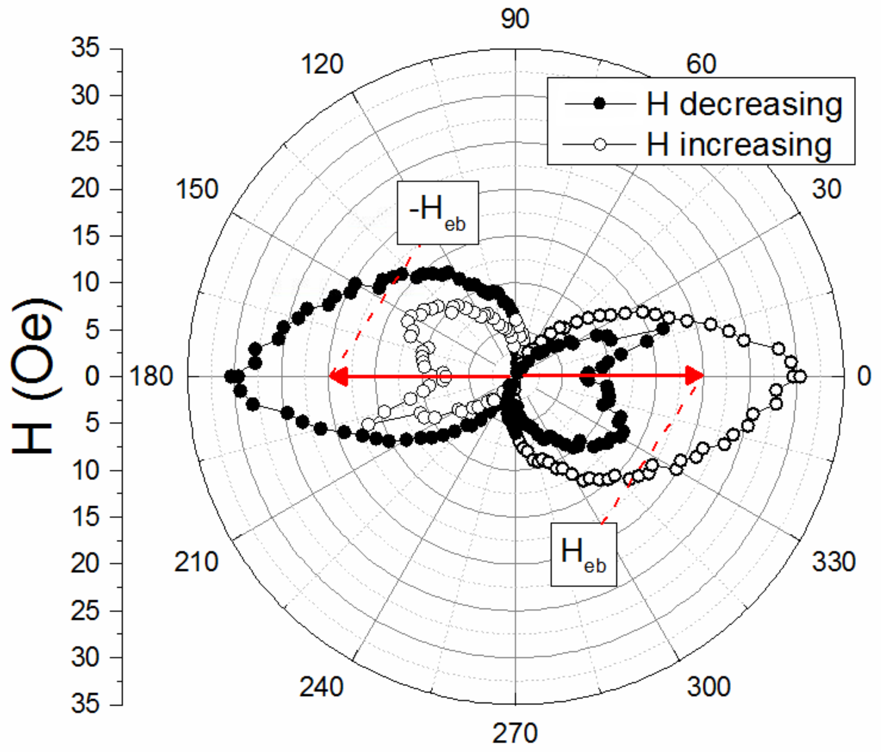

Figure 4.15 Critical curves for sample P09 showing displaced loop measured both parallel and antiparallel to the exchange bias vector

The left and right displacement for sample P09 can be seen in Figure 4.15. Note that, contrary to sample P03, the curve spirals back toward the origin, although the astroid shape is nearly retained approximately between the angles -30° and 30° (and 150° and 210°). In general, this is the region of interest [48], and from here the curves will only be displayed showing this region.

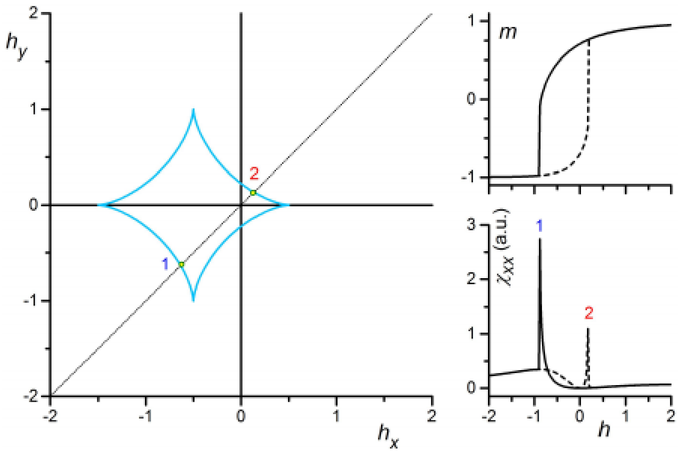

Figure 4.16 Theoretical astroid for the SW particle (left) shown with MHL (right – top) and susceptibility curve (right – bottom) at the selected angle.

As long as the susceptibility signal measured for increasing fields is different than that of decreasing fields, the peaks provide the correct critical curve, which, for the theoretical SW particle influenced by an exchange bias field collinear with the easy axis, is the displaced astroid of Figure 4.16. For the nearly reversible behaviors in the susceptibility signal, i.e. when increasing fields and decreasing fields show approximately the same peak, these false "tails" will appear for the displaced curve. Additionally, as the exchange bias is symmetric along its axis, it is only necessary to show one displaced curve.

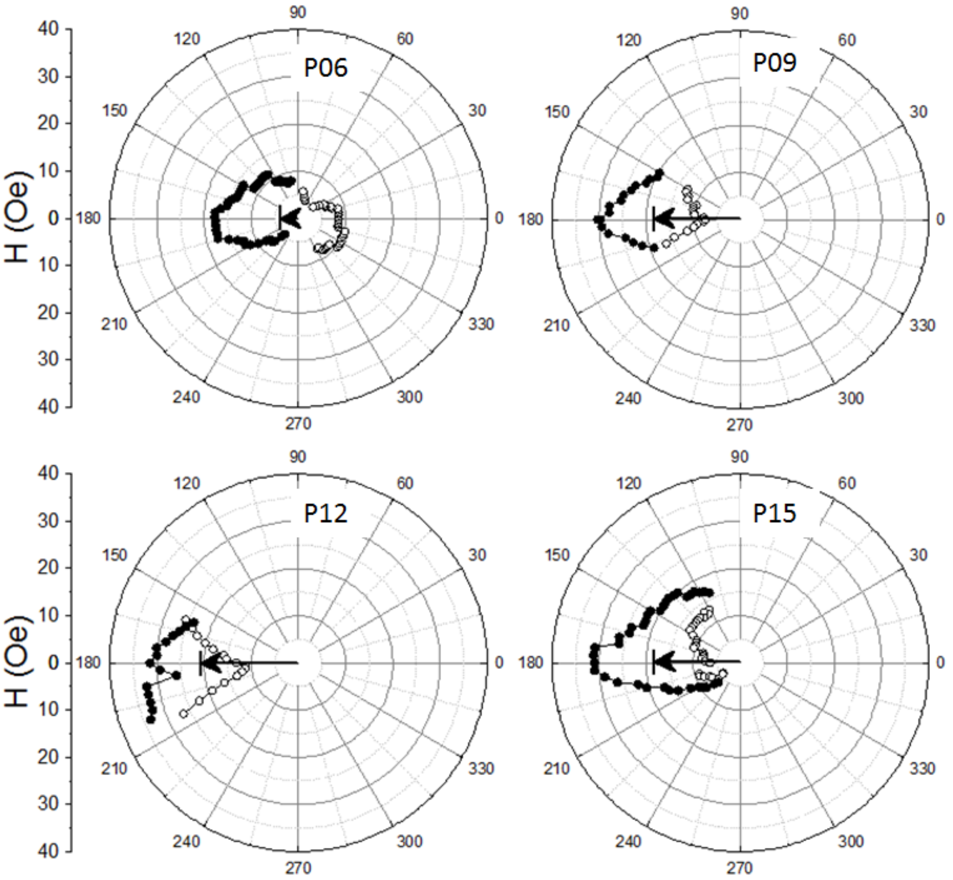

Figure 4.17 Critical curves for samples P06, P09, P12, and P15. Black vectors indicate the displacement

Figure 4.17 shows the four exchange-biased samples in this series. Black arrows indicate the displacement vector H_{eb}. As indicated in Figure 4.12, the susceptibility measurements for the CC are consistent with the MHL measurements, and therefore H_{eb} as evaluated through the quasi-static method is consistent with the static method. As observed in the above figure, the astroid shape is best retained in the samples which have thicker antiferromagnetic layers. In sample P06, which is at the onset of exchange bias, the CC is deformed from the theoretical SW model. This correlates with the fact that exchange bias as a function of angle for sample P06 (see Figure 4.7) showed the least symmetry of all samples. Additionally, the comparison in the angular variation of H_c and the CC are shown in Figure 4.18 for samples P06 and P09.

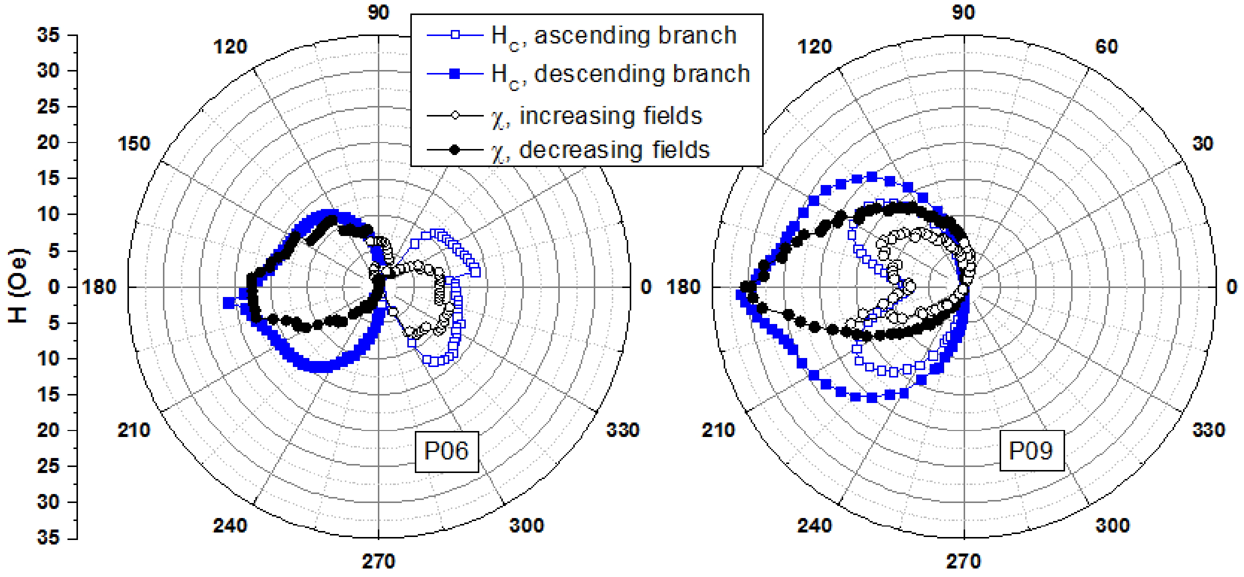

Figure 4.18 Comparison of H_c (blue) and CC (black) for samples P06 (left) and P09 (right)

Figure 4.19 below shows a summary of the data obtained in the last few subsections. For the first time, we have shown the evolution of the CC as t_{AF} is increased. The exchange bias in the quasi-static method of the TDO coincides with the static measurement of the MHL. Thus, the mechanism of magnetization reversal consistently gives a value for H_{eb} across the two different types of measurements.

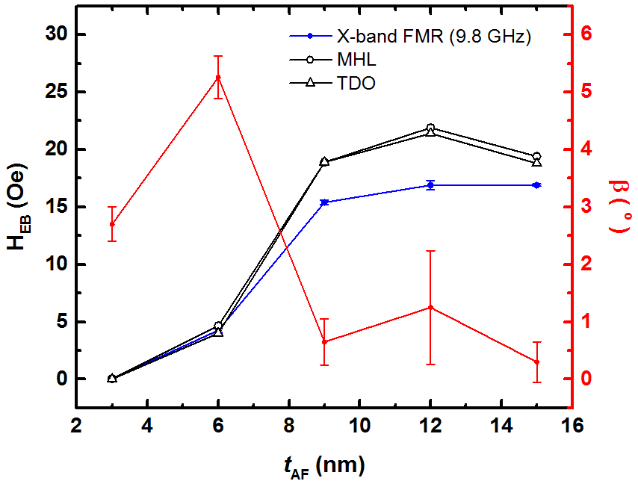

Figure 4.19 Comparison of H_{eb} obtained through the three different proposed methods of MHL (open circles), TDO (open triangles), and X-band FMR (blue circles), as well as the angle of misalignment β from the FMR fit.

4.2.3 Dynamic Critical Curves

The series was further studied through the use of the dynamic critical curve (dCC), which was introduced in Sec 3.2.3. The same protocol was applied here to our exchange-biased systems using the custom-built probe station. Measurements were made in Configurations 1 and 2 (see Figure 3.14 and Figure 3.19) [87] for all samples for FMR frequencies of 2, 3, 4, and 5 GHz.

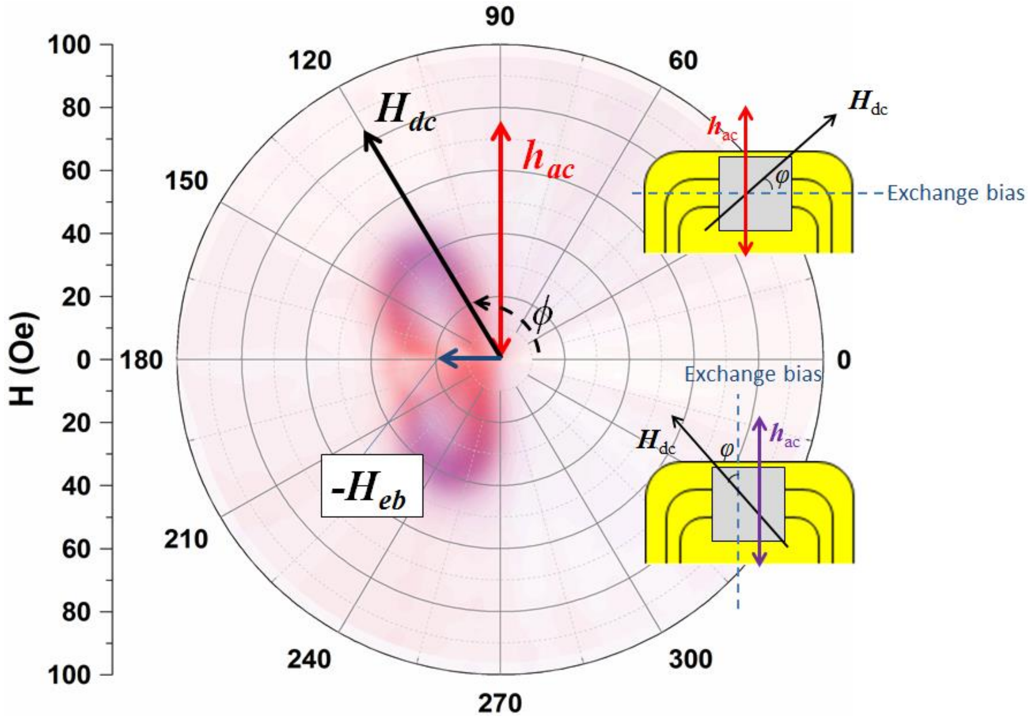

Figure 4.20 dCC for P09 at 2GHz showing negative displacement, applied dc field, and microwave magnetic field. *insets*: Configuration 1 (top) and Configuration 2 (bottom) with corresponding colors for microwave absorption. The exchange bias axis is represented by a blue dashed line in each Configuration.

An example of the dCC for P09 at 2 GHz is shown in Figure 4.20. The direction of $\boldsymbol{h}_{ac}$ is held constant in a direction approximately perpendicular to the exchange bias while an example of $\boldsymbol{H}_{\mathrm{dc}}$ is indicated with related angle θ as measured from the positive displacement axis. As before, the darkest colors correspond to highest absorption (or lowest transmission), with red representing FMR in Configuration 1 and purple representing Configuration 2.

As expected from the previous sections, the sample P03 did not have a displaced curve. The reason behind this was explained in Sec 4.2.1. Examples of the dCC for P03 can be seen in Figure 4.21.

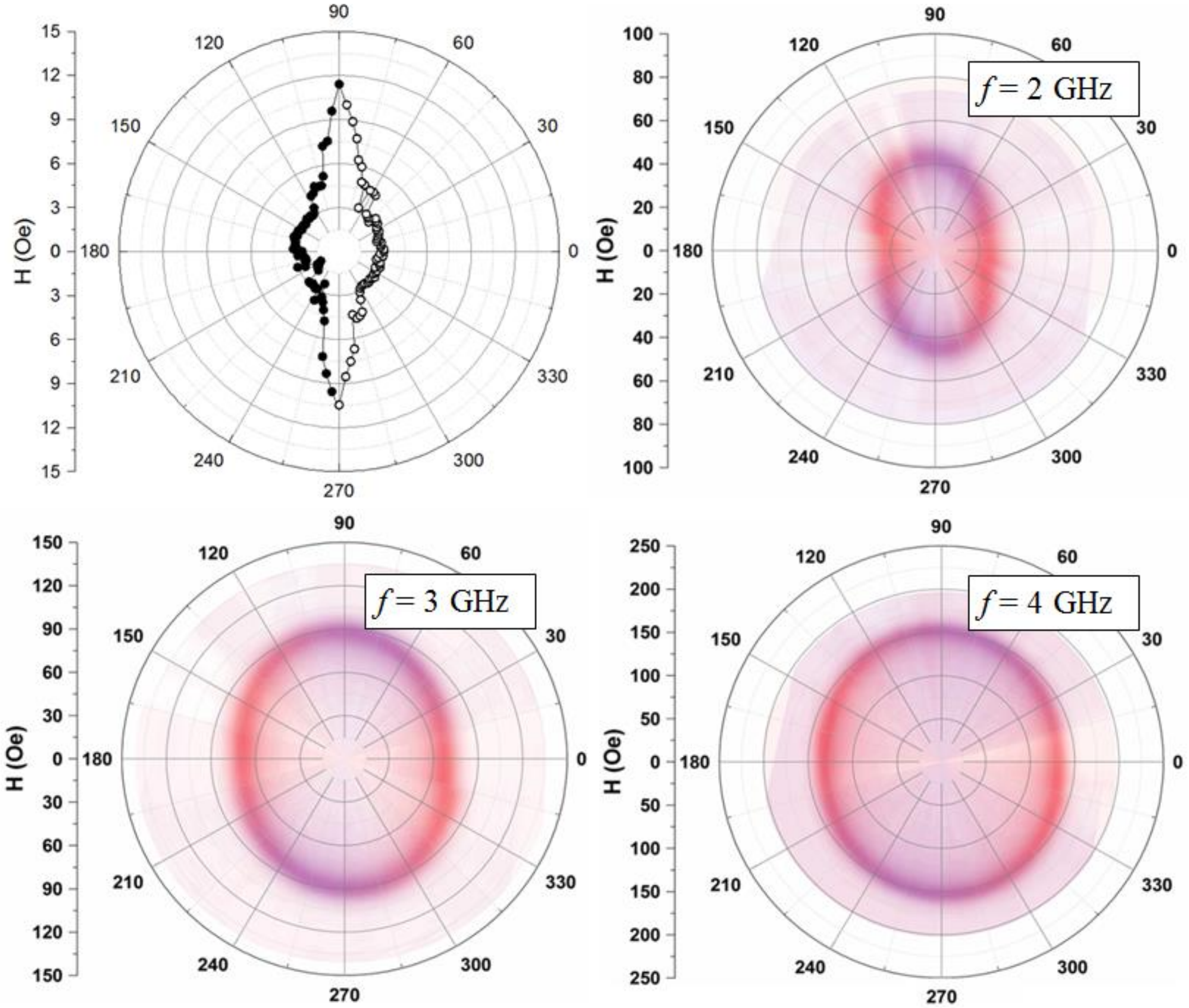

Figure 4.21 CC and dCCs for FMR frequencies 2, 3, and 4 GHz for P03

All other samples show a curve displaced by the exchange bias vector, as one would expect from the static and X-band measurements of previous sections. The value H_{eb} can be determined by measuring the displacement from the origin. To be precise, this value is calculated by selecting the point of maximum absorption along the exchange bias axis and applying the equation

$$H_{eb} = \frac{H_{r1} + H_{r2}}{2} \tag{4.6}$$

where H_{r1} and H_{r2} represent the two resonances observed in a spectrum, one corresponding to the positive magnetization state and the other to the negative magnetization state, which, in the case of exchange bias, are not symmetric. An example of these resonances is seen in Figure 4.22 for sample P15 measured along the exchange bias axis at 3 GHz.

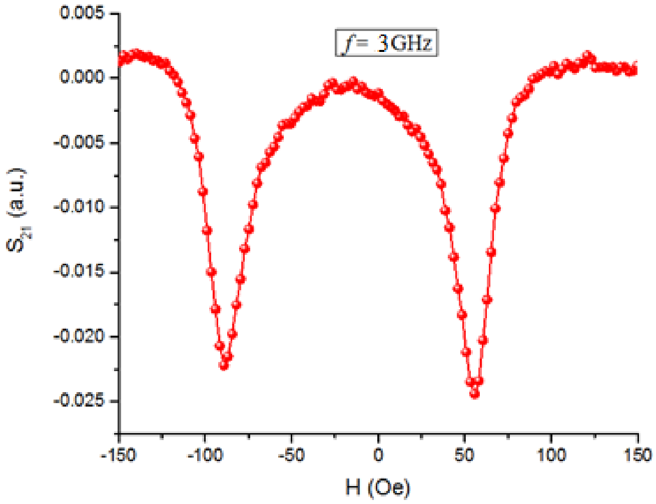

Figure 4.22 FMR spectrum for sample P15 for f = 3 GHz measured with H_{dc} ramped from positive to negative saturation along the exchange bias axis

From the figure, the two resonances are apparent, and the values can be plugged into Eq 4.6. Note that this evaluation is exactly equivalent to that seen in Figure 4.10, but in that case a difference is used rather than a sum because FMR is not evaluated in those measurements for a full spectra, but rather for positive fields only. For that reason, 0° and 180° must be treated using different signs. The exchange bias value was determined at all measured frequencies for all samples in this way.

We point out again that displacement may occur in either direction, depending on the orientation of the applied magnetic field with the exchange bias. Examples of displacement in each direction for P15 are shown below on the right side of Figure 4.23.

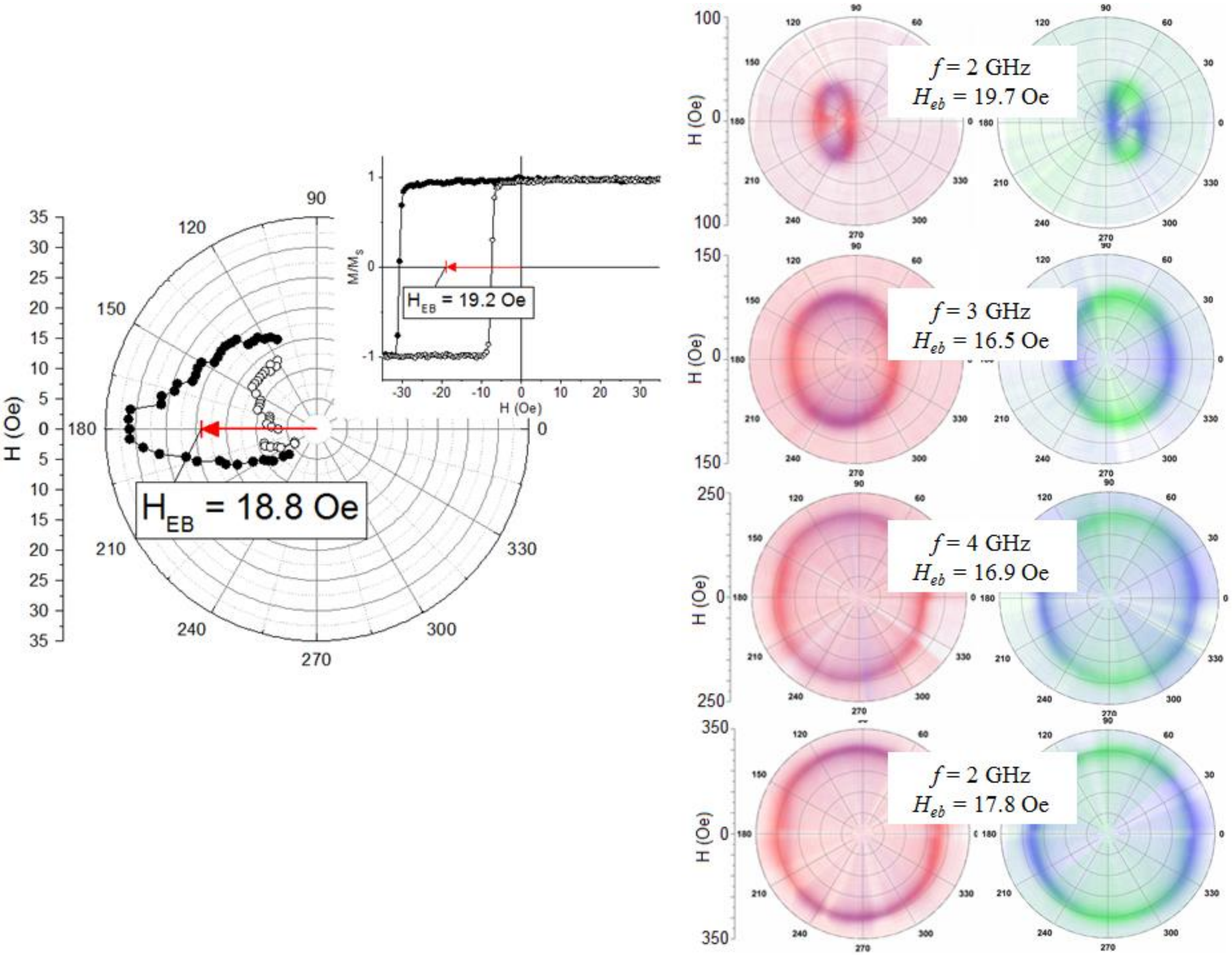

Figure 4.23 *left*: CC for sample P15. *inset*: MHL. *right*: dCC at all measured frequencies with both displacements shown. The value of measured exchange bias is indicated for each figure.

Figure 4.23 shows the comparison of the static CC and dCC, as well as the exchange bias evaluated through the static and dynamic measurements. As previously explained, the values should differ between the two different types of measurements. Another factor is the difficulty in aligning fields perfectly with the exchange bias axis. For the dCC, the angular increment was 5°, so it is reasonable to assume that, even though care was taken to set the measurement angle α equal to ϕ, perfect precision was nearly impossible.

To highlight the differences from one sample to another, Figure 4.24 compares the measurement of all samples at f = 3 GHz. As expected from the static measurements, little difference is observed between samples P09, P12, and P15.

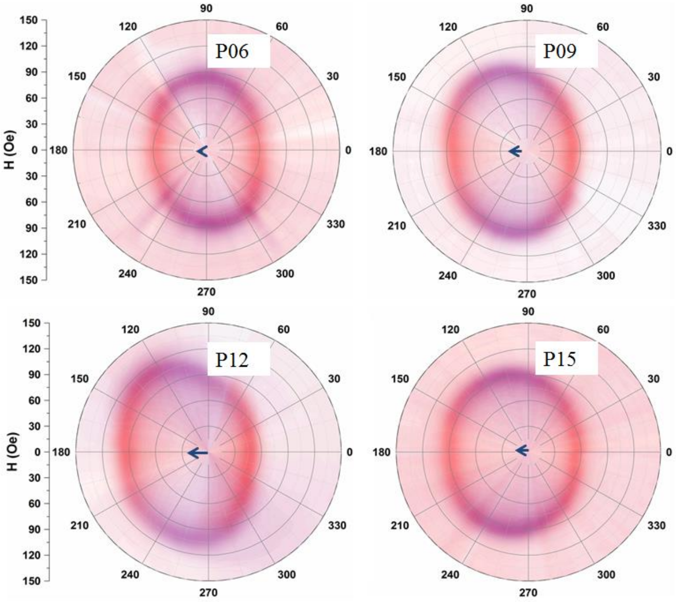

Figure 4.24 dCC at 3 GHz for all exchange-biased samples

To conclude this section, the value of H_{eb} as determined through all dCCs is compared below in Figure 4.25. The distinctions between the static and dynamic case is apparent, with TDO measurements again following the MHL.

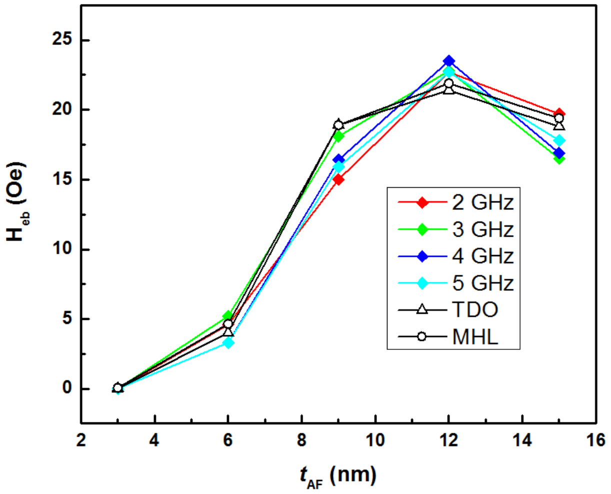

Figure 4.25 H_{eb} as determined for all exchange biased samples and FMR frequencies of the dCC, compared to the value determined by TDO and MHL

4.3 Summary

In this chapter, we have demonstrated the ability to apply our new characterization technique, the dCC, to the exchange bias system. While the dCC proved to be an effective mechanism in determining H_{eb}, we feel that the more interesting result is the evolution of the CC as antiferromagnetic layer thickness is changed.

We have also drawn a direct comparison between the evaluations of H_{eb} through three different methods. While comparisons between the MHL and FMR are known to give differing values, the quasi-static method of the TDO characterization had yet to be compared. From our analysis, it is clear that the TDO method gives values more closely resembling the static regime evaluation, with $H_{eb,\mathrm{TDO}}$ differing from $H_{eb,\mathrm{MHL}}$ by less than 3% in most cases and differing on average by 3.6% across the five samples. $H_{eb,\mathrm{TDO}}$ differs from $H_{eb,\mathrm{dCC}}$ by up to 11.4% and on average by 8.4%. Compared to X-band FMR, $H_{eb,\mathrm{TDO}}$ differs by 11.6% on average.

Chapter 5: Low Temperature Measurements of Exchange Bias in Multilayer Thin Films

This chapter introduces a phenomenon discovered more than half a century ago in rare earth (RE)-doped iron garnets. The same model, which has been adapted and applied to exchange bias, is applied here to multilayered ferromagnetic/antiferromagnetic spin-coupled samples.

5.1 Introduction to the Slow Relaxer Model

In 1962, Teale and Tweedale of Mullard Research labs reported on the microwave absorption of Yb-doped iron garnets, which had been shown to have a peak in resonance linewidth (ΔH) as a function of temperature [130]. Their work suggested that this peak could be explained by the relaxation of the Yb ion. Another observation was that, in measuring over a wide temperature range, the magnetocrystalline anisotropy as measured through the dynamic measurement of microwave absorption differed from that measured through an essentially static measurement over the same temperature range. The same phenomenon was observed for Er-doped FeO, Yb-doped YIG, EuIG, and YFeInO through the period of 1959 to 1965 [131-135]. An example of ΔH as a function of temperature is seen in Figure 5.1 [132].

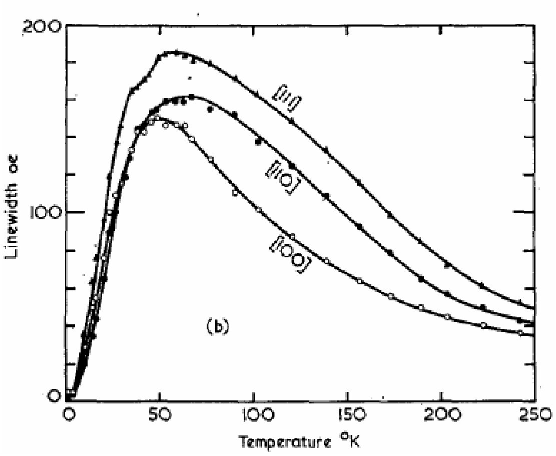

Figure 5.1 Example of ΔH variation with temperature for FeO doped with Yb and Er (Clarke 1963)

Teale and Tweedale explained this phenomenon on the basis of the population of the energy doublet of the rare-earth material. After a disturbance, the population of the energy doublet levels reaches thermal equilibrium at some time τ. At low temperatures, τ is long enough that during the precession of the magnetization in a magnetic field, the population is nearly constant. However, in a static experiment at the same low temperature, the magnetization rotates so slow that the thermal equilibrium is not disturbed but rather remains constant throughout the rotation. Therefore, the effective magnetocrystalline anisotropy is different depending on if it is measured through static or perturbative measurements.

A theory was derived by Teale and Tweedale [130] and Van Vleck and Orback [136] based on the earlier work of Clogston [137] and Galt [138] describing the slow relaxation process by rare-earth impurities. These works showed that ΔH takes the form

$$\Delta H \propto \frac{C}{T}\frac{\omega\tau}{1+\left(\omega\tau\right)^{2}} \tag{5.1}$$

where ω is the frequency, τ is the relaxation time, T is the temperature, and C is some constant. A shift, S_D, in the resonance field at some frequency ω due to the breaking of thermal equilibrium, is defined by

$$S_D \propto \frac{C}{2T} \frac{(\omega\tau)^2}{1+\left(\omega\tau\right)^2} \tag{5.2}$$

The quantity S_D was referred to by Clarke *et al.* [131] as the *dynamic shift* and was shown to be a function of the difference between the resonance field and the anisotropy field in the absence of relaxation effects. Therefore, the material must be measured in both static and dynamic environments in order to calculate S_D. Additionally, a form of relaxation time can be derived by dividing equation (5.2) by (5.1).

$$\frac{2\left|S_D\right|}{\Delta H} = \omega\tau \tag{5.3}$$

As shown in Ref [131], a fit to the experimental data of Eq 5.3 can be made using a relaxation behavior of the form

$$\tau = \tau_0 \tanh \frac{\delta}{kT} \tag{5.4}$$

which is taken from Orbach's spin-lattice relaxation time [139, 140]. The value δ is related to the doublet splitting.

Interestingly, similar phenomena have been observed in exchange biased systems. In the next section, a brief survey of these types of studies can be found.

5.1.1 History of Exchange Bias Measurements under the Slow Relaxer Model

In 1998, Lubitz *et al.* observed a peak in FMR ΔH for NiO/NiFe bilayers as temperature decreased [141]. In 2000, McMichael *et al.* observed similar behavior in CoO-biased bilayers as seen in Figure 5.2 [142]. These works were supported again by Lubitz *et al.* for NiFe bilayers with several different biasing layers [143].

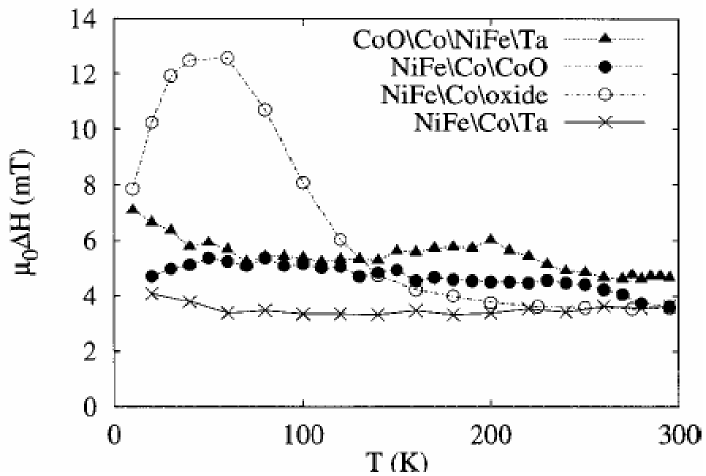

Figure 5.2 FMR ΔH as a function of temperature in CoO-biased films (McMichael 2000).

These groups identified antiferromagnetic grains as the slow relaxation mechanism in these FM/AFM systems. Two other group, Dubowik *et al.* [144] and Gloanec *et al.* [145, 146] have done similar experiments with bilayers, but these groups both came to the conclusion that paramagnetic ions present due to imperfections at the FM/AF boundaries are the slow relaxing mechanism rather than antiferromagnetic grains. This theory is more consistent with the original theory of relaxation in doped garnets. A fitting shown by Gloanec *et al.* [145], who also observed an FMR field shift, is consistent with the work of Clarke *et al.* [131]. These works were limited in that all experiments used bilayer samples and many focused only on a single FMR frequency. The study by Dubowik was also limited to temperatures above 78 K. A logical extension of these works would be a broadband investigation on a family of samples which includes static and dynamic measurements at liquid helium temperatures. This type of study was performed on multilayered samples and is presented in the following sections.

5.2 Sample Description

The multilayer samples were deposited on Si substrates with 50 nm of SiO_2 at room temperature using dc-triode sputtering with a base pressure of 3×10^{-9} Torr. Each sample has composition $[\mathrm{NiFe}\,(t\ \mathrm{nm})/\mathrm{IrMn}\,(20\ \mathrm{nm})]\times n(t)$, where t is the thickness of the ferromagnetic layer which is varied across layers and n is the number of repetitions. It should be noted that n is a function of ferromagnetic layer thickness and is adjusted to keep the full thickness constant across samples. Each sample has 10 nm Ti both as seed and capping layer. A field of 250 Oe was applied during deposition process to induce an anisotropy axis and to set the bias. The three samples are named S1, S2, and S3, and specific information can be seen in Table 5.1 [147]. A schematic of the samples is shown in Figure 5.3.

Sample	NiFe *t* (nm)	IrMn *t* (nm)	Repetition number *n*	Full thickness (nm)
S1	20	20	10	400
S2	60	20	5	400
S3	80	20	4	400

Table 5.1 Structural information for samples S1, S2, and S3.

5.3 Low Temperature Measurements

For all samples, the MHL was measured along the exchange bias axis using a Quantum Design Magnetic Properties Measurement System (MPMS) XL SQUID. SQUID magnetometry is an extremely sensitive device which monitors very small changes in magnetic flux and therefore can detect the magnetic properties of the sample. Using this system, the samples were measured in the temperature range 300 K to 2 K.

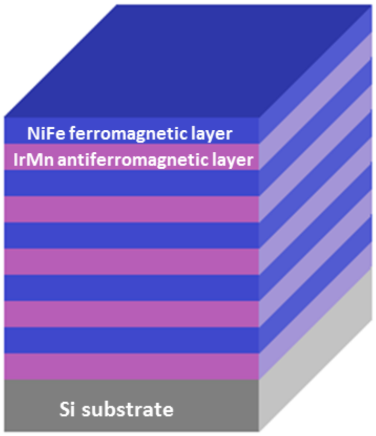

Figure 5.3 Example of NiFe/IrMn multilayer thin film structure with n = 5

In the high frequency regime, resonant absorption was measured using NanOsc CryoFMR integrated with the Quantum Design PPMS, discussed in Chapter 2. FMR was measured in the frequency range 3 to 16 GHz at temperatures 300 K to 2 K in 25 K increments. The sample was placed on the CPW with microwave magnetic field ($\boldsymbol{h}_{\mathrm{ac}}$) perpendicular to the exchange bias axis while the dc field of the PPMS ($\boldsymbol{H}_{\mathrm{dc}}$) was directed along the exchange bias (see Figure 5.4). $\boldsymbol{H}_{\mathrm{dc}}$ was ramped from 3000 Oe to -3000 Oe while probing the transmission coefficient.

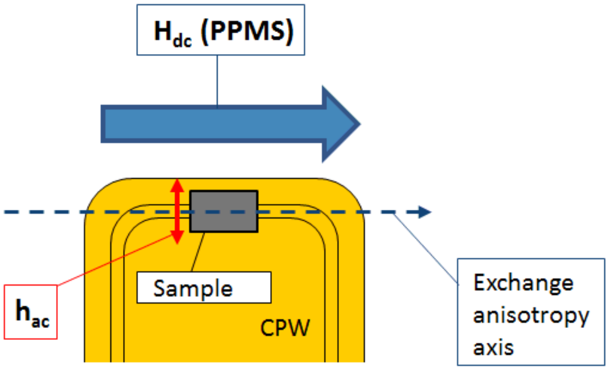

Figure 5.4 Sample on CPW with magnetic fields and anisotropy axis shown

5.4 Evaluation of Exchange Bias at Different Temperatures and Frequencies

It is worth noting that evaluating the exchange bias (H_{eb}) through the two different methods may yield values consistent with each other at temperatures close to 300 K, but as the temperature drops, the two values diverge largely. This will be clearer in the following sections.

5.4.1 Temperature Dependence of Exchange Bias in the Static Regime

H_{eb} is evaluated through the MHL recorded in through SQUID magnetometry. By the typical method, H_{eb} is determined by the shift in the MHL away from the origin. The exact value is determined by taking half of the sum of the coercive fields. Examples of the shifted hysteresis loop are seen in Figure 5.5.

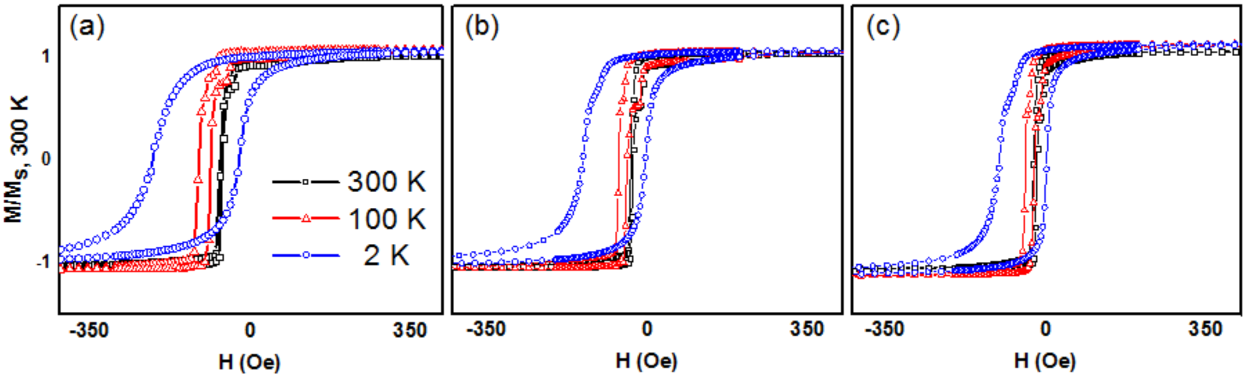

Figure 5.5 MHLs at selected temperatures for (a) S1, (b), S2, and (c) S3.

H_{eb} in the static regime is found to increase as the temperature in decreased. This is expected behavior. It has been shown that the shift in the MHL decreases with increasing temperature, and that the shift is dependent on the AF grain size. Additionally, the AF grain size is shown to be constant for a given film thickness [148]. As seen in Table 5.1, the AF film thickness is consistent across all our samples, and therefore, H_{eb} has the same type of temperature dependence in all samples. This temperature dependence is seen in Figure 5.6.

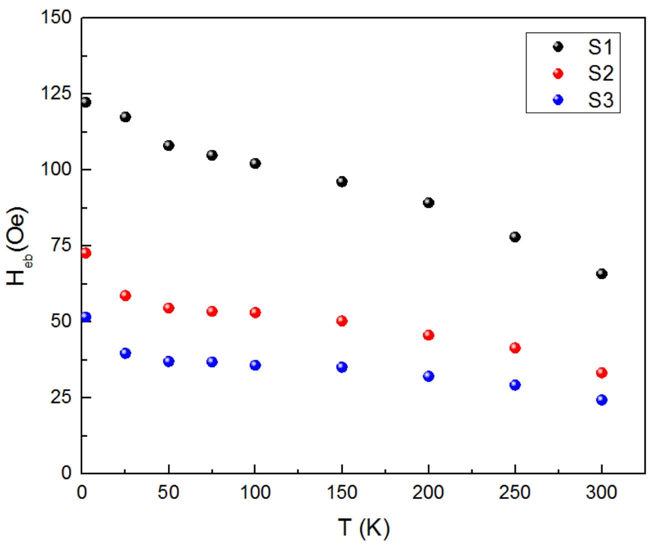

Figure 5.6 Temperature dependence of H_{eb} from the MHL

5.4.2 Temperature Dependence of Exchange Bias in the Dynamic Regime

From the dynamic measurements, H_{eb} can be evaluated at every measured FMR frequency by taking half of the sum of the resonance fields, H_r, for fields parallel to the exchange bias axis and antiparallel to the exchange bias axis. An example is shown in Figure 5.7 .

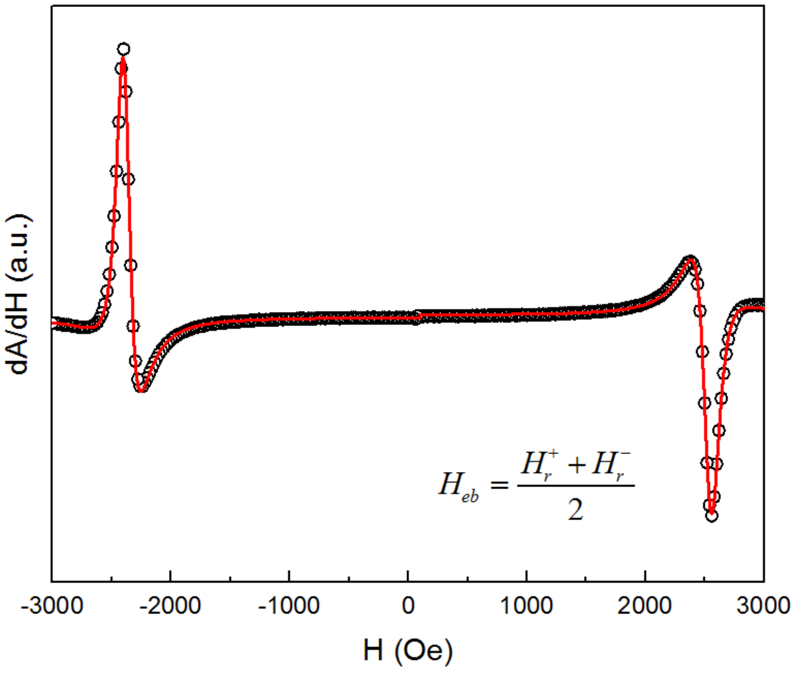

Figure 5.7 FMR spectra for sample S1 at 16 GHz and 300 K (black open circles) and fit using an asymmetric Lorentzian derivative (red solid line)

Two notable phenomena are seen in the analysis of the FMR data. The first is that the linewidth increases as temperature decreases and comes to a noticeable peak below 100 K before decreasing. This is a similar occurrence to that of the original slow relaxer experiments of the 1950’s and 60’s and has been observed by others in exchange bias [141-143]. The linewidth (Figure 5.8) appears to have the same form as Eq 5.1. This feature is a notable signature of the slow relaxer mechanism and is explained as an anisotropic exchange field between the ferromagnet and the impurities [136].

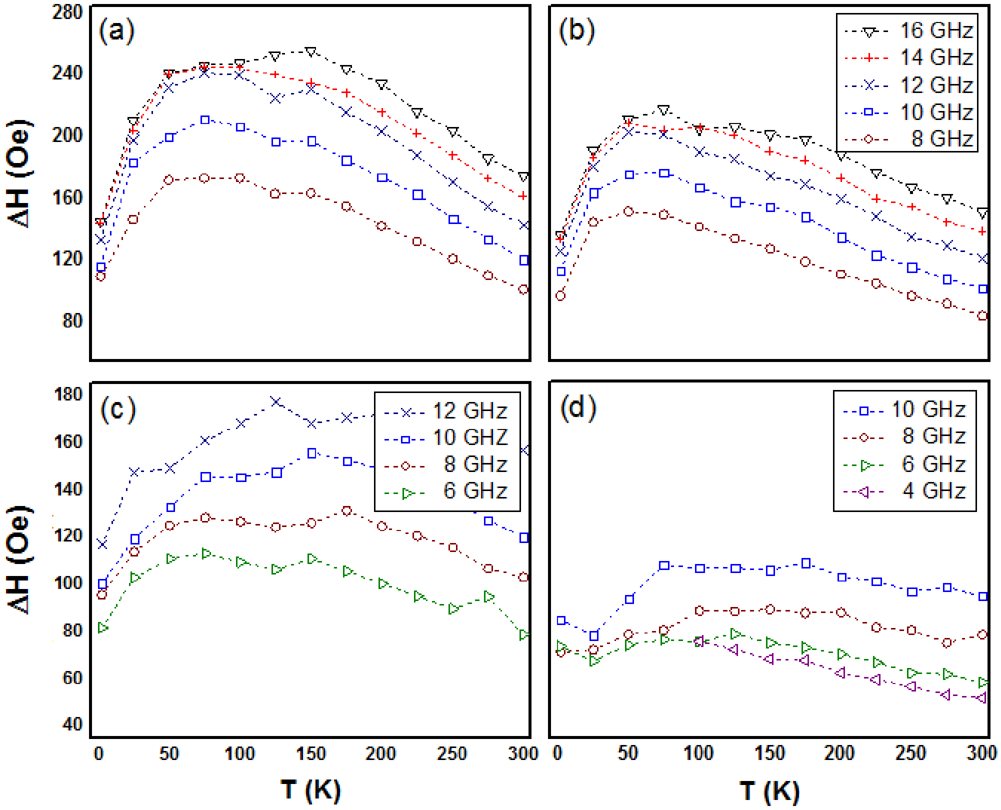

Figure 5.8 ΔH as a function of temperature for (a) S1 at 0°, (b) S1 at 180°, (c) S2 at 0°, and (d) S3 at 180°

The second is that H_{eb} *decreases* below 250 K as temperature is decreased. This leads to an obvious disagreement in the value of H_{eb} determined through the two different methods. This feature has also been observed in bilayers [145, 146] and is explained in much more detail in the following section.

5.4.3 Comparison and Discussion

The disagreement between the values of $H_{eb,\text{static}}$ and $H_{eb,\text{dynamic}}$ can be attributed to an anisotropic field shift in the FMR data, which accounts for the decreasing trend in the value of $H_{eb,\text{dynamic}}$. As seen in Figure 5.9 , the difference in H_r for positive field values ($\delta \mathrm{H}_\mathrm{R}^+$) for two different temperatures is not equal to the difference for negative field values ($\delta \mathrm{H}_\mathrm{R}^-$). As these two fields are critical for determination of H_{eb}, this accounts for an unexpected H_{eb} when comparing to the static determination. This shift can be explained by some AF grains forgetting the initial conditions after undergoing irreversible transitions [145]. This was applied to exchange bias [124, 149] after being predicted by Néel [34].

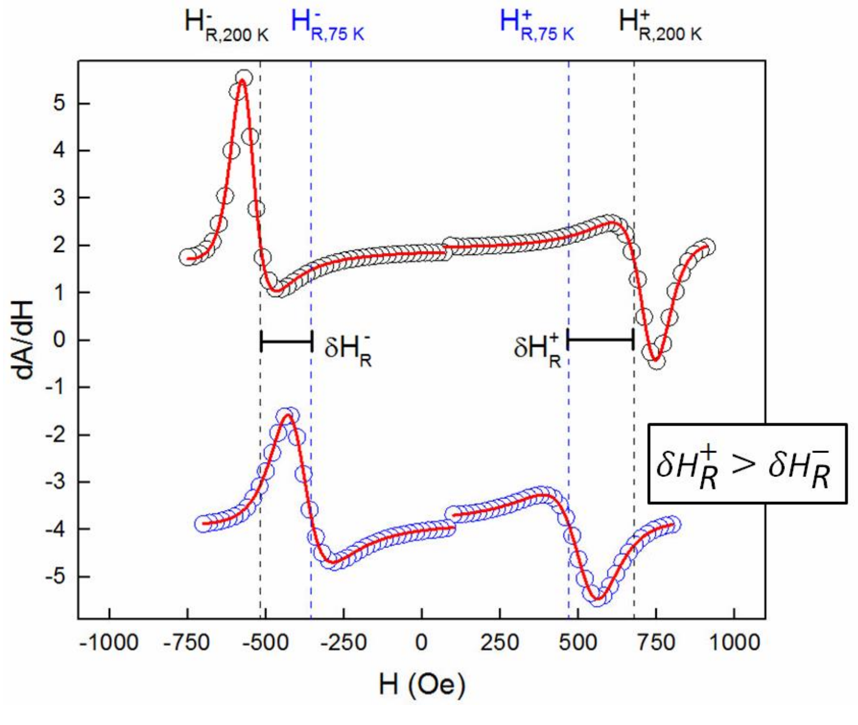

Figure 5.9 Anisotropic resonance field shift for S1 at 200 K compared to 75 K

We now define our dynamic shift S_D [recall Eq 5.2(5.2)] as

$$\left|S_D(\omega,T)\right|_E = \left|H_{eb}\left(0,T\right) - H_{eb}\left(\omega,T\right)\right| \tag{5.5}$$

where $H_{eb}(\omega,T)$ is the exchange bias from FMR and $H_{eb}(0,T)$ is from the MHL where the excitation frequency in zero. Figure 5.10 shows the comparison of H_{eb} through static and dynamic measurements for all samples. The dynamic shift as defined in Eq 5.5 is shown as well.

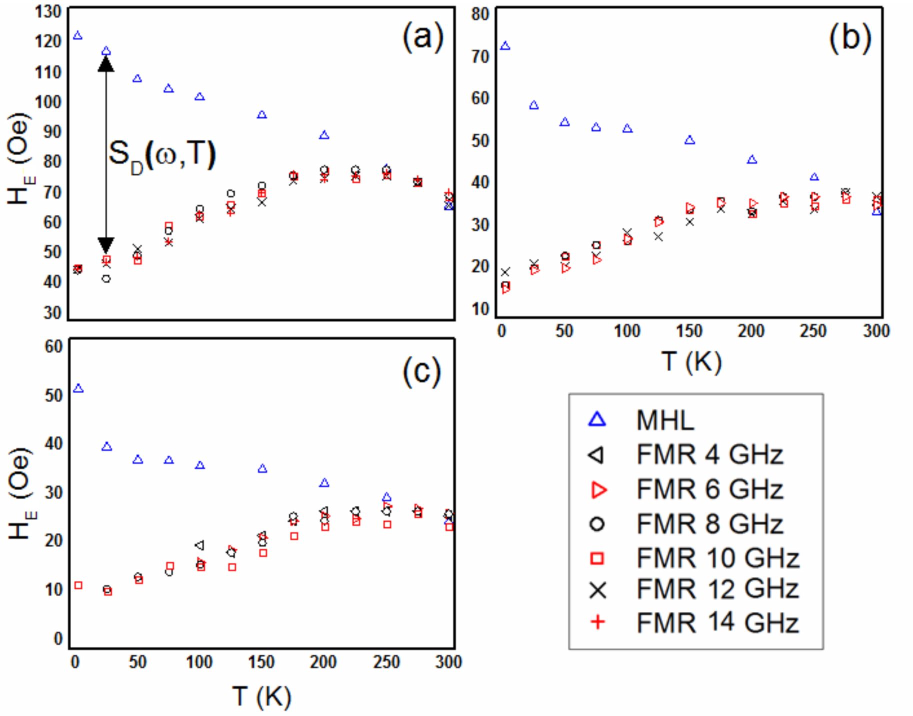

Figure 5.10 Exchange bias through the MHL (blue triangles) and FMR (black/red symbols) for (a) S1, (b) S2, and (c) S3 as a function of temperature. The difference between the two curves is the dynamic shift.

Now that S_D and ΔH are defined, we can follow Eqs 5.5 and 5.3 to find a relation between the ratio of S_D and ΔH and the relation time τ. This relationship is shown graphically in Figure 5.11.

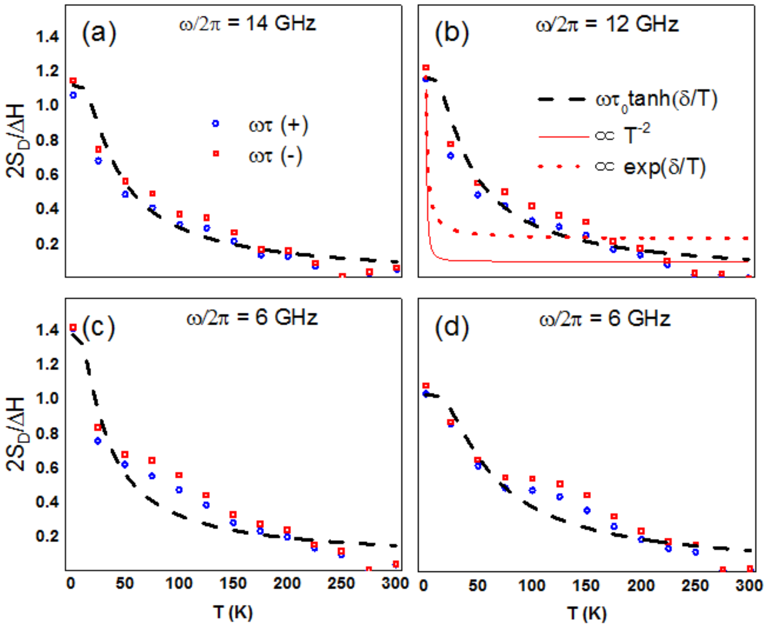

Figure 5.11 Temperature dependence of ωτ defined in Eq. (5.3) for (a) S1 at 14 GHz, (b) S1 at 12 GHz, (c) S2 at 6 GHz and (d) S3 at 6 GHz for positive (red squares) and negative (blue circles) FMR fields. Solid, dotted, and dashed lines refer to different fits.

The dashed black line in Figure 5.11 is a fit using Eq 5.4 and is taken from Orbach's derivation of spin-lattice relaxation time [139, 140] and is consistent with previous studies for bilayers [145, 146]. This fit corresponds to the theory that paramagnetic ions at the interface are the slow-relaxing mechanism. Figure 5.11(b) has examples of other fits which corresponds to relaxation behaviors predicted by others [141-144]. The dotted red line is a fitting of the form predicted by the Néel relaxation theory [34]. This would correspond to slow relaxation by antiferromagnetic grains, which was proposed by McMichael *et al*. and Lubitz *et al*. The solid red line is the relaxation behavior proposed by Dubowik *et al*., although this experiment was not performed for the full temperature range.

It is clear that the signatures of the slow relaxer model (Figure 5.8 and Figure 5.10) are most obviously present in sample S1. The subtle differences in the shape of the curves across the three samples in Figure 5.11 can be expected since $\omega\tau$ is dependent on ΔH, which becomes flatter as the number of layers is decreased. The fact that the fit is still imperfect may be attributed to difficulties in obtaining an accurate value for ΔH since the FMR spectra for these samples was somewhat asymmetric (see Figure 5.9 for example).

5.5 Summary

The work presented here gives support to one of the current theories of the slow relaxer mechanism, and is the first of its kind performed on multilayer samples. Additionally, it is the first study of this type using a family of samples for easy comparison of different properties. Another advantage of these experiments is the wide range of FMR frequencies probed, whereas others have been limited to a smaller number of frequencies, with many using only an X-band frequency between 9 and 10 GHz. This, combined with measurements done in the full range of temperatures from room temperature to below that of liquid helium, gives a more thorough study. The characteristics of the slow relaxer mechanism, namely, ΔH broadening and peak below 100 K, as well as an anisotropic shift in FMR spectra, are most apparent in the sample with most layer repetitions and therefore the highest number of surface boundaries [150].

Chapter 6: Conclusions

The exploration of magnetization dynamics is critical to device design and application. Due to restraints of different devices, the materials of interest are usually thin films, including multilayered thin films, in which magnetization changes occur in the film plane. For this reason, controlling two-dimensional switching and characterization of the magnetic properties in the film plane is crucial to future application as well as fundamental understanding.

In the first chapter, we presented the background necessary to proceed, leading up to the development of the Stoner-Wohlfarth model. In the following chapter, the technique of constructing the critical curve, the experimental compliment to the theoretical Stoner-Wohlfarth astroid, from susceptibility measurements in the sample plane was detailed. In general, the in-plane switching can fully be described by the critical curve, as the curve is a polar map of the fields at which irreversible magnetization reversal occurs. It can then be thought of as a switching map or fingerprint of the switching properties of the sample under study.

Using this concept, we characterized our first magnetically coupled system, the synthetic antiferromagnet (SAF), pointing out the unique shape of the critical curve. We then extended this to the regime of ferromagnetic resonance (FMR), introduced in Chapter 2. To construct a polar map of FMR fields under critical curve formalism required a new experimental setup to probe FMR fields in an angular-dependent fashion using a Vector Network Analyzer capable of measuring resonant absorption of electromagnetic energy by tracking transmission of the electromagnetic wave. Using this concept of the dynamic critical curve (dCC), it was discovered that at low enough frequency, the dCC moved completely inside of the critical curve, with no symmetric components on the outsides of the critical curve branches, which should normally occur in ferromagnetic systems. This implied that there is an energy for which resonant absorption only occurs in the state in which the magnetizations of the SAF layers are antiparallel.

Naturally, we wished to extend this study to a different type of system. We applied these concepts to a series of exchange-biased samples with differing thicknesses of the antiferromagnetic layer (t_{AF}). In the end, the dCC did not show any unexpected behaviors, while the critical curve clearly evolved as a function of t_{AF}.

The experimental works concluded with a low-temperature study of exchange-biased multilayers. The properties of these samples were explored in the static and dynamic regimes as before, but with different measurement protocols. These samples were not subject to angular-dependent studies, but rather temperature was used as the variable parameter. The vast divergences in the evaluations of exchange bias as a function of temperature were explained under the slow-relaxer model.

A major focus of this experimental work was on the development and improvement of the new probe station for measuring the dCC. This experimental setup was improved over the years first by using vibration isolators and secondly by relocating the entire setup to a new lab with a large optical table in order to improve the signal to noise ratio.

With the understanding that magnetization switching is critical to device performance, all efforts of characterizing the switching properties of magnetic nanostructures can be justified. This work has sought to explore, understand, and report the features of the critical curve and dCC for magnetically coupled thin film systems.

References

1. Bauer, M., et al., *Switching behavior of a Stoner particle beyond the relaxation time limit.* Physical Review B, 2000. **61**(5): p. 3410-3416.
2. Kaka, S. and S.E. Russek, *Precessional switching of submicrometer spin valves.* Applied Physics Letters, 2002. **80**(16): p. 2958-2960.
3. *Ferromagnetic Resonance* ed. S.V. Vonsovskii. 1966, London: Paragamon Press.
4. Slonczewski, J.C., *Theory of magnetic hysteresis in films and its applications to computers.* Research Memorandum R.M. 003.111.224, IBM Research Center Poughkeepsie, 1956.
5. Thiaville, A., *Extensions of the geometric solution of the two dimensional coherent magnetization rotation model.* Journal of Magnetism and Magnetic Materials, 1998. **182**(1-2): p. 5-18.
6. Stoner, E.C. and E.P. Wohlfarth, *A Mechanism of Magnetic Hysteresis in Heterogeneous Alloys.* Philosophical Transactions of the Royal Society of London. Series A, Mathematical and Physical Sciences, 1948. **240**(826): p. 599-642.
7. Radu, C., *Study of Magnetization Switching in Coupled Magnetic Nanostructured Systems*, in *Physics*. 2008, University of New Orleans.
8. Radu, C., et al., *Reversible susceptibility studies of magnetization switching in FeCoB synthetic antiferromagnets.* Journal of Applied Physics, 2007. **101**(9): p. 09D109.
9. Radu, C., et al., *Measurement of the critical curve of a synthetic antiferromagnet.* Applied Physics Letters, 2008. **93**(2): p. 022506.
10. Tebble, R.S. and D.J. Craik, *Magnetic Materials*. 1969: Wiley-Interscience.
11. Kittel, C., *Introduction to Solid State Physics*. 8 ed. 2005, New Jersey John Wiley & Sons.
12. Cullity, B.D. and C.D. Graham, *Introduction to Magnetic Materials*. 2008: Wiley-IEEE Press. 544.
13. Zhong, K., et al., *A novel spin modulation of work function for C adsorbed Cr/Fe(001) metal gate.* AIP Advances, 2012. **2**(4): p. 042134.
14. Ruderman, M.A. and C. Kittel, *Indirect Exchange Coupling of Nuclear Magnetic Moments by Conduction Electrons.* Physical Review, 1954. **96**(1): p. 99-102.
15. Mahan, G.D., *Condensed Matter in a Nutshell*. 2011, United Kingdom: Princeton University Press.
16. Kasuya, T., *A Theory of Metallic Ferro- and Antiferromagnetism on Zener's Model.* Progress of Theoretical Physics, 1956. **16**(1): p. 45-57.
17. Yosida, K., *Magnetic Properties of Cu-Mn Alloys.* Physical Review, 1957. **106**(5): p. 893-898.
18. Nolting, W.R., Anupuru *Quantum Theory of Magnetism*. 2009, Berlin: Springer.
19. Cullity, B.D., *Introduction to Magnetic Materials* 1972, New Jersey: Addison-Wiley Publishing Company.

20. Ohodnicki, P.R., et al., *Composition dependence of field induced anisotropy in ferromagnetic (Co,Fe)89Zr7B4 and (Co,Fe)88Zr7B4Cu1 amorphous and nanocrystalline ribbons*. Journal of Applied Physics, 2008. **104**(11): p. 113909.
21. Herzer, G., *Magnetic field-induced anisotropy in nanocrystalline Fe-Cu-Nb-Si-B alloys*. Journal of Magnetism and Magnetic Materials, 1994. **133**(1): p. 248-250.
22. Morrish, A.H., *The physical principles of magnetism*. 1965: Wiley.
23. Meiklejohn, W.H. and C.P. Bean, *New Magnetic Anisotropy*. Physical Review, 1957. **105**(3): p. 904-913.
24. Choi, H.-C., et al., *Antiferromagnetic layer thickness dependence of noncollinear uniaxial and unidirectional anisotropies in NiFe/FeMn/CoFe trilayers*. Physical Review B, 2010. **81**(22): p. 224410.
25. Dieny, B., et al., *Giant magnetoresistive in soft ferromagnetic multilayers*. Physical Review B, 1991. **43**(1): p. 1297-1300.
26. Apalkov, D., B. Dieny, and J.M. Slaughter, *Magnetoresistive Random Access Memory*. Proceedings of the IEEE, 2016. **104**(10): p. 1796-1830.
27. Wolf, S.A., et al., *Spintronics: A Spin-Based Electronics Vision for the Future*. Science, 2001. **294**(5546): p. 1488-1495.
28. Ampere, A.M., *Théorie mathématique des phénomènes électro-dynamiques: uniquement déduite de l'expérience* 1827: Reprinted by Blanchard, Paris (1958).
29. Jiles, D., *Introduction to Magnetism and Magnetic Materials*. 2 ed. 1998, Florida: Taylor and Francis Group.
30. Williams, H.J., R.M. Bozorth, and W. Shockley, *Magnetic Domain Patterns on Single Crystals of Silicon Iron*. Physical Review, 1949. **75**(1): p. 155-178.
31. Bloch, F., *Zur Theorie des Austauschproblems und der Remanenzerscheinung der Ferromagnetika*. Zeitschrift für Physik, 1932. **74**(5): p. 295-335.
32. Spinu, L., *Etude des propriétés dynamiques des assemblées de nanoparticules magnétiques*, in *Physics*. 1998, Universite de Paris-Sud: France. p. 226.
33. Bertotti, G., *Hysteresis in Magnetism: for Physicists, Materials Scientists, and Engineers*. 1998, San Diego: Academic Press.
34. Neel, L., *Théorie du traînage magnétique des ferromagnétiques en grains fins avec application aux terres cuites*. Ann. Geophys, 1949. **5**.
35. Brown, W.F., *Thermal Fluctuations of a Single-Domain Particle*. Physical Review, 1963. **130**.
36. Gurevich, A.G. and G.A. Melkov, *Magnetization Oscillations and Waves*. 1996: CRC Press. 464.
37. Kikuchi, R., *On the Minimum of Magnetization Reversal Time*. Journal of Applied Physics, 1956. **27**(11): p. 1352-1357.
38. C. Mallinson, J., *On Damped Gyromagnetic Precession*. Vol. 23. 1987. 2003-2004.
39. Aharoni, A.F., E. H.; Shtrikman, S.; Treves, D., *The Reversible Susceptibility Tensor of the Stoner-Wohlfarth Model* Bulletin of the Research Council of Israel, 1957. **6A**: p. 215-238.

40. Spinu, L., et al. *Superparamagnetism and transverse susceptibility in magnetic nanoparticle systems*. in *2000 IEEE International Magnetics Conference (INTERMAG)*. 2000.
41. Spinu, L., et al., *Probing magnetic anisotropy effects in epitaxial CrO2 thin films.* Physical Review B, 2000. **62**(13): p. 8931-8934.
42. Spinu, L., et al., *Dynamic radio-frequency transverse susceptibility in magnetic nanoparticle systems.* Journal of Applied Physics, 2000. **87**(9): p. 5490-5492.
43. Srikanth, H., et al., *Dynamic transverse susceptibility in Au–Fe–Au nanoparticles*. Vol. 304. 2001. 901-904.
44. Spinu, L., C.J.O. Connor, and H. Srikanth, *Radio frequency probe studies of magnetic nanostructures.* IEEE Transactions on Magnetics, 2001. **37**(4): p. 2188-2193.
45. Srikanth, H., et al., *Vortex dynamics and magnetic anisotropy in RuSr2GdCu2O8.* Journal of Applied Physics, 2001. **89**(11): p. 7487-7489.
46. Spinu, L., et al. *RF dynamics in nanoparticle systems with tuned strength of interactions*. in *2002 IEEE International Magnetics Conference (INTERMAG)*. 2002.
47. Spinu, L., et al., *Probing two-dimensional magnetic switching in Co/SiO2 multilayers using reversible susceptibility experiments.* Applied Physics Letters, 2005. **86**(1).
48. Spinu, L., et al., *Vectorial mapping of exchange anisotropy in IrMn/FeCo multilayers using the reversible susceptibility tensor.* Physical Review B, 2003. **68**(22): p. 4.
49. Yeninas, S.L., *Tunnel-diode resonator and nuclear magnetic resonance studies of low-dimensional magnetic and superconducting systems*. 2013, Iowa State University Physics.
50. Srikanth, H., J. Wiggins, and H. Rees, *Radio-frequency impedance measurements using a tunnel-diode oscillator technique.* Review of Scientific Instruments, 1999. **70**(7): p. 3097-3101.
51. Spinu, L., et al., *Transverse susceptibility as the low-frequency limit of ferromagnetic resonance.* Journal of Magnetism and Magnetic Materials, 2006. **296**(1): p. 1-8.
52. Weber, R.T., J. Jiang, and D.P. Barr, *EMX User's Manual*. 1998, Bruker Instruments, Inc.: Billerica, MA USA.
53. !!! INVALID CITATION !!!
54. Pozar, D.M., *Microwave Engineering*. 4 ed. 2012: John Wiley & Sons.
55. Neudecker, I., et al., *Comparison of frequency, field, and time domain ferromagnetic resonance methods.* Journal of Magnetism and Magnetic Materials, 2006. **307**(1): p. 148-156.
56. Ding, Y., T.J. Klemmer, and T.M. Crawford, *A coplanar waveguide permeameter for studying high-frequency properties of soft magnetic materials.* Journal of Applied Physics, 2004. **96**(5): p. 2969-2972.
57. Bilzer, C., et al., *Vector network analyzer ferromagnetic resonance of thin films on coplanar waveguides: Comparison of different evaluation methods.* Journal of Applied Physics, 2007. **101**(7): p. 074505.

58. Głowiński, H., et al., *Coplanar waveguide based ferromagnetic resonance in ultrathin film magnetic nanostructures: Impact of conducting layers.* Journal of Applied Physics, 2014. **116**(5): p. 053901.
59. Pareti, L.T., G., *Detection of Singularities in the Reversible Trasvers Susceptibility of an Uniaxial Ferromagnet.* Journal of Applied Physics, 1987. **61**: p. 5098-5101.
60. Adams, D.J., *Ferromagnetic Resonance Studies of Coupled Magnetic Systems*, in *Physics*. 2016, University of New Orleans.
61. Adams, D.J., et al., *Angular dependence of resonant absorption in FeCoB synthetic antiferromagnets.* AIP Advances, 2017. **7**(5): p. 056322.
62. A. Duine, R., et al., *Synthetic Antiferromagnetic Spintronics: Part of a collection of reviews on antiferromagnetic spintronics*. 2017.
63. Forrester, M., F. Kusmartsev, and E. Kovacs, *Switching dynamics of doped CoFeB trilayers and a comparison to the quasistatic approximation.* Physical Review B, 2013. **87**(17): p. 17.
64. He, H., et al., *Co/Ni (N)-Based Synthetic Antiferromagnet With Perpendicular Anisotropy and Its Application in Pseudo Spin Valves.* Ieee Transactions on Magnetics, 2010. **46**(6): p. 1327-1330.
65. Milyaev, M.A., et al., *Thermal stability of spin valves based on a synthetic antiferromagnet and Fe50Mn50 alloy.* Physics of Metals and Metallography, 2015. **116**(11): p. 1073-1079.
66. Tadisina, Z.R., et al., *Thermal stability of synthetic antiferromagnet and hard magnet coupled spin valves.* Journal of Vacuum Science & Technology A, 2008. **26**(4): p. 735-738.
67. Pietambaram, S.V., et al., *Exchange coupling control and thermal endurance of synthetic antiferromagnet structure for MRAM.* Ieee Transactions on Magnetics, 2004. **40**(4): p. 2619-2621.
68. Veloso, A. and P.P. Freitas, *Spin valve sensors with synthetic free and pinned layers.* Journal of Applied Physics, 2000. **87**(9): p. 5744-5746.
69. Byeon, S.C., A. Misra, and W.D. Doyle, *Synthetic antiferromagnetic soft underlayers for perpendicular recording media.* Ieee Transactions on Magnetics, 2004. **40**(4): p. 2386-2388.
70. Hernandez, S., M. Kapoor, and R.H. Victora, *Synthetic antiferromagnet for hard layer of exchange coupled composite media.* Applied Physics Letters, 2007. **90**(13): p. 3.
71. Khvalkovskiy, A.V., et al., *Basic principles of STT-MRAM cell operation in memory arrays.* Journal of Physics D-Applied Physics, 2013. **46**(7): p. 20.
72. Savtchenko, L., et al., *Method of writing to scalable magnetoresistance random access memory element*. 2003, Google Patents.
73. Kawato, Y., M. Futamoto, and K. Nakamoto, *Perpendicular magnetic recording medium and magnetic storage apparatus*. 2005, Google Patents.
74. Jun, H., et al., *Current-Induced Magnetization Switching in MgO Barrier Based Magnetic Tunnel Junctions with CoFeB/Ru/CoFeB Synthetic Ferrimagnetic Free Layer.* Japanese Journal of Applied Physics, 2006. **45**(10L): p. L1057.

75. Chernyshova, T., et al., *Magnetoresistive sensitivity and uniaxial anisotropy of spin-valve microstrips with a synthetic antiferromagnet*. Vol. 118. 2017. 415-420.
76. Devolder, T., et al., *Annealing stability of magnetic tunnel junctions based on dual MgO free layers and [Co/Ni] based thin synthetic antiferromagnet fixed system.* Journal of Applied Physics, 2017. **121**(11): p. 113904.
77. Lapa, P.N., et al., *Spin valve with non-collinear magnetization configuration imprinted by a static magnetic field.* AIP Advances, 2016. **6**(5): p. 056107.
78. Van Roosbroeck, R., et al., *Synthetic Antiferromagnetic Nanoparticles as Potential Contrast Agents in MRI.* ACS Nano, 2014. **8**(3): p. 2269-2278.
79. Bi, C., et al., *Anomalous spin-orbit torque switching in synthetic antiferromagnets.* Physical Review B, 2017. **95**(10): p. 104434.
80. Grünberg, P., et al., *Layered Magnetic Structures: Evidence for Antiferromagnetic Coupling of Fe Layers across Cr Interlayers.* Physical Review Letters, 1986. **57**(19): p. 2442-2445.
81. Abarra, E.N., et al., *Longitudinal magnetic recording media with thermal stabilization layers.* Applied Physics Letters, 2000. **77**(16): p. 2581-2583.
82. Fullerton, E.E., et al., *Antiferromagnetically coupled magnetic media layers for thermally stable high-density recording.* Applied Physics Letters, 2000. **77**(23): p. 3806-3808.
83. Inomata, A., et al., *Exchange coupling strength in synthetic ferrimagnetic media.* Magnetics, IEEE Transactions on, 2001. **37**(4): p. 1449-1451.
84. Maffitt, T.M., et al., *Design considerations for MRAM.* IBM J. Res. Dev., 2006. **50**(1): p. 25-39.
85. Sun, J.Z., et al., *Thermal activation-induced sweep-rate dependence of magnetic switching astroid.* Applied Physics Letters, 2001. **78**(25): p. 4004-4006.
86. Bruno, P., *Interlayer exchange coupling: a unified physical picture.* Journal of Magnetism and Magnetic Materials, 1993. **121**: p. 248-252.
87. Adams, D.J., et al., *Critical switching curves of FeCoB synthetic antiferromagnets.* Journal of Physics D: Applied Physics, 2018. **51**(5): p. 055005.
88. Cimpoesu, D., L. Stoleriu, and A. Stancu, *Generalized Stoner-Wohlfarth model accurately describing the switching processes in pseudo-single ferromagnetic particles.* Journal of Applied Physics, 2013. **114**(22): p. 223901.
89. Cimpoesu, D., et al., *Angular resonant absorption curves in magnetic nanowire arrays.* Applied Physics Letters, 2013. **102**(23).
90. Spinu, L., et al., *Micromagnetic calculation of the transverse susceptibility of patterned media.* IEEE Transactions on Magnetics, 2003. **39**(5): p. 2516-2518.
91. Cimpoesu, D., et al., *Micromagnetic Simulation of the imaginary part of the transverse susceptibility.* IEEE Transactions on Magnetics, 2005. **41**(10): p. 3121-3123.

92. Cimpoesu, D., A. Stancu, and L. Spinu, *Physics of complex transverse susceptibility of magnetic particulate systems.* Physical Review B, 2007. **76**(5): p. 054409.
93. Stoecklein, W., S.S.P. Parkin, and J.C. Scott, *Ferromagnetic resonance studies of exchange-biased Permalloy thin films.* Physical Review B, 1988. **38**(10): p. 6847-6854.
94. Ambrose, T., R.L. Sommer, and C.L. Chien, *Angular dependence of exchange coupling in ferromagnet/antiferromagnet bilayers.* Physical Review B, 1997. **56**(1): p. 83-86.
95. O'Handley, R.C., *Modern Magnetic Materials: Principles and Applications*. 2000: John Wiley & Sons, Inc.
96. Hempstead, R., S. Krongelb, and D.A. Thompson, *Unidirectional anisotropy in nickel-iron films by exchange coupling with antiferromagnetic films*. Vol. 14. 1978. 521-523.
97. Tsang, C., N. Heiman, and K. Lee, *Exchange induced unidirectional anisotropy at FeMn-Ni80Fe20 interfaces.* Journal of Applied Physics, 1981. **52**(3): p. 2471-2473.
98. Tsang, C. and K. Lee, *Temperature dependence of unidirectional anisotropy effects in the Permalloy-FeMn systems.* Journal of Applied Physics, 1982. **53**(3): p. 2605-2607.
99. Scott, J.C., *Ferromagnetic resonance studies in the bilayer system Ni0.80Fe0.20/Mn0.50Fe0.50: Exchange anisotropy.* Journal of Applied Physics, 1985. **57**(8): p. 3681-3683.
100. Ambrose, T. and C.L. Chien, *Magnetic properties of exchange coupled NiFe/CoO/NiFe trilayers.* Applied Physics Letters, 1994. **65**(15): p. 1967-1969.
101. Allegranza, O. and M.M. Chen, *Effect of substrate and antiferromagnetic film’s thickness on exchange-bias field (invited).* Journal of Applied Physics, 1993. **73**(10): p. 6218-6222.
102. Xi, H. and R.M. White, *Critical thickness effect in the exchange-coupled NiFe/CrMnPtx bilayer system.* Physical Review B, 2000. **61**(2): p. 1318-1323.
103. Ali, M., et al., *Antiferromagnetic layer thickness dependence of the IrMn/Co exchange-bias system.* Physical Review B, 2003. **68**(21): p. 214420.
104. Xi, H. and R.M. White, *Antiferromagnetic thickness dependence of exchange biasing.* Physical Review B, 2000. **61**(1): p. 80-83.
105. Mauri, D., et al., *Simple model for thin ferromagnetic films exchange coupled to an antiferromagnetic substrate.* Journal of Applied Physics, 1987. **62**(7): p. 3047-3049.
106. Malozemoff, A.P., *Mechanisms of exchange anisotropy (invited).* Journal of Applied Physics, 1988. **63**(8): p. 3874-3879.
107. Malozemoff, A.P., *Heisenberg-to-Ising crossover in a random-field model with uniaxial anisotropy.* Physical Review B, 1988. **37**(13): p. 7673-7679.
108. Jungblut, R., et al., *Orientational dependence of the exchange biasing in molecular-beam-epitaxy-grown Ni80Fe20/Fe50Mn50 bilayers (invited).* Journal of Applied Physics, 1994. **75**(10): p. 6659-6664.

109. Dieny, B., et al., *Recent results on the giant magnetoresistance in magnetic multilayers (anisotropy, thermal variation and CCP-GMR).* Journal of Magnetism and Magnetic Materials, 1995. **151**(3): p. 378-387.
110. Nikolaev, K.R., et al., *Exchange-biased La2/3Ca1/3(Sr1/3)MnO3 ultrathin films.* Applied Physics Letters, 2000. **76**(4): p. 478-480.
111. Rohrman, F.A., *The Theory of the Properties of Metals and Alloys (Mott, N. F.; Jones, H.).* Journal of Chemical Education, 1937. **14**(2): p. 99.
112. Fert, A., *Nobel Lecture: Origin, development, and future of spintronics.* Reviews of Modern Physics, 2008. **80**(4): p. 1517-1530.
113. Binasch, G., et al., *Enhanced magnetoresistance in layered magnetic structures with antiferromagnetic interlayer exchange.* Physical Review B, 1989. **39**(7): p. 4828-4830.
114. Baibich, M.N., et al., *Giant Magnetoresistance of (001)Fe/(001)Cr Magnetic Superlattices.* Physical Review Letters, 1988. **61**(21): p. 2472-2475.
115. Fert, A.B., P., in *Ultrathin Magnetic Structures, Vol. II*, B.B. Heinrich, J.A.C., Editor. 1994, Springer: Berlin. p. 82.
116. Parkin, S.S.P., in *Ultrathin Magnetic Structures, Vol. II*, B.B. Heinrich, J.A.C., Editor. 1994, Springer: Berlin. p. 148.
117. Parkin, S.S.P., in *Annu. Rev. Mater. Sci.*, B.W. Wessels, Editor. 1995. p. 357.
118. Parkin, S., et al., *Magnetically engineered spintronic sensors and memory.* Proceedings of the IEEE, 2003. **91**(5): p. 661-680.
119. Parkin, S., *Spin-Polarized Current in Spin Valves and Magnetic Tunnel Junctions.* MRS Bulletin, 2011. **31**(5): p. 389-394.
120. Xi, H. and R.M. White, *Coupling between two ferromagnetic layers separated by an antiferromagnetic layer.* Physical Review B, 2000. **62**(6): p. 3933-3940.
121. Layadi, A., *Investigation of off-aligned exchange coupling by torque curve and ferromagnetic resonance.* Journal of Applied Physics, 2001. **90**(9): p. 4651-4656.
122. Jiménez, E., et al., *Emergence of noncollinear anisotropies from interfacial magnetic frustration in exchange-bias systems.* Physical Review B, 2009. **80**(1): p. 014415.
123. Jiménez, E., et al., *Role of anisotropy configuration in exchange-biased systems.* Journal of Applied Physics, 2011. **109**(7): p. 07D730.
124. McMichael, R.D., et al., *Ferromagnetic resonance studies of NiO-coupled thin films of Ni80Fe20.* Physical Review B, 1998. **58**(13): p. 8605-8612.
125. Geshev, J., L.G. Pereira, and J.E. Schmidt, *Angular dependence of the exchange bias obtained from magnetization and ferromagnetic resonance measurements in exchange-coupled bilayers.* Physical Review B, 2001. **64**(18): p. 184411.
126. Smit, J.B., H, *Ferromagnetic Resonance Absorption in BaFe12O19, a Highly Anisotropic Crystal.* Philips Res. Rep., 1955. **10**: p. 113-130.
127. Bennett, A.J. and B.R. Cooper, *Origin of the Magnetic "Surface Anisotropy" of Thin Ferromagnetic Films.* Physical Review B, 1971. **3**(5): p. 1642-1649.

128. Rubinstein, M., P. Lubitz, and C. Shu-Fan, *Ferromagnetic-resonance field shift in an exchange-biased CoO/Ni80Fe20 bilayer.* Journal of Magnetism and Magnetic Materials, 1999. **195**(2): p. 299-306.
129. Graët, C.L., et al., *Probing misalignment in exchange biased systems: A dynamic approach.* Applied Physics Letters, 2009. **94**(26): p. 262502.
130. Teale, R.W. and K. Tweedale, *Ytterbium-ion relaxation in ferrimagnetic resonance.* Physics Letters, 1962. **1**(7): p. 298-300.
131. Clarke, B.H., K. Tweedale, and R.W. Teale, *Rare-Earth Ion Relaxation Time and G Tensor in Rare-Earth-Doped Yttrium Iron Garnet. I. Ytterbium.* Physical Review, 1965. **139**(6A): p. A1933-A1943.
132. Clarke, B.H., et al., *Rare-Earth Ion Relaxation in Ferrimagnetic Resonance.* Journal of Applied Physics, 1963. **34**(4): p. 1269-1270.
133. LeCraw, R.C., et al., *Ferromagnetic Relaxation in Europium Iron Garnet.* Physical Review Letters, 1963. **11**(11): p. 490-493.
134. Spencer, E.G., J.P. Remeika, and P.V. Lenzo, *FERROMAGNETIC RESONANCE LOSSES IN INDIUM-SUBSTITUTED YTTRIUM IRON GARNET.* Applied Physics Letters, 1964. **4**(10): p. 171-172.
135. Dillon, J.F. and J.W. Nielsen, *Effects of Rare Earth Impurities on Ferrimagnetic Resonance in Yttrium Iron Garnet.* Physical Review Letters, 1959. **3**(1): p. 30-31.
136. Van Vleck, J.H. and R. Orbach, *Ferrimagnetic Resonance of Dilute Rare-Earth Doped Iron Garnets.* Physical Review Letters, 1963. **11**(2): p. 65-67.
137. Clogston, A.M., *Relaxation Phenomena in Ferrites.* Bell Sys. Tech. Journal 1955. **34**.
138. Galt, J.K., W.A. Yager, and F.R. Merritt, *Temperature Dependence of Ferromagnetic Resonance Line Width in a Nickel Iron Ferrite: A New Loss Mechanism.* Physical Review, 1954. **93**(5): p. 1119-1120.
139. Orbach, R., *Spin-lattice relaxation in rare-earth salts.* Proceedings of the Royal Society of London. Series A. Mathematical and Physical Sciences, 1961. **264**(1319): p. 458-484.
140. Orbach, R., *Spin-Lattice Relaxation Time of Rare-Earth Ions in Strong Exchange Fields.* Journal of Applied Physics, 1962. **33**(6): p. 2144-2144.
141. Lubitz, P., et al., *Temperature dependence of ferromagnetic resonance as induced by NiO pinning layers.* Journal of Applied Physics, 1998. **83**(11): p. 6819-6821.
142. McMichael, R.D., et al., *Exchange bias relaxation in CoO-biased films.* Journal of Applied Physics, 2000. **87**(9): p. 6406-6408.
143. Lubitz, P., et al., *Frequency and temperature dependence of ferromagnetic linewidth in exchange biased Permalloy.* Journal of Applied Physics, 2001. **89**(11): p. 6901-6903.
144. Dubowik, J., et al., *Temperature dependence of ferromagnetic resonance in permalloy/NiO exchange-biased films.* Eur. Phys. J. B, 2005. **45**(2): p. 283-288.
145. Gloanec, M., et al., *Dynamical effect in measurement of the exchange-bias field: A consequence of the slow-relaxer mechanism.* Physical Review B, 2009. **80**(22): p. 220404.

146. Gloanec, M., et al., *Temperature dependence of exchange bias in NiFe/FeMn bilayers.* Physical Review B, 2010. **82**(14): p. 144433.
147. Khanal, S., et al., *Exchange bias in (FeNi/IrMn)n multilayer films evaluated by static and dynamic techniques.* Journal of Physics D-Applied Physics, 2014. **47**(25): p. 8.
148. Gredig, T., I.N. Krivorotov, and E.D. Dahlberg, *Temperature dependence of magnetization reversal and angular torque in Co/CoO.* Physical Review B, 2006. **74**(9): p. 094431.
149. Stiles, M.D. and R.D. McMichael, *Model for exchange bias in polycrystalline ferromagnet-antiferromagnet bilayers.* Physical Review B, 1999. **59**(5): p. 3722-3733.
150. Adams, D.J., et al., *Temperature dependence of exchange bias in (NiFe/IrMn)n multilayer films studied through static and dynamic techniques.* AIP Advances, 2018. **8**(5): p. 056302.

List of Publications

1. J. Hu, J.Y. Liu, D. Graf, S.M.A Radmanesh, **Daniel J. Adams**, A. Chuang, Y. Wang, I. Chiorescu, J. Wei, L. Spinu, Z.Q. Mao, "π Berry phase and Zeeman splitting of Weyl semimetal TaP" *Scientific Reports*, 6, 18674 (2016).

2. Olasehinde Owoseni, Emmanuel Nyankson, Yueheng Zhang, **Daniel J. Adams,** Jibao He, Leonard Spinu, Gary L McPherson, Arijit Bose, Ram B Gupta, Vijay T. John, "Interfacial Adsorption and Surfactant Release Characteristics of Magnetically Functionalized Halloysite Nanotubes for Responsive Emulsions", *Journal of Colloid and Interface Science*, 463, 288-298 (2016).

3. Jinyu Liu, Jin Hu, Huibo Cao, Yanglin Zhu, Alyssa Chuang, D. Graf, **Daniel J. Adams**, S. M. A. Radmanesh, L. Spinu, I. Chiorescu, Zhiqiang Mao, "Nearly massless Dirac fermions hosted by Sb square net in $BaMnSb_2$", *Scientific Reports*, 6, 30525 (2016).

4. **Daniel J. Adams**, M. A. Khan, P. Poudyal, L. Spinu, "Angular dependence of resonant absorption in FeCoB synthetic antiferromagnets", *AIP Advances*, **7**(5): p. 056322 (2017).

5. J. Y. Liu, J. Hu, Q. Zhang, D. Graf, H. B. Cao, S. M. A. Radmanesh, **Daniel J. Adams**, Y. L. Zhu, G. F. Cheng, X. Liu, W. A. Phelan, J. Wei, M. Jaime, F. Balakirev, D. A. Tennant, J. F. DiTusa, I. Chiorescu, L. Spinu, Z. Q. Mao, "A magnetic topological semimetal $Sr_{1-y}Mn_{1-z}Sb_2$ (y, z < 0.1)", *Nature Materials*, 16(9), 905–910 (2017).

6. **Daniel J. Adams**, S. Khanal, M. A. Khan, A. Maksymov, L. Spinu, "Temperature dependence of exchange bias in $(NiFe/IrMn)_n$ multilayer films studied through static and dynamic techniques", *AIP Advances*, 8(5) (2018).

7. **Daniel J. Adams**, Dorin Cimpoesu, Mohammad Asif Khan, Pratik Poudyal, Leonard Spinu, "Critical switching curves of FeCoB synthetic antiferromagnets", *Journal of Physics D: Applied Physics*, 51(5) (2018).

Vita

Daniel Joseph Adams was born in Metairie, Louisiana in 1990. He received his Bachelor of Science in Physics in 2014 and Master of Science in Applied Physics in 2016 from the University of New Orleans. His graduate work was done under the direction of Professor Leonard Spinu.